Cell

Lymph nodes are innervated by a unique population of sensory neurons with immunomodulatory potential

Graphical abstract

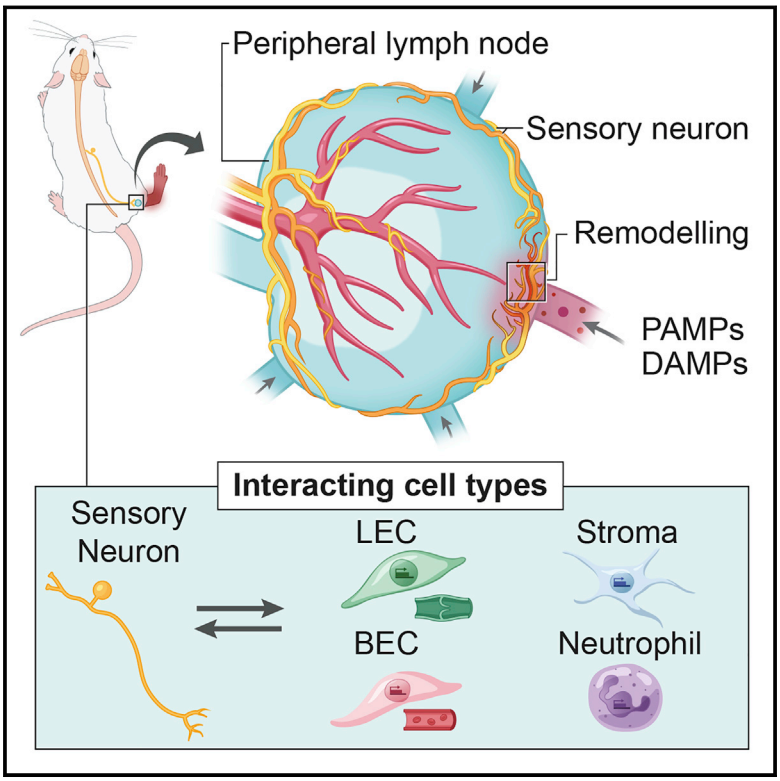

Highlights

- Anatomical and molecular identification of lymph node-innervating nociceptors
- Demonstration of inflammation-induced plasticity of sensory innervation of lymph nodes
- Transcriptome-based identification of nociceptor target cells in lymph node
- Optogenetic validation of lymph node target cell modulation by nociceptor activity

Authors

Siyi Huang, Carly G.K. Ziegler, John Austin, ..., Jose Ordovas-Montanes, Alex K. Shalek, Ulrich H. von Andrian

Correspondence

siyi_huang@hms.harvard.edu (S.H.), shalek@mit.edu (A.K.S.), uva@hms.harvard.edu (U.H.v.A.)

In Brief

Peripheral lymph nodes are monitored by a unique assortment of sensory neurons with strong enrichment for peptidergic nociceptors. By combining whole-mount immunolabeling, retrograde neuronal tracing, single-cell genomics, and optogenetic approaches, Huang et al. uncover a bidirectional neuroimmune communication axis in lymph nodes, where sensory neurons not only sense lymph node immune status but also, when activated, modulate gene expression in immune and stromal cells.

Huang et al., 2021, Cell *184*, 1–19
January 21, 2021
https://doi.org/10.1016/j.cell.2020.11.028

CellPress

Cell

CellPress

Article

Lymph nodes are innervated by a unique population of sensory neurons with immunomodulatory potential

Siyi Huang,[1,2,8,*] Carly G.K. Ziegler,[1,3,4,5,6,8] John Austin,[1,2] Najat Mannoun,[1,2] Marko Vukovic,[1,3,4] Jose Ordovas-Montanes,[1,3,4,7] Alex K. Shalek,[1,2,3,4,5,9,*] and Ulrich H. von Andrian[1,2,9,10,*]

[1]The Ragon Institute of MGH, MIT and Harvard, Cambridge, MA 02139, USA
[2]Department of Immunology & HMS Center for Immune Imaging, Harvard Medical School, Boston, MA 02115, USA
[3]Institute for Medical Engineering & Science (IMES), Department of Chemistry, and Koch Institute for Integrative Cancer Research, MIT, Cambridge, MA 02139, USA
[4]Broad Institute of MIT and Harvard, Cambridge, MA 02142, USA
[5]Harvard-MIT Program in Health Sciences and Technology, Harvard Medical School, Cambridge, MA 02139, USA
[6]Harvard Graduate Program in Biophysics, Harvard University, Boston, MA 02115, USA
[7]Division of Gastroenterology, Boston Children's Hospital, Boston, MA 02115, USA
[8]These authors contributed equally
[9]Senior author
[10]Lead Contact
*Correspondence: siyi_huang@hms.harvard.edu (S.H.), shalek@mit.edu (A.K.S.), uva@hms.harvard.edu (U.H.v.A.)
https://doi.org/10.1016/j.cell.2020.11.028

SUMMARY

Barrier tissue immune responses are regulated in part by nociceptors. Nociceptor ablation alters local immune responses at peripheral sites and within draining lymph nodes (LNs). The mechanisms and significance of nociceptor-dependent modulation of LN function are unknown. Using high-resolution imaging, viral tracing, single-cell transcriptomics, and optogenetics, we identified and functionally tested a sensory neuro-immune circuit that is responsive to lymph-borne inflammatory signals. Transcriptomics profiling revealed that multiple sensory neuron subsets, predominantly peptidergic nociceptors, innervate LNs, distinct from those innervating surrounding skin. To uncover LN-resident cells that may interact with LN-innervating sensory neurons, we generated a LN single-cell transcriptomics atlas and nominated nociceptor target populations and interaction modalities. Optogenetic stimulation of LN-innervating sensory fibers triggered rapid transcriptional changes in the predicted interacting cell types, particularly endothelium, stromal cells, and innate leukocytes. Thus, a unique population of sensory neurons monitors peripheral LNs and may locally regulate gene expression.

INTRODUCTION

The nervous and immune systems have been viewed traditionally as functionally and anatomically distinct even though they share a critical common task: to detect and respond to internal and external threats that may be physical, chemical, or biological in nature. The nervous system has a direct role in avoidance of potentially injurious or infectious situations, whereas the immune system provides key resistance and repair mechanisms. Neuro-immune interactions have been investigated in a number of settings, especially in the central nervous system (CNS) (Klein et al., 2017; Norris and Kipnis, 2019; Prinz and Priller, 2017), and several recent studies have uncovered evidence of bidirectional communication between the peripheral nervous system (PNS) and the immune system in the spleen, bone marrow, intestine, airways, lungs, and skin (Baral et al., 2019; Chiu et al., 2012; Foster et al., 2017; Godinho-Silva et al., 2019; McMahon et al., 2015; Ordovas-Montanes et al., 2015; Veiga-Fernandes and Mucida, 2016). However, the mechanisms and consequences of these multi-faceted interactions are still poorly understood.

Best recognized for their sensory role, dorsal root ganglion (DRG) neurons provide the CNS with information from the periphery through direct innervation of peripheral tissues. Traditional structural and functional characterization of sensory neurons and, more recently, single-cell RNA sequencing (scRNA-seq)-based molecular profiling have revealed a high degree of heterogeneity among somatosensory neurons (Sharma et al., 2020; Kupari et al., 2019; Usoskin et al., 2015; Wood et al., 2018; Cohen et al., 2019). In particular, one major subset of sensory neurons, nociceptors, has been increasingly appreciated for its diversity and potential for sensing and modulating immune and inflammatory processes (Sharma et al., 2020; Baral et al., 2019; Kupari et al., 2019; McMahon et al., 2015; Ordovas-Montanes et al., 2015; Usoskin et al., 2015; Wood et al., 2018; Cohen et al., 2019). In many cases, nociceptor modulation of immunity involves bioactive neuropeptides, such as calcitonin

Please cite this article in press as: Huang et al., Lymph nodes are innervated by a unique population of sensory neurons with immunomodulatory potential, Cell (2021), https://doi.org/10.1016/j.cell.2020.11.028

gene-related peptide (CGRP) and substance P, which are released from activated peripheral terminals of nociceptors and act on various immune and stromal cells that express the corresponding receptors (Assas et al., 2014; Baral et al., 2019; Suvas, 2017).

Peptidergic neurons of putative sensory origin innervate most, if not all, secondary lymphoid organs and barrier tissues, but their density, pattern of innervation, and neighboring cell types are notably different between tissues (Belvisi, 2002; Brierley et al., 2004; Felten et al., 1985; Fink and Weihe, 1988; Kurkowski et al., 1990; Oaklander and Siegel, 2005; Popper et al., 1988). This raises the intriguing possibility that sensory neurons targeting distinct peripheral sites may contribute differently to immune responses by engaging in local tissue-specific sensory neuroimmune circuits. Indeed, recent work has uncovered a key role of nociceptors in shaping immune activity in major barrier tissues, as evidenced by animal models of asthma, colitis, psoriasis, and infectious disease (Baral et al., 2019; Foster et al., 2017; McMahon et al., 2015; Ordovas-Montanes et al., 2015).

To date, the immunomodulatory effect of nociceptors has been documented primarily in the context of innate immune responses, where pro- and anti-inflammatory activities are observed. For instance, nociceptors in the skin can sense invading bacteria and attenuate inflammatory responses against bacterial infections (Chiu et al., 2013). Conversely, upon topical exposure to imiquimod, a TLR7 agonist, dermal dendritic cells (DCs) require signals from cutaneous nociceptors to produce interleukin (IL)-23, a pro-inflammatory cytokine that drives psoriasiform dermatitis (Riol-Blanco et al., 2014). Interestingly, both studies report that nociceptors also affect regional lymph nodes (LNs); systemic nociceptor ablation prior to a bacterial infection caused a profound increase in lymphoid and myeloid LN cellularity (Chiu et al., 2013), whereas, upon imiquimod exposure, the absence of nociceptors reduced LN cellularity (Riol-Blanco et al., 2014). In both settings, nociceptors were globally ablated, so it is unclear whether the observed effects were due to loss of sensory innervation in the LNs themselves or in the surrounding non-lymphoid tissues.

LNs act as sentinel organs that collect, filter, and monitor the constant flow of interstitial fluid (lymph) that is drained from peripheral tissues by afferent lymph vessels. LNs are the principal initiation sites for adaptive immune responses and are required for maintenance of peripheral tolerance to self-antigens (Buettner and Bode, 2012; Karrer et al., 1997; Lakkis et al., 2000; Mooster et al., 2015; Zhou et al., 2003). Generation of local adaptive immune responses against immunogens critically depends on bidirectional information flow between the peripheral site of initial immune challenge and the draining LNs, where antigen acquisition/presentation and subsequent lymphocyte differentiation and maturation are orchestrated. This process relies on directed transport of antigen-presenting cells, cytokines, and antigens via afferent lymph vessels from the periphery and selective recruitment of vast numbers of naive and memory lymphocytes from the blood via high endothelial venules (HEVs). Within LNs, specialized endothelial and stromal cells delineate the lymph conduits and organize the extravascular space into discrete anatomic domains. In addition, a variety of myeloid leukocytes cooperate to support efficient antigen encounters by B and T cells to elicit an appropriate immunogenic or tolerogenic response.

Previous studies of LNs in several mammalian species have shown that LNs are innervated by noradrenergic and peptidergic neurons (Felten et al., 1985; Fink and Weihe, 1988). In animal models of arthritis and contact hypersensitivity, local application of capsaicin, a neurotoxin that targets TRPV1 (transient receptor potential channel-vanilloid subfamily member 1), attenuates inflammatory responses, suggesting a pro-inflammatory role for capsaicin-sensitive sensory innervation of LNs (Felten et al., 1992; Lorton et al., 2000; Shepherd et al., 2005a). More recently, a diphtheria toxin fragment A (DTA)-based mouse model in which mice are globally deficient in nociceptors revealed a role of sensory neurons in regulating antigen retention and flow through peripheral LNs in immunized mice (Hanes et al., 2016). This observation, together with studies in sheep that showed a stimulatory effect of a neuropeptide, substance P, on lymph flow and lymphocyte recirculation through peripheral LNs (Moore et al., 1989), suggests that modulation of lymphatic trafficking may be one of the mechanisms by which putative sensory innervation could locally regulate immune responses in LNs. Nonetheless, sensory neuron-immune interactions in LNs have yet to be established definitively and studied systematically.

Here, by integrating state-of-the-art imaging, retrograde labeling, scRNA-seq, and optogenetics, we mapped sensory neuronal, immune and stromal components of skin-draining LNs. We found that sensory neurons innervate LNs with a preferential distribution toward the LN periphery, the region most prone to undergo rapid inflammation-induced mechanical, chemical, and cellular changes. Using scRNA-seq of retrogradely labeled DRG neurons, we identified four molecularly distinct LN-innervating sensory neuronal subtypes with strong enrichment for peptidergic nociceptors. Moreover, we found that LN-innervating neurons expressed a specific set of inflammatory molecules and receptors and could undergo structural remodeling following cutaneous challenge with direct (TLR4) and indirect (TLR1/2) agonists. This suggests that peripheral inflammatory signals are conveyed to LN-innervating neurons via additional secondary mediators, potentially through communication with other LN-resident cell types. To nominate the putative cellular communication partners of these sensory neurons, we used Seq-Well-based scRNA-seq to generate a single-cell "atlas" of murine steady-state LNs. By *in-silico*-matching known ligands and receptors expressed by LN-innervating sensory neurons and each LN-resident stromal and immune subset, we determined that stromal cells exhibit the highest potential for interaction with local sensory fibers. Finally, using optogenetic triggering, we first stimulated LN-innervating sensory neurons and then profiled LN-resident cell types using single-cell transcriptomics to identify the LN-resident cells most responsive to neuronal activity, including lymphatic endothelial cells, non-HEV blood endothelial cells, non-endothelial stroma, and certain populations of innate leukocytes, confirming our predictions. Our results define the anatomical and molecular identity of a previously enigmatic population of sensory neurons that innervate LNs and uncover a sensory neuron-stroma axis in steady-state LNs. The experimental and computational frameworks and

Please cite this article in press as: Huang et al., Lymph nodes are innervated by a unique population of sensory neurons with immunomodulatory potential, Cell (2021), https://doi.org/10.1016/j.cell.2020.11.028

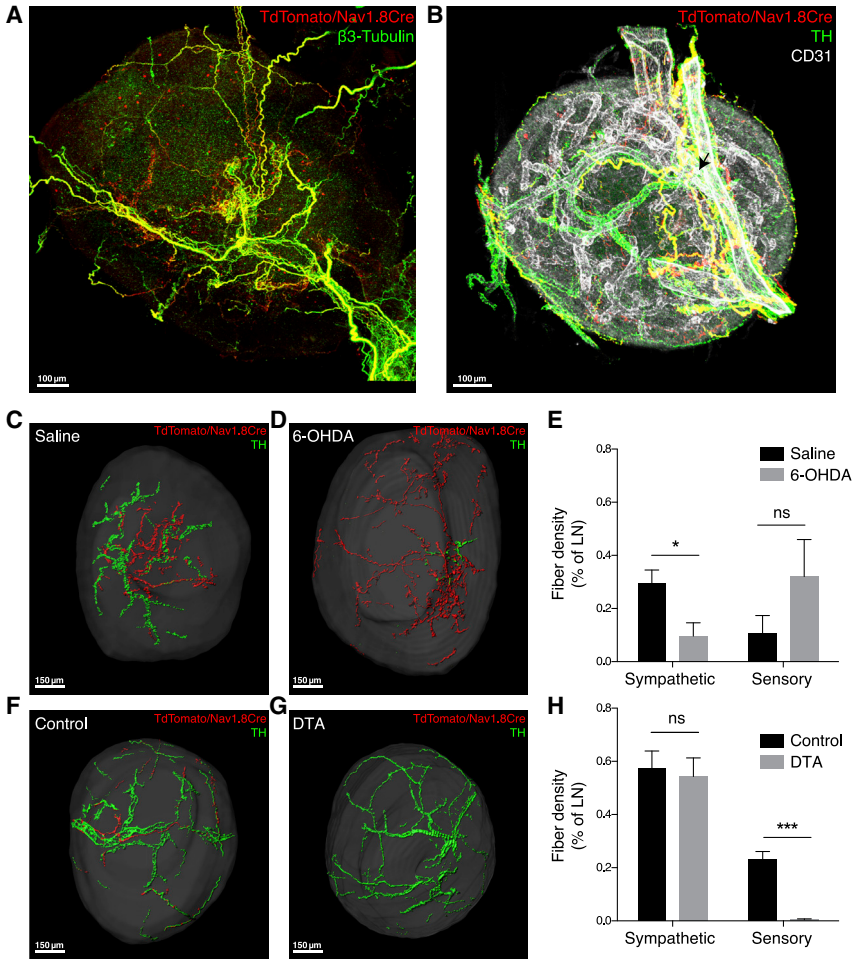

Figure 1. Dual innervation of peripheral LNs by sensory and sympathetic neurons

(A and B) Representative 3D reconstructions of popLNs from *Nav1.8*$^{Cre/+}$ × *Rosa26*$^{LSL\text{-}tdTomato/+}$ animals stained for sensory neurons and (A) the pan-neuronal marker β3-tubulin or (B) tyrosine hydroxylase (TH) and CD31 to mark sympathetic fibers and vasculature, respectively. Black arrow: LN hilum. Scale bars, 100 μm.

(C and D) Representative rendered surfaces for tdTomato$^+$ sensory fibers (red) and TH$^+$ sympathetic fibers (green) in popLNs (gray) of saline-treated (C) and 6-OHDA-treated (D) *Nav1.8*$^{Cre/+}$ × *Rosa26*$^{LSL\text{-}tdTomato/+}$ mice. Scale bars, 150 μm.

(E) Quantification of the effect of 6-OHDA treatment on sensory and sympathetic fiber density. n = 5 LN/group, 3 control, 3 OHDA treated. Sympathetic fibers, *p = 0.0232; sensory fibers, ns, p = 0.2050 by unpaired t test.

(F and G) Representative rendered surfaces for tdTomato$^+$ sensory fibers (red) and TH$^+$ sympathetic fibers (green) in rendered popLNs (gray) of age-matched *Nav1.8*$^{Cre/+}$ × *Rosa26*$^{LSL\text{-}tdTomato/+}$ (F) and Nav1.8-DTA (G) mice. Scale bars, 150 μm.

(H) Quantification of the effect of DTA-induced developmental ablation of Nav1.8$^+$ neurons on sensory and sympathetic fiber density. n = 6 LN/group, 3 mutant, 3 littermate controls. Sympathetic fibers, not significant (ns), p = 0.7542; sensory fibers, ***p < 0.001 by unpaired t test.

See also Figure S1 and Video S1.

foundational datasets established in this study should be broadly applicable to future analysis of neural circuits in a wide variety of tissues.

RESULTS

LNs are innervated by sensory and sympathetic neurons

To establish whether, where, and to what extent LNs are innervated by sensory neurons, we pursued several complementary strategies. First, we labeled peripheral neurons of sensory lineage, including nociceptors, with tdTomato using "knockin" mice that expressed Cre recombinase under control of the *Nav1.8* locus, which encodes a nociceptor-enriched voltage-gated sodium channel (Nassar et al., 2004). To visualize the complete 3D morphology of nerve fibers within intact popliteal LNs (popLNs) from these animals, we used a protocol adapted from a previously described tissue imaging method, immunolabeling-enabled 3D imaging of solvent-cleared organs (iDISCO; STAR Methods; Renier et al., 2014). By co-staining for tdTomato and the pan-neuronal marker β3-tubulin, tdTomato$^+$ nerve fibers, presumably originating from sensory neurons, were readily detectable as a major component of the neuronal architecture within and in the immediate vicinity of popLNs, particularly at the hilus (Figure 1A; Video S1). Consistent with previous studies that describe sympathetic innervation of LNs (Bellinger et al., 1992; Felten et al., 1985), popLNs also contained a sizeable population of tdTomato$^-$ neuronal fibers that expressed tyrosine hydroxylase (TH), a prototypical marker for sympathetic neurons (Figure 1B; Video S1). In comparison, cholinergic parasympathetic fibers genetically labeled with GFP in *ChAT*^{BAC}*-EGFP* animals, where EGFP expression was driven by endogenous choline acetyltransferase (ChAT) transcriptional regulatory elements within a transgene, were never observed in LNs, even though scattered GFP$^+$ cells were detectable in LNs, likely representing previously described ChAT$^+$ immune cells (Reardon et al., 2013; Rosas-Ballina et al., 2011; Tallini et al., 2006; Figure S1A). As noted previously (Bellinger et al., 1992), the primary path of nerve entry into LNs closely tracked the major blood vessels that entered the LN in the hilus region (Figure 1B; Video S1). Incoming nerve fibers preferentially traveled along a subset of blood vessels that were identified as small arteries and arterioles based on selective genetic labeling in *Bmx-CreER*^{T2} × *Rosa26*$^{eYFP/+}$mice in which arterial endothelial cells (ECs) express YFP (Ehling et al., 2013; Figure S1B). In the LNs, the arborization pattern of tdTomato$^-$ TH$^+$ (putative sympathetic) neurons was notably distinct from that of tdTomato$^+$ TH$^-$ (putative sensory) neurons. Although TH$^+$ neurons primarily innervated the vasculature and often wrapped tightly around blood vessels, tdTomato$^+$ fibers displayed a different terminal morphology and not only aligned

Please cite this article in press as: Huang et al., Lymph nodes are innervated by a unique population of sensory neurons with immunomodulatory potential, Cell (2021), https://doi.org/10.1016/j.cell.2020.11.028

with vasculature but also branched extensively into the interstitial space (Figure 1B; Video S1).

Sensory (NaV1.8$^+$) and sympathetic (TH$^+$) neurons are traditionally defined based on the location of their cell bodies, with the former residing in vagal ganglia or DRGs and the latter in sympathetic ganglia (SG), which each represent anatomically segregated structures that can be identified reliably. However, some Nav1.8-lineage neurons are also found in sympathetic ganglia (Gautron et al., 2011), and TH$^+$ low-threshold mechanoreceptors are present in DRGs (Li et al., 2011), so neither marker is truly specific. To unequivocally establish the anatomic origin of intranodal fibers, we retrogradely labeled LN-innervating neurons in DRGs and sympathetic ganglia by injecting a fluorescent neuronal tracer, wheat germ agglutinin (WGA)-AF488, into inguinal LNs (iLNs) of *Nav1.8*$^{Cre/+}$ × *Rosa26*$^{tdTomato/+}$ mice (Robertson, 1990; Figure S1C; STAR Methods). Expression of tdTomato and TH within WGA$^+$ populations revealed that more than 90% of WGA$^+$ neurons in DRGs and sympathetic ganglia were tdTomato$^+$TH$^-$ and tdTomato$^-$TH$^+$, respectively, confirming that Nav1.8 and TH adequately and specifically identify sensory and sympathetic innervation of LNs (Figures S1D–S1H).

Having confirmed that LNs are innervated by sensory and sympathetic neurons, we next asked whether either type of innervation depended on the presence of the other. We assessed the differential sensitivity of LN-innervating neurons to 6-hydroxydopamine (6-OHDA)-mediated chemical sympathectomy or diphtheria toxin A (DTA)-mediated genetic ablation of Nav1.8-lineage neurons. 6-OHDA treatment efficiently depleted LNs of sympathetic fibers but had no significant effect on Nav1.8$^+$ sensory fibers (Figures 1C–1E). Conversely, ablation of Nav1.8-lineage neurons in *Nav1.8*$^{Cre/+}$ × *Rosa26*$^{DTA/tdTomato}$ (Nav1.8-DTA) mice (Abrahamsen et al., 2008) resulted in profound loss of sensory fibers without affecting TH$^+$ fibers (Figures 1F–1H). Thus, LNs receive mutually independent sympathetic and sensory innervation.

Sensory neurons preferentially innervate the periphery of LNs

Next we mapped the spatial distribution of sensory fibers in LNs. LNs are anatomically divided into the lymphocyte-rich cortex, consisting of superficial B follicles and the deep T cell area, and the medulla, which connects to the hilus and contains abundant macrophages and lymphatics. The entire organ is covered by a collagen-rich capsule that is penetrated by afferent lymph vessels that discharge lymph into the subcapsular sinus (SCS), a fluid-filled space that is densely lined by specialized macrophages and lymphatic endothelial cells (LECs). In *Nav1.8*$^{Cre/+}$ × *Rosa26*$^{tdTomato/+}$ × *Prox1-EGFP* animals, in which GFP is selectively expressed in LECs (Choi et al., 2011), we were able to identify intranodal sensory (i.e., tdTomato$^+$) fibers and determine their spatial relationship to the GFP$^+$ lymphatic network and their distance to the outermost boundaries of the LN (Figure S2A; STAR Methods). Any tdTomato$^+$ sensory fiber within or below the GFP$^+$ outermost LEC lining was considered intranodal. Notably, sensory fiber penetration into the LN parenchyma was relatively shallow, with an average maximum penetration distance of 112 μm ± 29 μm (mean ± SEM) below the capsule (Figure 2A; Video S2). The majority (~60%) of intranodal sensory fibers were located less than 10 μm below the surface of popLNs (Figure 2B; STAR Methods). Most of the penetrating tdTomato$^+$ fibers were located in the medulla, marked by the LEC-restricted marker LYVE-1. In contrast, tdTomato$^+$ fibers were rarely seen in the deep LN cortex (Figure 2C; Video S2).

In the more densely innervated outer cortical region of LNs, two plexuses of sensory fibers were apparent, one perivascular and the other capsular/subcapsular (Figures 2D). The perivascular fibers coursed through the medulla in tight association with arterioles and mostly terminated before these vessels gave rise to the capillary network. Sensory fibers were generally absent from postcapillary HEVs, the paracortical microvascular segments that express peripheral node addressin (PNAd), where blood-borne lymphocytes adhere and emigrate into LNs (von Andrian and Mempel, 2003; Figures 2E and S2B; Video S3). Occasionally, individual axons were observed branching away from the vasculature and meandering in the interstitial space (Figure 2E; Video S3). Fibers that formed the capsular/subcapsular network typically branched from larger perivascular axon bundles, ramified extensively in the collagen-rich capsule, and, in some cases, extended into and below the subcapsular space, making contact with CD169$^+$ SCS macrophages (Figures 2F and S2B–S2D; Video S3).

These studies indicate that the deep LN cortex, where the majority of naive lymphocytes reside, is essentially devoid of sensory innervation, whereas cells in the LN periphery, particularly those in the perivascular and subcapsular spaces, are in close proximity to sensory fibers, suggesting regionally confined functional interactions.

LN-innervating sensory neurons are heterogeneous and dominated by peptidergic nociceptors

Next we defined the composition of LN-innervating sensory neurons using scRNA-seq (Figure 3A; STAR Methods). We injected a Cre-expressing recombinant adeno-associated virus, AAV2/1-Cre (a serotype with broad tropism toward DRG neurons; Kuehn et al., 2019; Mason et al., 2010) into the right iLNs of *Rosa26*$^{LSL\text{-}tdTomato/LSL\text{-}tdTomato}$ mice carrying a Cre-dependent tdTomato reporter. Upon entry into sensory fibers, this non-replicating virus travels retrogradely to the cell body in DRGs, where virally encoded Cre recombinase induces expression of tdTomato. Following unilateral iLN injection, robust tdTomato expression was observed in neurons in the ipsilateral last thoracic (T13) and first lumbar (L1) DRGs, which supply the inguinal region (Takahashi and Nakajima, 1996; Figures 3B–3D). TdTomato labeling at the site of injection was primarily concentrated in the injected iLNs, indicating spatial confinement of the injected material (Figure S3A). However, some tdTomato$^+$ cells were also detectable in the immediate vicinity of injected LNs, raising the possibility that some sensory fibers outside of the LNs were inadvertently labeled. To control for this, we assessed the extent of retrograde labeling of DRG neurons following deliberate perinodal virus injection. Relative to intranodal injections, which resulted in robust labeling of DRG neurons (16.2 ± 2.4 cells per mouse [mean ± SEM], n = 4), very few (1.5 ± 0.6, n = 4) DRG neurons were labeled after deliberate perinodal AAV2/1-Cre injection (Figures S3B and S3C). To independently evaluate the specificity of our retrograde viral labeling strategy, we also performed intranodal injections of AAV-Flex-tdTomato in *Nav1.8*^{Cre} animals, in which

Please cite this article in press as: Huang et al., Lymph nodes are innervated by a unique population of sensory neurons with immunomodulatory potential, Cell (2021), https://doi.org/10.1016/j.cell.2020.11.028

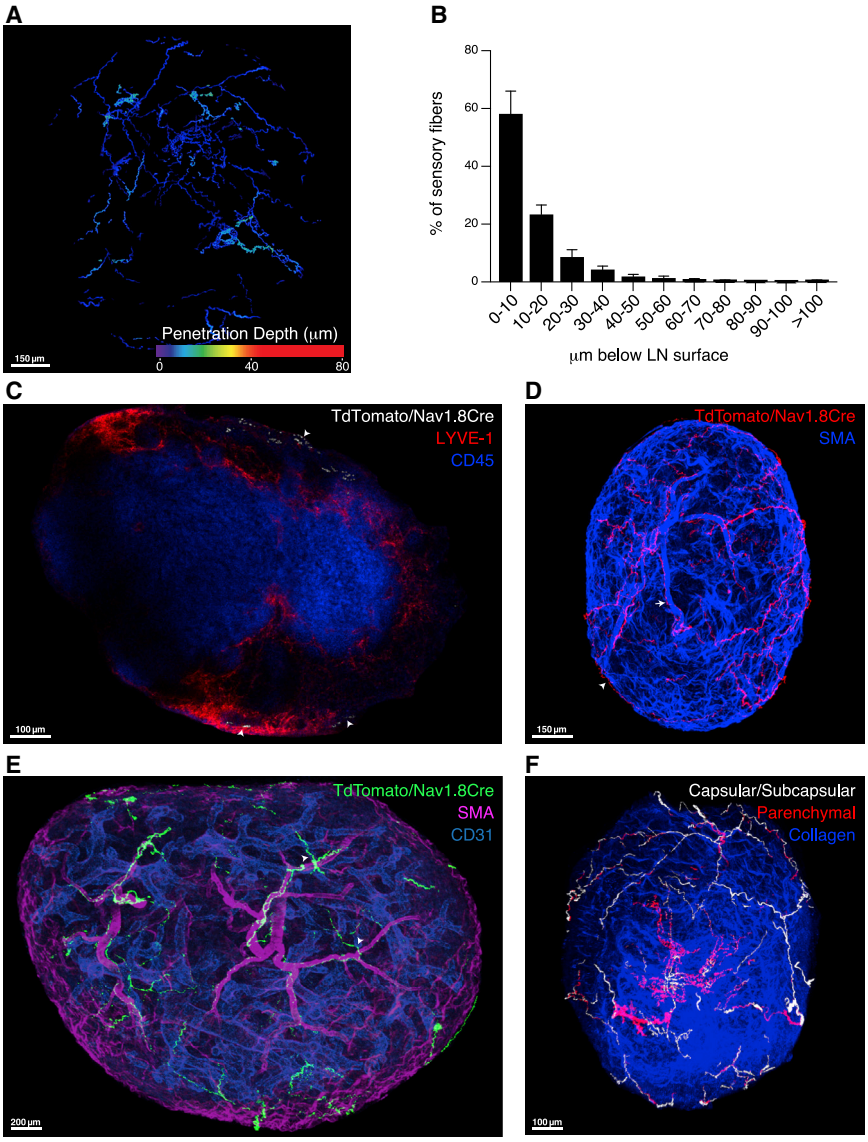

Figure 2. Spatial distribution of sensory innervation of peripheral LNs

(A) 3D reconstruction of a representative confocal image of tdTomato$^+$ sensory fibers in popLNs of *Nav1.8$^{Cre/+}$; Rosa26$^{LSL\text{-}tdTomato/+}$; Prox1-EGFP* animals color-coded by penetration depth (based on the outermost layer of GFP$^+$ LECs). Scale bar, 150 μm.

(B) Quantification of the penetration depth of tdTomato$^+$ sensory fibers (as in A) as a percentage of total intranodal sensory fibers (5 LNs, 3 mice). Error bars, SEM.

(C) Representative confocal section of whole-mount popLNs from *Nav1.8$^{Cre/+}$; Rosa26$^{LSL\text{-}tdTomato/+}$; Prox1-EGFP* animals, stained for tdTomato, LYVE-1, and CD45. Arrowheads, sensory fibers. Scale bar, 100 μm.

(D) 3D reconstruction of a representative confocal image of whole-mount popLNs from *Nav1.8$^{Cre/+}$; Rosa26$^{LSL\text{-}tdTomato/LSL\text{-}tdTomato}$* animals, stained for tdTomato and smooth muscle cell actin (SMA). Arrow, perivascular plexus; arrowhead, capsular/subcapsular plexuses. Scale bar, 150 μm.

(E) 3D reconstruction of a representative confocal image of whole-mount popLNs from *Nav1.8^{Cre}; Rosa26$^{LSL\text{-}tdTomato/LSL\text{-}tdTomato}$* animals, stained for tdTomato, SMA, and CD31. Arrow, avascular branch of the perivascular plexus. Scale bar, 200 μm.

(F) 3D reconstruction of a representative confocal image of whole-mount popLNs from *Nav1.8$^{Cre/+}$; Rosa26$^{LSL\text{-}tdTomato/+}$; Prox1-EGFP* animals, stained for tdTomato, GFP, and collagen type 1 to distinguish capsular/subcapsular and parenchymal sensory fibers. Scale bar, 100 μm.

See also Figure S2 and Videos S2 and S3.

sensory neurons express Cre recombinase. The innervation pattern of retrogradely labeled tdTomato$^+$ neurons was similar to that of tdTomato$^+$ LN-innervating sensory neurons in *Nav1.8$^{Cre/+}$* × *Rosa26$^{tdTomato/+}$* animals, confirming their identity (Figures 2D and S3D; Video S4).

We harvested ipsilateral T13 and L1 DRGs from AAV2/1-Cre-injected *Rosa26$^{LSL\text{-}tdTomato/LSL\text{-}tdTomato}$* animals, manually isolated individual tdTomato$^+$ neurons, and performed scRNA-seq on 52 LN-innervating sensory neurons (Hempel et al., 2007; Picelli et al., 2014; Trombetta et al., 2014; STAR Methods). As a control, we also profiled 31 skin-innervating neurons from 4 *Rosa26$^{LSL\text{-}tdTomato/LSL\text{-}tdTomato}$* mice that were labeled retrogradely by intradermal AAV2/1-Cre injection (Figure S3E). The specificity of retrograde labeling from the skin was demonstrated by skin-restricted axonal terminals of retrogradely labeled Nav1.8$^+$ neurons following intradermal injection of AAV2/1-Flex-EGFP into *Nav1.8^{Cre}* animals (Figure S3F) as well as lack of tdTomato labeling in draining LNs upon intradermal injection of AAV2/1-Cre into *Rosa26$^{LSL\text{-}tdTomato/LSL\text{-}tdTomato}$* animals (data not shown).

To define the molecular identity of LN-innervating sensory neurons, we examined each for expression of canonical markers known to differentiate at least 11 sensory neuron molecular subtypes (Usoskin et al., 2015; Figure 3E). As expected, the majority (96% with $\log_2(1 + \text{transcripts per million [TPMs]}) > 1$) expressed Nav1.8 (*Scn10a*), whereas few (23% with $\log_2(1 + \text{TPM}) > 1$) co-expressed TH (*Th*). Almost all LN neurons with detectable *Nav1.8* also expressed the high-affinity receptor for nerve growth factor (NGF), TrkA (*Ntrk1*), and CGRP (*Calca*), suggesting a peptidergic identity. Indeed, 88.4% ± 8.7% (mean ± SEM) of retrogradely labeled LN-innervating DRG neurons expressed CGRP by immunohistochemistry (Figure 3F). Notably, mutually exclusive expression of substance P (*Tac1*) and neurofilament heavy chain (NFH; gene name *Nefh*) in *Calca*$^+$ LN-innervating sensory neurons identified two LN-innervating peptidergic nociceptor subclasses that correspond to thermosensitive unmyelinated nociceptors and lightly myelinated Aδ nociceptors, respectively (Usoskin et al., 2015). Consistent with the heterogeneous expression of *Nefh*, a marker for medium- to large-diameter sensory neurons

Please cite this article in press as: Huang et al., Lymph nodes are innervated by a unique population of sensory neurons with immunomodulatory potential, Cell (2021), https://doi.org/10.1016/j.cell.2020.11.028

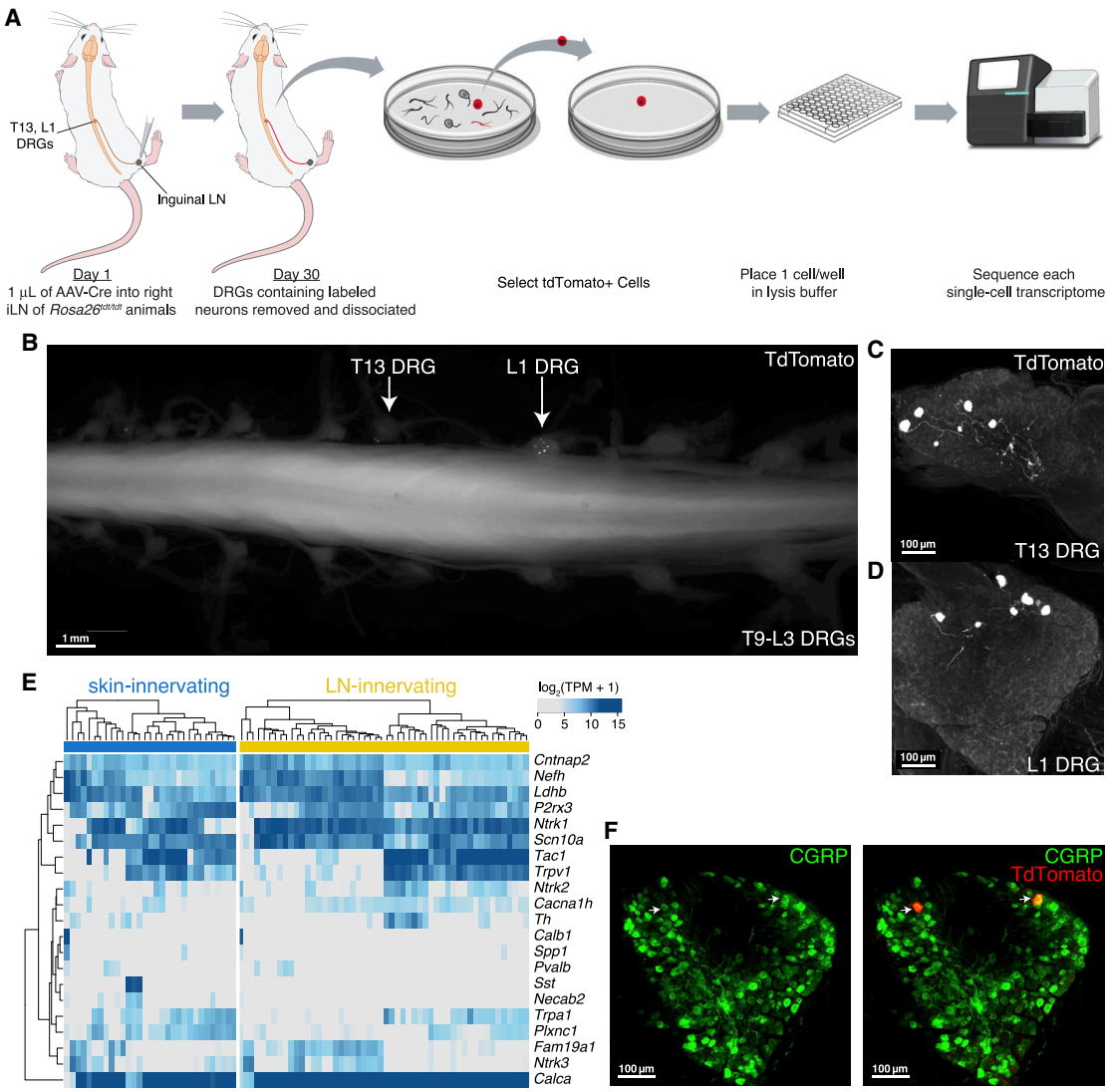

Figure 3. Retrograde labeling of LN-innervating sensory neurons for scRNA-seq

(A) Schematic of retrograde labeling from the LNs, manual cell sorting, and scRNA-seq.

(B) Representative epifluorescence image of tdTomato$^+$ retrogradely labeled iLN-innervating DRG neurons in a whole-mount spinal cord-DRG preparation without antibody amplification. Scale bar, 1 mm.

(C and D) Maximum projection view of confocal images of whole-mount ipsilateral T13 (C) and L1 (D) DRGs from (B) stained for tdTomato. Scale bars, 100 μm.

(E) Single-cell expression of neuronal subtype-specific markers.

(F) Representative confocal sections of whole-mount DRGs containing tdTomato$^+$ retrogradely labeled iLN-innervating neurons from *Rosa26*$^{LSL\text{-}tdTomato/LSL\text{-}tdTomato}$ animals following intranodal injection of AAV-Cre, stained for tdTomato and CGRP. Arrows, retrogradely labeled iLN-innervating neurons. 88.4% ± 8.7% (mean ± SEM) tdTomato+ sensory neurons express CGRP (44 neurons, 3 mice). Scale bars, 100 μm.

See also Figure S3 and Video S4.

with myelinated axons (Rice and Albrecht, 2008), whole-mount DRG staining revealed that retrogradely labeled LN-innervating sensory neurons were heterogeneous with respect to soma size. This diversity of cell dimensions matched the range of diameters observed in CGRP$^+$ neurons, known to be heterogeneous in size (Lawson et al., 2002; Figure S3G). Furthermore, NFH$^+$ myelinated and NFH$^-$ unmyelinated sensory fibers were abundant in the perivascular and capsular/subcapsular space of LNs (Figure S3H). Because soma size and myelination status are commonly used, together with other electrophysiological properties, to classify DRG neurons into functional subtypes (Wood et al., 2018), sensory neurons innervating LNs are likely composed of qualitatively distinct neuronal subtypes.

We next sought to more broadly contextualize our scRNA-seq profiles of LN-innervating sensory neurons by integrated analysis with two published scRNA-seq DRG atlases: Usoskin et al. (2015) (Figure S4A) and Sharma et al. (2020) (Figures 4A and 4B; STAR Methods). LN-innervating sensory neurons displayed closest

similarity to the peptidergic neurons defined by Usoskin et al. (2015) (Figures S4A and S4B) and the 4 peptidergic subtypes (called CGRP-η, -ξ, -γ, and -ε) described by Sharma et al. (2020) (Figure 4C). In comparison, skin-innervating neurons displayed transcriptomic phenotypes consistent with diverse neuronal subtypes, including stomatostatin $(SST)^+$ pruriceptors, $MRGPRD^+$ polymodal nociceptors, various low-threshold mechanoreceptor (LTMR) subtypes, and the $CGRP^+$ peptidergic subtypes represented by LN-innervating neurons. Next, we directly classified LN-innervating or skin-innervating sensory neurons relative to the 11 DRG subtypes in the Usoskin et al. (2015) atlas and the 15 in the Sharma et al. (2020) atlas (STAR Methods; Figures 4D and S4C). We recovered 4 transcriptionally distinct neuronal classes in our dataset, called neuron types 1–4. Each neuron type was represented, albeit in different proportions, in LN-innervating and skin-innervating sensory neurons, demonstrating intrinsic heterogeneity in sensory neurons innervating the same target as well as innervation target-dependent differences in subtype composition ($p < 0.001$ by Pearson's chi-square test; Figure 4E). Using differential gene expression analysis, we discovered unique gene modules that cleanly define each neuron type (Figure 4F; Table S1). These were consistent with the general phenotypic descriptions of the corresponding subtypes in Sharma et al. (2020) and Usoskin et al. (2015). Together, these data suggest that LN-innervating sensory neurons are transcriptionally heterogeneous but strongly biased toward peptidergic phenotypes.

LN-innervating sensory neurons are molecularly distinct from their skin-innervating counterparts

We next compared LN- and skin-innervating sensory neurons to define gene programs that may support target tissue-specific development and function. We identified 101 and 156 genes that were significantly upregulated in LN-innervating and skin-innervating neurons, respectively (Figures 5A, 5B, S4D, and S4E; Table S1). Analysis of differentially expressed (DE) genes and gene ontologies revealed that LN- and skin-innervating sensory neurons differ with respect to many surface ion channels and synaptic proteins (LN-specific: *Trpc4*, *Trpm8*, *Kcnh5*, and *Ache*; skin-specific: *Trpc3*, *Trpc6*, *Kctd16*, *Synpr*, *Gabra1*, and *Kcnk12*), as well as secreted and cell surface molecules, which may reflect target-specific modes of communication between sensory neurons and their microenvironment (Figures 5C, 5D, and S4F–S4H). LN-innervating sensory neurons overexpressed genes with inflammatory or immune cell interacting activities, including *Tbxa2r*, *Il33*, *Ptgir*, and *Cd1d*, suggesting additional immunological functions, including the capacity to monitor LN inflammatory state by sensing inflammation-induced prostanoids that may reach LNs via lymph or that are produced directly in reactive LNs (Figures 5C and 5D; Table S1; Andoh et al., 2007; Bley et al., 1998; Wacker et al., 2002).

To identify candidate markers for LN-innervating neurons, we compared these neurons to skin-innervating neurons and the full diversity of sensory neurons captured in the Sharma et al. (2020) atlas (Table S1; Figure 5E). We validated *Ptgir* and *Prokr2*, two markers with different sensitivity and specificity, as LN-innervating sensory neurons markers (Figures 4F, S4D, and S4E) using RNAscope-based multiplexed fluorescence *in situ* hybridization analysis of *Ptgir*, *Prokr2*, and *tdTomato* in DRGs containing $tdTomato^+$ retrogradely labeled LN- or skin-innervating neurons (Figures 5F and S4I–S4L). Thus, sensory neurons innervating LNs are marked by a distinct transcriptional profile that includes high expression of *Ptgir* and *Prokr2*.

Peripheral challenge with pro-inflammatory TLR agonists expands sensory innervation of draining LN

Previous work has shown that sensory innervation often increases at sites of inflammation (Chakrabarty et al., 2011; Pongratz and Straub, 2013), suggesting that sensory neuronal networks may undergo remodeling when exposed to inflammatory signals. Indeed, LN-innervating sensory neurons expressed several Toll-like receptors (TLRs), innate sensors of pro-inflammatory molecular patterns associated with pathogens or tissue damage (Akira et al., 2006; Janeway and Medzhitov, 2002), including *Tlr4* (40% of LN-innervating neurons assayed), *Tlr5* (25%), *Tlr3* (15%), and *Tlr6* (6%) (Figure S4M). Thus, we assessed the structural plasticity of sensory innervation of LNs in response to lipopolysaccharide (LPS), a prototypic TLR4 ligand (Chow et al., 1999) by comparing the innervation patterns of reactive and contralateral PBS-draining popLNs on day 3 following LPS footpad injection in $Nav1.8^{Cre/+} \times Rosa26^{LSL\text{-}tdTomato/LSL\text{-}tdTomato}$ mice (Figures 5G–5J). LPS challenge consistently led to a selective 2-fold increase in total sensory fiber content in draining LNs ($p < 0.05$; Figures 5G, 5I, and 5J). This increase in sensory innervation tightly paralleled a concomitant increase in total LN volume, and sensory fiber density remained essentially constant regardless of the inflammatory state of the LN (Figures 5H and S4N). To determine whether the expansion of sensory innervation upon peripheral TLR exposure required direct recognition of TLR ligand, we also injected mice subcutaneously with Pam3CSK4, a ligand for TLR1 and TLR2 (Jin et al., 2007), which are both absent from LN sensory neurons (Figure S4M). Compared with LPS-treated mice, Pam3CSK4 elicited not only similar LN expansion (Figure S4O) but also a similar enhancement of sensory innervation (Figures 5K–5N). Therefore, in certain cases, expanded innervation likely arises through indirect sensing of TLR-induced secondary inflammatory mediators, potentially involving communication with other LN-resident cell types and/or detection of secreted factors from the periphery.

scRNA-seq of LN cells nominates interacting partners of LN-innervating sensory neurons

To identify potential interaction partners for LN-innervating sensory neurons, we next systematically mapped putative cellular interactions between sensory neurons and the various cell types that reside in LNs. First we generated a single-cell transcriptomic atlas of steady-state murine iLNs using Seq-Well (Aicher et al., 2019; Gierahn et al., 2017; STAR Methods). To increase coverage of rare LN cell types (i.e., non-T and non-B cells) that populate the preferentially innervated LN periphery, we profiled paired LN samples from before and after immuno-magnetic depletion of T and B cells (Figure 6A). Following quality filtering and preprocessing, we recovered libraries from 9,622 single cells. Using established methods for unbiased cell type identification, we uncovered 24 distinct cell types representing all major known lymphoid, myeloid, and stromal LN populations (Butler

Please cite this article in press as: Huang et al., Lymph nodes are innervated by a unique population of sensory neurons with immunomodulatory potential, Cell (2021), https://doi.org/10.1016/j.cell.2020.11.028

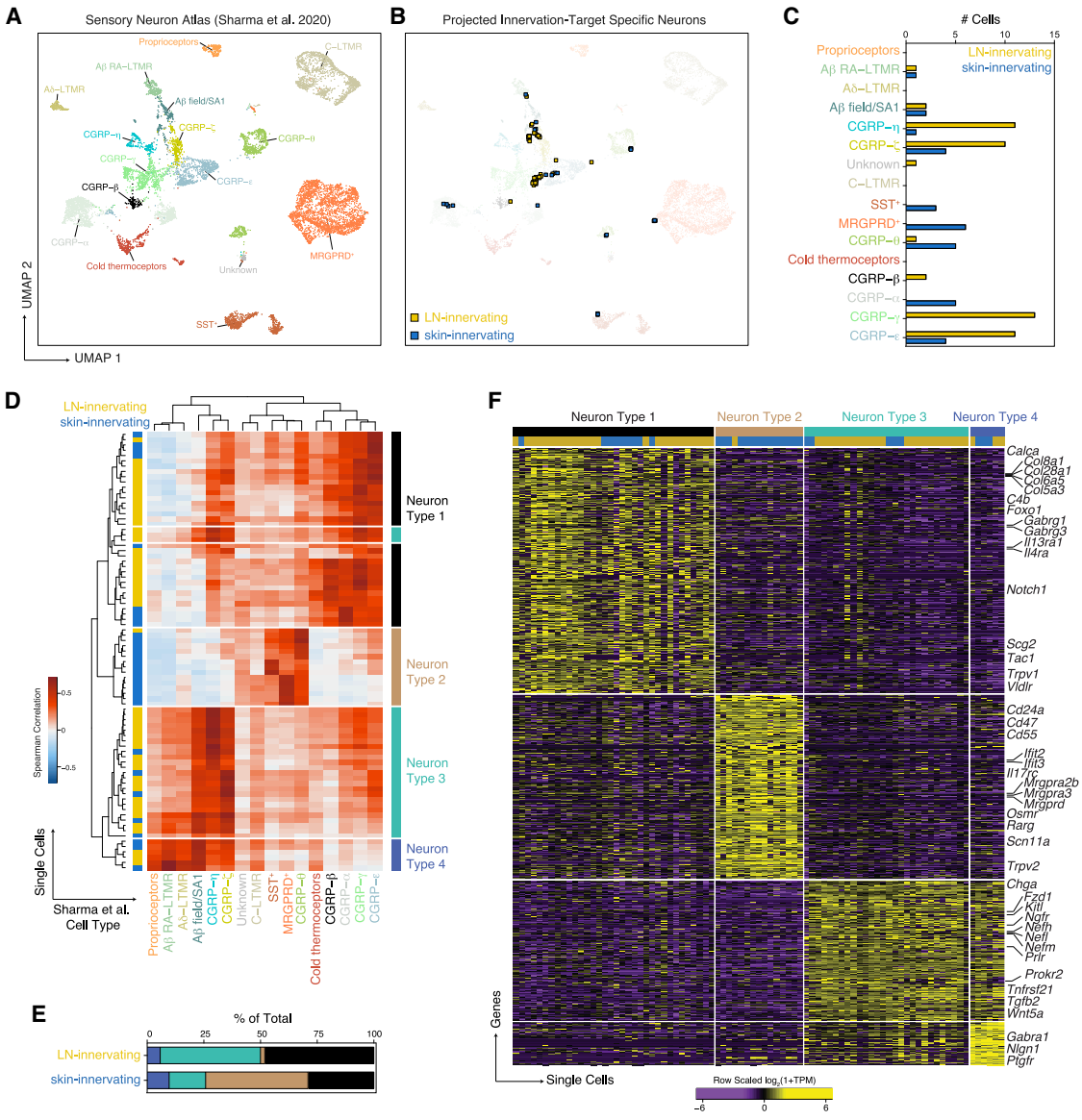

Figure 4. LN-innervating sensory neurons are primarily peptidergic nociceptors

(A) Uniform manifold approximation and projection (UMAP) of the Sharma et al. (2020) atlas, colored by previously defined cell types.

(B) UMAP as in (A), with LN-innervating (yellow squares) and skin-innervating (blue squares) neurons projected.

(C) Predicted cell types for LN-innervating neurons (yellow) or skin-innervating neurons (blue).

(D) Spearman correlation between LN- or skin-innervating neurons and subsets from the Sharma et al. (2020) atlas. Hierarchical clustering divides LN- and skin-innervating neurons into 4 subtypes: neuron type 1 (CGRP-like, black); neuron type 2 (CGRP-θ, MRGPRD$^+$ polymodal nociceptor-, SST$^+$ pruriceptor-like, tan); neuron type 3 (mixed CGRP-like, LTMR-like, turquoise); and neuron type 4 (mixed CGRP-ξ, -η, LTMR, proprioceptor-like, dark blue).

(E) Distribution of neuron types 1–4 by innervation target.

(F) DE genes (Holm-adjusted $p < 0.01$).

See also Figure S4 and Tables S1 and S2.

et al., 2018; Figures 6B, 6C, and S5A–5P; Table S2; STAR Methods).

To determine the relative likelihood of each LN cell type interacting with LN-innervating sensory neurons, we analyzed the expression of ligand-receptor pairs across our two single-cell datasets (Cohen et al., 2018; Smillie et al., 2019; Vento-Tormo et al., 2018; Drokhlyansky et al., 2019). We reasoned that interacting cells might rely on inter-cellular ligand-receptor pairs for signaling crosstalk and/or physical association through interaction of membrane-anchored proteins or via secreted ligands binding to receptors. Accordingly, the number of co-expressed ligand-receptor cognates between a LN-innervating neuron and any given LN cell type was used to estimate the "interaction potential" for that LN cell type (Figures 6D, 6E, and S6A; STAR

Please cite this article in press as: Huang et al., Lymph nodes are innervated by a unique population of sensory neurons with immunomodulatory potential, Cell (2021), https://doi.org/10.1016/j.cell.2020.11.028

CellPress

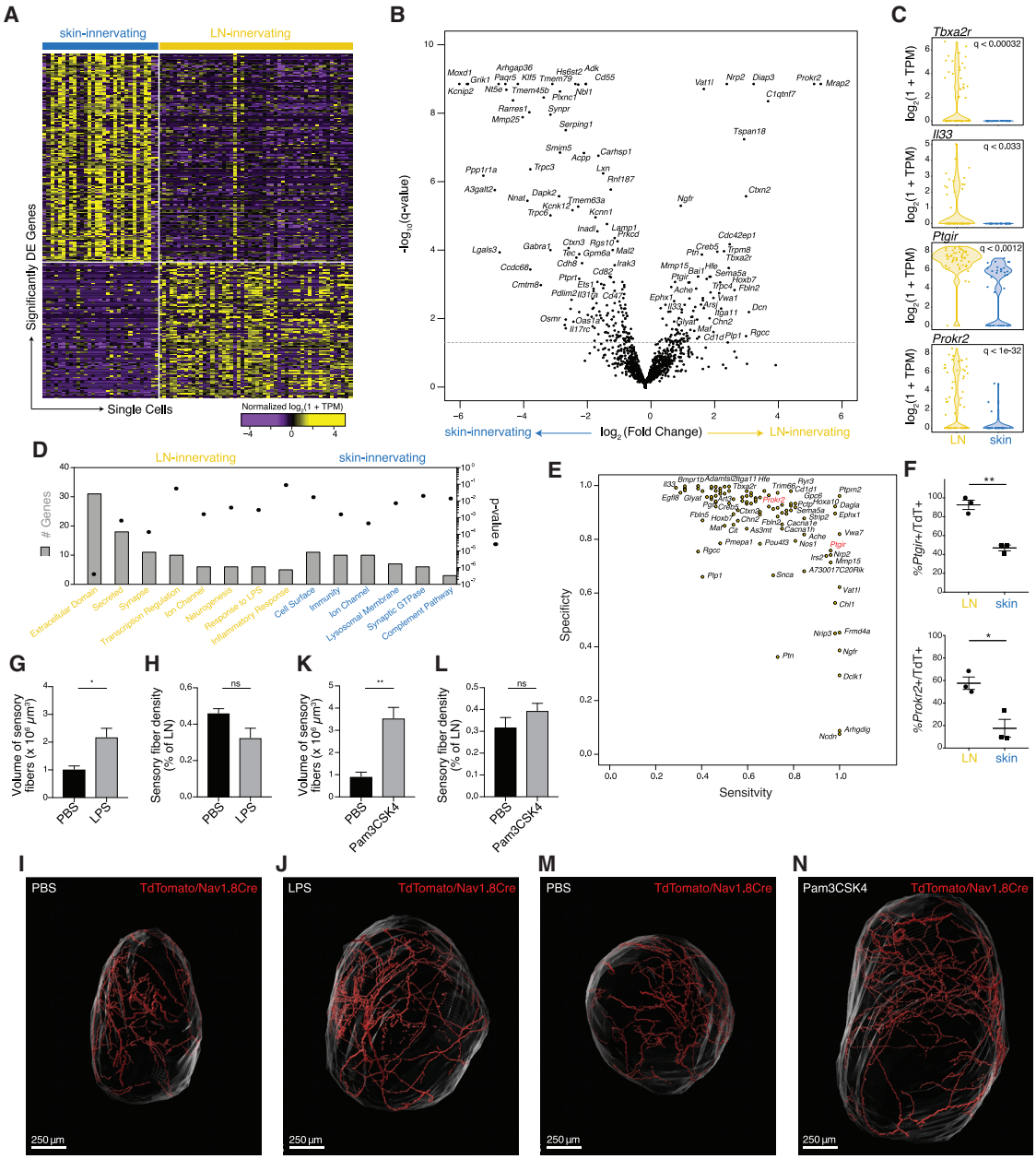

Figure 5. LN-innervating sensory neurons express unique defining markers and functional pathways

(A) Heatmap of significantly DE genes (Holm-adjusted p (q) < 0.05).

(B) Volcano plot. Dashed line: q = 0.05.

(C) Violin plots of select genes.

(D) Enriched gene ontologies of genes upregulated in LN-innervating neurons (yellow) or skin-innervating neurons (blue). Left y axis, number of DE genes; right y axis, p value (Fisher's exact test).

(E) Identification of sensitive and specific markers for LN-innervating neurons.

(F) Quantification of *Ptgir* and *Prokr2* expression in *tdTomato*$^+$ retrogradely labeled LN- or skin-innervating neurons (TdT$^+$) as the percentage of *tdTomato*$^+$ neurons that are *Ptgir*$^+$ or *Prokr2*$^+$ by RNAscope. 3 mice, **p = 0.0014, *p = 0.0142, by unpaired t test. Error bars, SEM.

(G and H). Volume (G) and density (H) of sensory innervation of popLNs 3 days after PBS or LPS footpad injection. n = 6 LN/group, 6 animals. Volume, *p = 0.0121; density, not significant (ns), p = 0.0503 by Welch's t test. Error bars, SEM.

(I and J) Representative rendered surfaces for tdTomato$^+$ sensory fibers (red) in popLNs (gray) in *Nav1.8*$^{Cre/+}$ × *Rosa26*$^{LSL\text{-}tdTomato/LSL\text{-}tdTomato}$ mice following footpad injection of PBS (I) or LPS (J). Scale bars, 250 μm.

(legend continued on next page)

Methods). The non-immune compartment (non-endothelial stroma [NES], blood vessel ECs [BEC], high ECs [HEC], and two LEC subsets [LEC 1 and LEC 2]) exhibited the highest interaction potential among all LN cell types and reached statistical significance compared with randomized data (Figure 6E; S6B–S6E; STAR Methods). To take into consideration the directionality of the cognate pairs, we partitioned ligand-receptor pairs into three categories: (1) the gene product is secreted by LN-innervating neuron, (2) secreted by LN-resident cell types, or (3) non-directional/unknown directionality, often corresponding to interactions between two membrane-tethered proteins. Considering only molecules secreted by LN-innervating neurons (category 1), LEC 2, LEC 1, BECs, HECs, and NESs expressed a significantly elevated abundance of cognate receptors (Figure 6F). Given a strong enrichment for peptidergic signatures among LN-innervating neurons, we assessed expression of the corresponding neuropeptide receptors among LN cell types (Figure S6F). *Ramp1*, which, together with *Calcrl*, a ubiquitously expressed gene among LN cell types, forms the CGRP receptor (McLatchie et al., 1998), was more highly expressed in innate immune cell types such as mast cells and DCs, suggesting that LN-innervating sensory neurons may signal to select myeloid cells via CGRP. The receptors for other neuropeptides, *Tac1*, *Adcyap1*, and *Gal* (*Tacr1*, *Adcyap1r1*, and *Galr2* and *Galr1*, respectively), were uniquely expressed by NESs, identifying substance P, PACAP, and galanin as potential signaling mediators between LN-innervating neurons and NESs. Notably, the recently identified alternative substance P receptor *Mrgprb2* was almost exclusively and highly expressed in LN mast cells, suggesting a substance P/Mrgprb2-mediated sensory neuron-mast cell connection analogous to what has been described in the skin (Green et al., 2019). In contrast, classic neuropeptides did not appear to be a primary mode of communication between LN-innervating sensory neurons and LN ECs.

Next we analyzed the cognate receptors and ligands responsible for high interaction potentials among the stromal compartments (Figures S6G and S6H). Predicted interaction between LN-innervating neurons and NESs was strongly driven by extracellular matrix components (*Col3a1*, *Col5a2*, *Col5a1*, *Col6a1*, *Col6a2*, *Col6a3*, *Col1a2*, *Col1a2*, *Lama2*, *Thbs2*, and *Fn1*) and growth factors/chemokines with diverse roles in neuronal development and function (*Vegfa*, *Ptn*, *Mdk*, and *Cxcl12*) (González-Castillo et al., 2015; Mackenzie and Ruhrberg, 2012; Mithal et al., 2012; Winkler and Yao, 2014) as well as receptors for growth factors known to regulate fibroblast proliferation and differentiation (*Pdgfra*, *Pdgfrb*, and *Ntrk2*) (Andrae et al., 2008; Palazzo et al., 2012). Similarly, the putative interactions between BECs and HECs with LN-innervating sensory neurons were potentially bidirectional, as evidenced by expression of a distinct set of extracellular matrix and cell adhesion molecules (*Lama5*, *Itga5*, and *Hspg2*), receptors of central signaling pathways for vascular development (*Flt1*, *Notch4*, and *Fzd4*) (Mack and Iruela-Arispe, 2018; Shibuya, 2011; Ye et al., 2010), and classic axon guidance molecules with known roles in leukocyte-endothelial adhesion, angiogenesis, and arterial-venous differentiation (*Sema3f*, *Sema7a*, *Nrp1*, *Plxnd1*, *Efnb1*, and *Epha4*) (Adams and Eichmann, 2010; Larrivée et al., 2009). Thus, our single-cell profiling identified stromal cells as the most likely interacting partners of LN-innervating sensory neurons and revealed potential communication modalities for cell-cell interactions.

Optogenetics-assisted validation of local targets of LN-innervating sensory neurons

To directly test functional interactions between LN-innervating sensory neurons and LN cells, we systematically interrogated the effects of acute activation of LN-innervating sensory neurons on LN-resident cell gene expression by integrating optogenetic stimulation with scRNA-seq (STAR Methods). To specifically activate LN-innervating sensory neurons *in vivo*, we used *Nav1.8*$^{Cre/+}$ × *Rosa26*$^{ChR2\text{-}eYFP/+}$ (ChR2+) mice in which Nav1.8-lineage neurons expressed ChR2 (Deisseroth, 2011). The sensory neurons innervating surgically exposed iLNs were activated selectively using blue light (473 nm) through an optical fiber directed at a region around the subiliac artery adjacent to the hilus, the predominant site where sensory nerve bundles enter the iLNs (Figures 1A, 1B, 7A, and S7A).

Following 3 h of pulsed light exposure, iLNs from the stimulated and unstimulated sides were processed in parallel and analyzed using Seq-Well (Figures 7A and S7B). To isolate the ChR2-dependent effect of optogenetic activation, iLNs in a separate cohort of *Nav1.8*$^{Cre/+}$ × *Rosa26*$^{eYFP/+}$ (ChR2$^-$) animals, which expressed eYFP instead of ChR2 in Nav1.8-lineage neurons, were subjected to identical photostimulation, dissociation, cellular enrichment, and scRNA-seq analysis (STAR Methods). The changes in cellular composition and gene expression in ChR2$^+$, but not ChR2$^-$ (i.e., eYFP$^+$), animals were considered true effects of local stimulation of LN sensory fibers (Figure S7C; STAR Methods). Our final dataset included 4 ChR2$^+$ mice and 3 ChR2$^-$ mice, two iLNs per mouse (one light-exposed, one control), and contained 10,364 cells (STAR Methods; Figures 6B, 7B, S7D). Compared with the contralateral control iLN, we did not observe significant light-induced changes in the abundance of any cell type in ChR2$^+$ or ChR2$^-$ animals, nor did we observe changes in LN cellularity upon light exposure (Figures S7E and S7F), indicating that neither the surgical/photostimulation procedures nor activation of LN-innervating sensory neurons dramatically altered the ecosystem of the exposed iLNs over the relatively short timescale of 3 h.

We next compared gene expression between the same cell types in ChR2$^+$ light-exposed LNs and ChR2$^+$ contralateral control LNs (Table S3; STAR Methods). Remarkably, robust ChR2-dependent transcriptional changes were readily detected in a subset of cell types—LEC 2, BECs, NESs, neutrophil 2, and natural killer (NK) cells—indicating selective modulatory capabilities of LN-innervating sensory neurons (Figures 7C–7F and S7G).

(K and L) Volume (K) and density (L) of sensory innervation of popLNs 3 days after PBS or Pam3CSK4 footpad injection. n = 4 LN/group, 4 animals. Volume, **p = 0.0076; density, ns, p = 0.2249 by Welch's t test. Error bars, SEM.

(M and N) Representative rendered surfaces for tdTomato$^+$ sensory fibers (red) within popLNs (gray) in *Nav1.8*$^{Cre/+}$ × *Rosa26*$^{LSL\text{-}tdTomato/LSL\text{-}tdTomato}$ mice following footpad injection of PBS (M) or Pam3CSK4 (N). Scale bars, 250 μm.

See also Figure S4 and Table S1.

Please cite this article in press as: Huang et al., Lymph nodes are innervated by a unique population of sensory neurons with immunomodulatory potential, Cell (2021), https://doi.org/10.1016/j.cell.2020.11.028

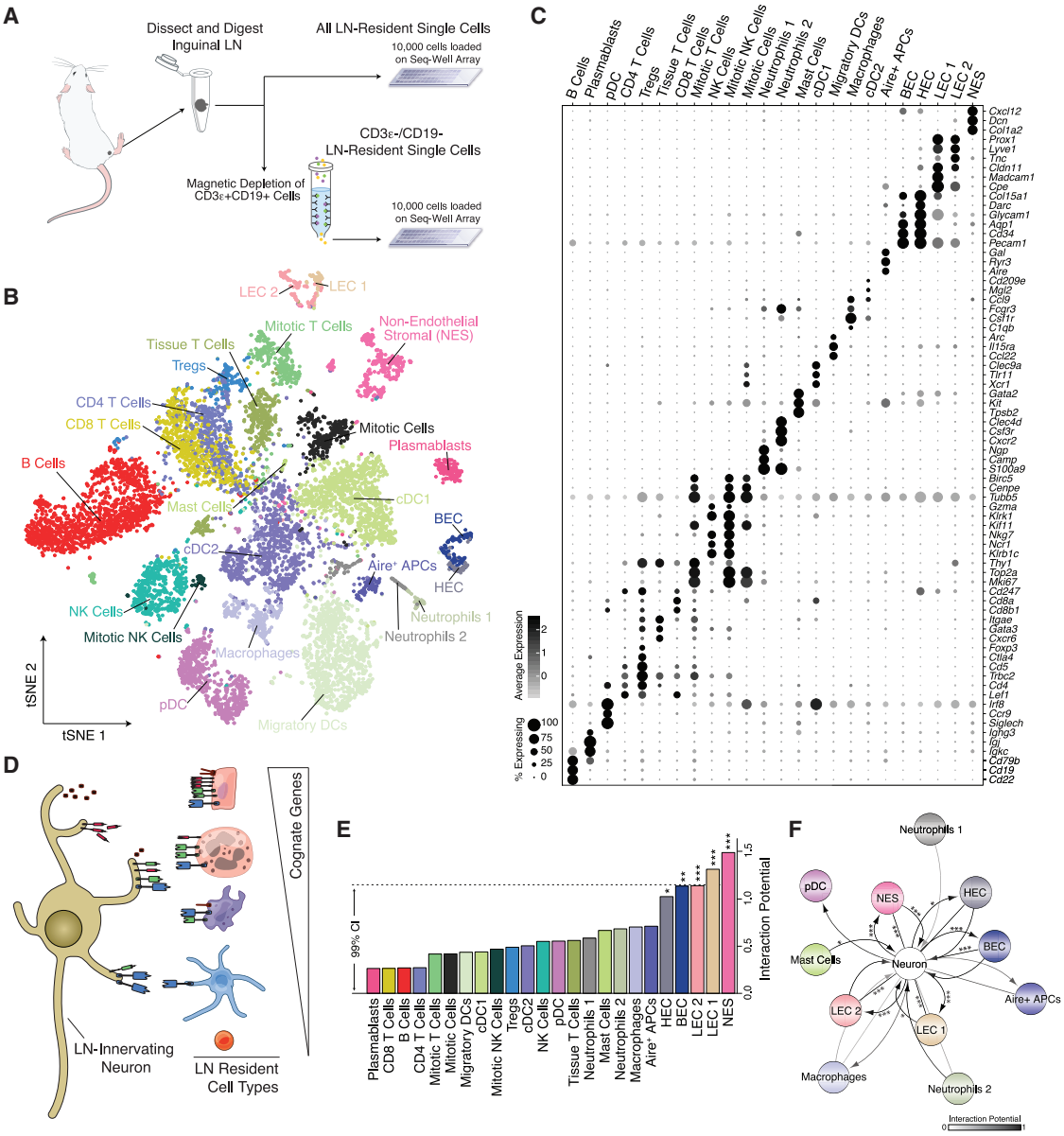

Figure 6. Single-cell transcriptomic profiling of iLN cells nominates likely interaction partners of iLN-innervating sensory neurons

(A) Schematic for iLN isolation, dissociation, and enrichment for rare iLN cell types.

(B) tSNE of 9,662 cells, colored by cell type.

(C) Dot plot of cell-type-specific genes, false discovery rate (FDR)-corrected $p < 0.001$ by likelihood ratio test.

(D) Schematic of receptor-ligand analysis.

(E) Interaction potential by cell type. Dashed lines, 99% confidence interval over permuted data.

(F) Cell-cell interaction network. Arrows from the "neuron" node: secreted molecules produced by LN-innervating neurons; arrows to the "neuron" node: secreted molecules produced by LN-resident cell types; Un-directed lines: ligand-receptor pairs with unknown directionality or bidirectional effects.

*$p < 0.05$, **$p < 0.01$, ***$p < 0.001$ by permutation test. See also Figures S5 and S6 and Tables S3 and S4.

Further, we found that the magnitude of change in gene expression (as measured by the number of DE genes) was correlated significantly with the overall interaction potential (Figure 6E) derived from the steady-state iLN atlas (Pearson correlation = 0.52, $p < 0.03$; Figures 7G and S7G).

The most affected LN cell type was LEC 2, based on the abundance of DE genes with substantial effect sizes (Figure S7G). LEC 2 were also the cell type with the highest overall interaction potential (Figures 6E, and 7G) and were characterized by high expression of potential molecular pathways for bidirectional

Please cite this article in press as: Huang et al., Lymph nodes are innervated by a unique population of sensory neurons with immunomodulatory potential, Cell (2021), https://doi.org/10.1016/j.cell.2020.11.028

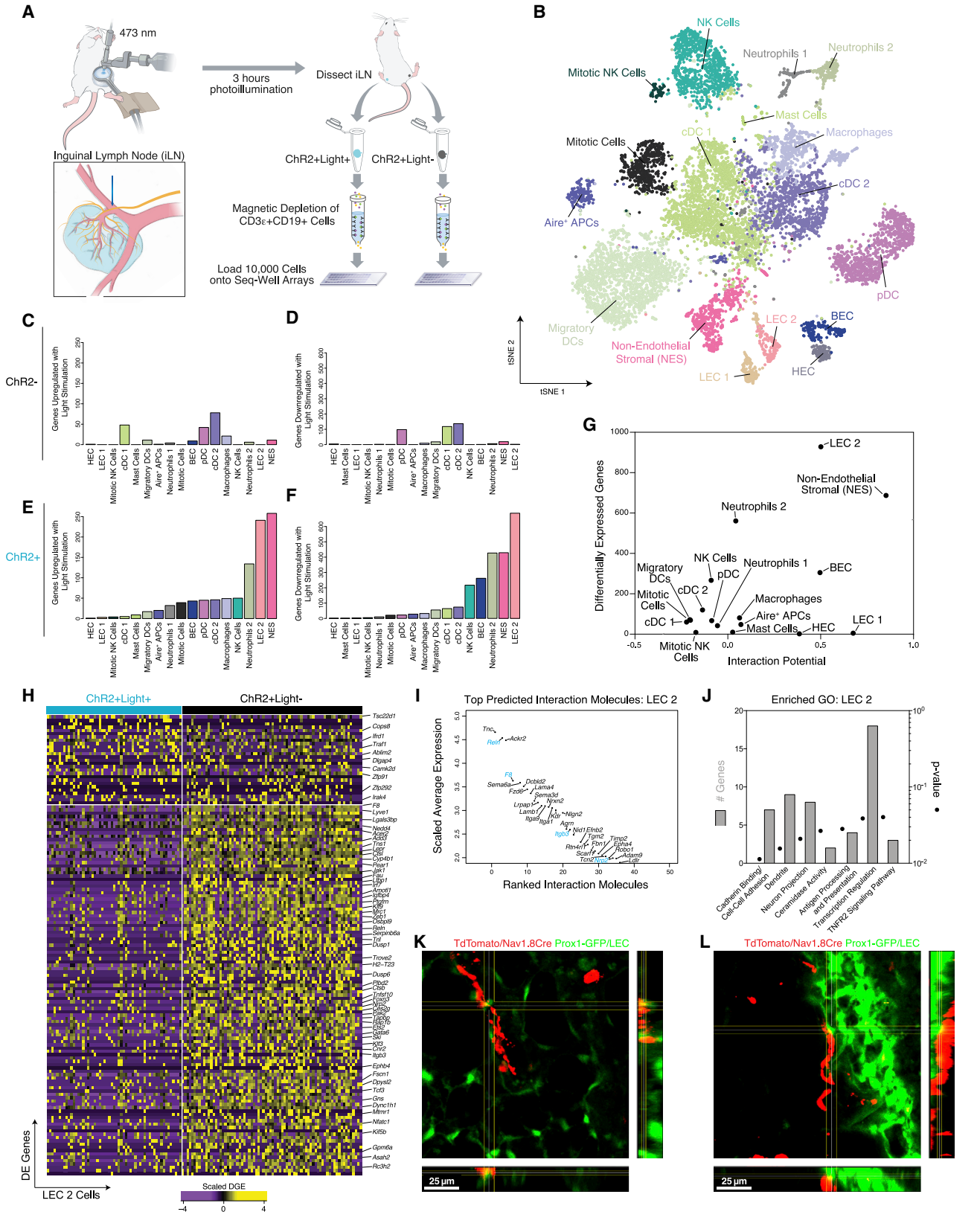

(legend on next page)

interaction with LN-innervating neurons, including extracellular matrix molecules (*Tnc*, *Fbn1*, and *Nid1*), synaptic proteins (*Agrn*, *Nrxn2*, and *Nlgn2*) (Südhof, 2018; Wu et al., 2010), and axon guidance molecules known to regulate lymphangiogenesis (*Efnb2*, *Nrp2*, and *Robo1*) (Vaahtomeri et al., 2017; Yang et al., 2010; Figure 7I). Interestingly, some interaction-capable molecules, such as *Reln*, *F8*, *Itgb3*, and *Nrp2*, were downregulated following neuronal stimulation, suggesting a potential negative feedback loop that may act to maintain or restore homeostasis by limiting the effect of neuronal stimulation on LEC 2 when initiated (Figure 7I). Among neuronal stimulation-induced gene expression changes in LEC 2, which were dominated by downregulation, there was overrepresentation of genes in multiple pathways involved in neuronal synapses and dendrite projection, ceramidase activity, cathepsin expression, and antigen processing and presentation and multiple transcriptional regulators, including *Gata6*, *Ets2*, *Irf7*, and *Nfatc1* (Figure 7J). We observed a general trend toward downregulation of LEC-enriched genes, including key regulators of lymphatic development and patterning (e.g., *Reln*, *Nrp2*, *Ephb4*, *Nfatc1*, and *Lyve1*), as well as angiogenic molecules (e.g., *Dlg1* and *Glul*), suggesting anti-angiogenic and/or anti-lymphangiogenic action of LN-innervating sensory neurons (Cho et al., 2019; Eelen et al., 2018; Kulkarni et al., 2009; Lutter et al., 2012; Vaahtomeri et al., 2017; Wu et al., 2014; Zhang et al., 2015). Moreover, downregulation of ceramidases (i.e., *Acer2* and *Asah2*, implicated in production of sphingosine-1-phosphate [S1P] in LECs, a major source of S1P in lymph) may affect lymphocyte egress from LNs, a process known to be under the control of adrenergic nerves (Mao and Obeid, 2008; Nakai et al., 2014; Pappu et al., 2007; Pham et al., 2010). Consistent with the observation that LEC 2 exhibited the largest neuronal activation-evoked transcriptional changes, direct contact between sensory nerves and LECs was observed frequently in the medulla and on the ceiling of the SCS (Figures 7K and 7L). These data further suggest that sensory neurons innervating LNs, when activated, may rapidly modulate the non-immune compartment to influence LN composition and/or function.

DISCUSSION

Despite their critical roles in regulating immunological processes in barrier tissues and the spleen (Chavan et al., 2017; Ordovas-Montanes et al., 2015), neuroimmune interactions, particularly those involving somatosensory neurons, have yet to be studied systematically in LNs. Here we directly addressed this gap in knowledge by analyzing the morphological, molecular, and functional attributes of the sensory neurons that innervate peripheral LNs. Our study identifies a sensory neuron-stroma axis in LNs as a previously unappreciated circuit of peripheral neuroimmune communication.

Previous light and electron microscopic studies have revealed the localization of peptidergic fibers in LNs (Felten et al., 1985; Fink and Weihe, 1988). However, the extent to which those fibers reflect sensory innervation had not been assessed directly. Here we demonstrate the definitive presence of sensory innervation in LNs. We found that *bona fide* sensory fibers organized into two nerve plexuses: one perivascular and another capsular/subcapsular. The perivascular plexus is particularly concentrated in the medulla and preferentially associated with arterioles and medullary LECs, whereas fibers in the capsular/subcapsular plexus are in close contact with other LN-resident cells, such as SCS macrophages and LECs. By using a whole-mount immunolabeling protocol, we reliably identified and visualized in 3D the entire network of neuronal fibers to quantitatively describe LN neuronal architecture. Through genetic labeling and retrograde tracing of LN sensory innervation, we performed unbiased morphological characterization of this heterogeneous neuronal population.

Our analysis revealed that sensory fibers are enriched in the LN periphery, a location prone to inflammation-induced mechanical, chemical, and cellular changes, suggesting a potential role of those neurons as local sentinels of LN activation. Consistent with this idea, we observed sensory hyperinnervation of LNs as a response to TLR stimulation at a distal site, potentially contributing to heightened pain sensitivity in certain types of infection. Although the exact type(s) of stimuli LN sensory neurons are tuned to and the nature of the neuronal response to diverse challenges have yet to be defined, there are multiple plausible sensing mechanisms through which LN-innervating sensory neurons could detect changes in immune status. For example, immune challenges in the periphery often result in local production of inflammatory mediators, such as tumor necrosis factor alpha (TNF-α) or IL-1β, that may become lymph-borne and directly stimulate or sensitize LN-innervating sensory neurons via their cognate cytokine receptors; i.e., TNFR1 (*Tnfrsf1a*) or IL-1R (*Il1r1*), respectively. It is also likely that sensory fibers, particularly those embedded in the LN capsule, can sense changing mechanical forces as a result of inflammation-induced LN expansion. Indeed, most DRG neurons display mechanosensitivity, albeit to different

Figure 7. Optogenetics-assisted identification of potential postsynaptic cellular targets of LN-innervating sensory neurons

(A) Schematic of optogenetic stimulation of LN-innervating neurons and cell isolation for scRNA-seq.

(B) tSNE of 10,364 cells (light-stimulated and control LNs in ChR2$^+$ and ChR2$^-$ animals), colored by cell type.

(C–F) DE genes with FDR-adjusted $p < 0.05$ and Cohen's effect size > 0.2, separated by cell type: (C) ChR2$^-$ (control) mice, upregulated by light stimulation; (D) ChR2$^-$ (control) mice, downregulated by light stimulation; (E) ChR2$^+$ (experimental) mice, upregulated by light stimulation, omitting genes also induced in ChR2$^-$ (control) mice; (F) ChR2$^+$ (experimental) mice, downregulated by light stimulation, omitting genes also repressed in ChR2$^-$ (control) mice.

(G) Interaction potential versus abundance of DE genes (Pearson correlation = 0.52; $p = 0.03$).

(H) Heatmap of DE genes between LEC 2 in light-stimulated versus unstimulated LNs in ChR2$^+$ mice.

(I) Top candidate neuron-interacting molecules in LEC 2 from steady-state LNs (Figure 6). Blue, DE with neuronal stimulation.

(J) Enriched gene ontologies in LEC 2 following neuronal stimulation. Left y axis, number of DE genes; right y axis, p value (Fisher's exact test).

(K and L) Section view of a representative two-photon micrograph of physical contact between tdTomato$^+$ sensory fibers (red) and GFP$^+$ LECs (green) in the medulla (K) and on the ceiling of SCS (L) of whole-mount popLNs from *Nav1.8$^{Cre/+}$; Rosa26$^{LSL\text{-}tdTomato/+}$; Prox1-EGFP* animals. Scale bars, 25 μm.

See also Figure S7 and Table S3.

Please cite this article in press as: Huang et al., Lymph nodes are innervated by a unique population of sensory neurons with immunomodulatory potential, Cell (2021), https://doi.org/10.1016/j.cell.2020.11.028

degrees (Drew et al., 2002; Hu and Lewin, 2006; Lewin and Stucky, 2000; McCarter et al., 1999). Notably, LN-innervating sensory neurons are likely particularly sensitive to mechanical stimuli experienced in the LN periphery because most express high levels of mRNA for the mechanically gated ion channel *Piezo2*, the major mechanotransducer for touch, proprioception, baroreception, and airway stretch (Nonomura et al., 2017; Ranade et al., 2014; Woo et al., 2015; Zeng et al., 2018). There is also growing evidence of direct activation of sensory neurons by infectious pathogens. For example, nociceptors in barrier tissues have been shown to detect bacterial products, such as pore-forming toxins (PFTs), N-formyl peptides, and endotoxin (Blake et al., 2018; Chiu et al., 2013; Diogenes et al., 2011; Meseguer et al., 2014). Conceivably, intact microbes and/or microbial products carried by the lymph may be similarly detected by sensory fibers in LNs. Consistent with this idea, we found that LN-innervating sensory neurons expressed mRNA for LPS receptors; i.e., *TLR4* and *TrpA1* as well as *Adam10*, the receptor for α-hemolysin, a PFT from *S. aureus* (Diogenes et al., 2011; Inoshima et al., 2011; Meseguer et al., 2014; Wilke and Bubeck Wardenburg, 2010). Finally, exposure of LN-innervating sensory fibers to the content of afferent lymph is also a potential vulnerability to incoming neurotropic pathogens. For example, subcutaneous challenge of mice with vesicular stomatitis virus (VSV) results in rapid transport of infectious lymph-borne virions to the draining LNs, where VSV can invade peripheral neurons to cause fatal ascending infection of the CNS (Iannacone et al., 2010). Although the anatomic origin and identity of VSV-susceptible nerve fibers in LNs remain to be formally established, their morphology and location in the subcapsular/capsular space are consistent with them being of sensory origin.

Identification of LEC 2 as top targets of LN-innervating sensory neurons is particularly intriguing because local sensory afferents have been implicated in regulation of antigen, lymph, and lymphocyte flow through LNs, processes that are controlled by LECs (Hanes et al., 2016; Moore et al., 1989). Whether and to what extent the communication between sensory neurons and LEC 2 contributes to those processes will require a better understanding of the distribution and function of LEC 2 within LNs. Using a recently published resource describing the transcriptional diversity and identity of LECs in human LNs (Takeda et al., 2019), we further contextualized our two murine LEC subsets. In the LEC 2 cluster, we found cells with elevated expression of *Emcn*, *Ackr2*, *Ackr4*, *Cav1*, and *Fabp4*, which suggests high similarity with LECs found in the SCS ceiling, afferent and efferent lymphatic vessels, as well as the cortical sinuses. Of note, two ceramidases, *Acer2* and *Asah2*, implicated in S1P biosynthesis, were downregulated by optogenetic stimulation in LEC 2, suggesting that sensory neurons may affect lymphocyte trafficking by regulating S1P-mediated lymphocyte egress from LNs (Mao and Obeid, 2008; Pappu et al., 2007; Pham et al., 2010). This could either reflect direct efferent communication between sensory neurons and LEC 2 or involve an efferent autonomic reflex triggered by afferent sensory signals. Consistent with the latter, sympathetic neurons have been previously shown to suppress lymphocyte egress from LNs (Nakai et al., 2014). Thus, sensory and sympathetic LN fibers may act together or independently to regulate the dwell time of recirculating lymphocytes within LNs, potentially fine-tuning antigen encounters and the ensuing adaptive immune response.

In the immune compartment, certain innate leukocytes, including neutrophils, macrophages, and mast cells, were also targets of optogenetically stimulated sensory fibers, whereas the bulk of adaptive lymphocytes remained essentially unaffected. Of note, a nociceptor-neutrophil communication axis has been identified recently as a major immunosuppressive mechanism in mouse models of *S. aureus*-induced pneumonia and *S. pyogenes*-induced necrotizing fasciitis (Baral et al., 2018; Pinho-Ribeiro et al., 2018). Whether nociceptor-neutrophil communication exerts similar immunomodulatory activities in LNs remains to be determined. Somewhat unexpectedly, interactions between sensory fibers and DCs in LNs were notably limited, at least within the experimental parameters of this study. This distinguishes LNs from peripheral barrier tissues, where nociceptors are necessary and sufficient to drive IL-23 production by dermal DCs, resulting in type 17 inflammation (Kashem et al., 2015; Riol-Blanco et al., 2014). However, it is important to note that neither *in silico* nor optogenetic analyses can rule out DCs or, for that matter, adaptive T or B cells as direct or indirect interacting partners of sensory neurons in LNs.

In conclusion, we established LNs as a point of convergence between the sensory nervous system and the immune system by identifying a molecularly distinct and heterogeneous population of sensory neurons with the capacity to affect LN function and homeostasis. We speculate that the heterogeneous, unique composition of LN-innervating sensory neurons may be an essential feature for continuous monitoring of the immune status of LNs, which may vary widely in magnitude and quality based on the type of challenge. Although further investigation will be needed, it is intriguing to hypothesize that specific immune triggers may also engage one or more subtype(s) of LN sensory neurons with distinct immunomodulatory capacities to customize immune activity, appropriately or maladaptively, for any given insult.

Limitations of study

The primary focus of this study was the identification and characterization of LN-innervating sensory neurons and their cellular communication partners at the anatomic and molecular levels. Although our analysis provides clues regarding how sensory neurons may monitor and modulate pathophysiological processes in LNs, it will be important to further establish their functional effect experimentally. For example, we show that LN-innervating neurons regulate, in LN LECs, the expression of enzymes involved in S1P metabolism, known to control lymphocyte egress. What, then, is the role of sensory innervation in lymphocyte homing to or egress from LNs at steady state and following inflammatory challenge? In theory, controlled optogenetic stimulation of LN-innervating fibers, as performed here, could address this question. However, to observe responses beyond short-term effects (e.g., changes in lymphocyte trafficking), longer time intervals of optogenetic stimulation would be required, and the unavoidable surgical preparation and prolonged exposure to highly energetic laser light would ultimately result in confounding local inflammation and tissue deterioration. Alternative, less invasive experimental strategies

to assay how LN-innervating neurons affect cellular dynamics need to be explored, and development of strategies to specifically ablate or inactivate LN-innervating sensory neurons will be critical to answer many outstanding questions. Finally, additional work will also be essential to understand the scope and context-dependent roles of LN-innervating neurons in response to a variety of pathogens and inflammatory challenges.

STAR★METHODS

Detailed methods are provided in the online version of this paper and include the following:

- KEY RESOURCES TABLE
- RESOURCE AVAILABILITY
  - Lead contact
  - Materials availability
  - Data and code availability
- EXPERIMENTAL MODEL AND SUBJECT DETAILS
- METHOD DETAILS
  - Whole mount immunohistochemistry
  - Retrograde labeling of LN- and skin-innervating neurons
  - Immunohistochemistry of tissue sections
  - Intravital two-photon microscopy
  - Subcutaneous challenge by footpad injection of LPS or Pam3CSK4
  - Manual cell sorting for scRNA-seq
  - scRNA-seq of neurons using Smart-Seq2
  - RNAscope
  - Tamoxifen treatment
  - 6-OHDA treatment
  - Optogenetic stimulation of iLN-innervating sensory neurons
  - LN Dissociation and Single Cell Isolation
  - LN scRNA-seq using Seq-Well
- QUANTIFICATION AND STATISTICAL ANALYSIS
  - Image analysis
  - Neuron scRNA-seq data preprocessing
  - Neuron scRNA-seq differential gene expression
  - Analysis of neuron scRNA-seq in the context of previously published datasets
  - LN Seq-Well data preprocessing
  - Dimensionality reduction, clustering, visualization, and cell type identification of LN Seq-Well data
  - Analysis of cellular receptor-ligand pairs
  - Differential gene expression following optogenetic stimulation
  - Statistical testing

Supplemental information

Supplemental Information can be found online at https://doi.org/10.1016/j.cell.2020.11.028.

ACKNOWLEDGMENTS

We thank Guiying Cheng for technical assistance with LN injections, Dr. Constance Cepko and Dr. Ralph Adams for sharing mouse lines, Dr. Stephen Liberles's lab for sharing the laser/shutter setup for optogenetic stimulation, Dr. David Ginty's lab for sharing the Zeiss microscope for whole-mount spinal cord and DRG imaging, the Microscopy Resources On the North Quad (MicRoN) facility for confocal microcopy, the HMS Center for Immune Imaging for provision of imaging and image analysis resources, and the members of the von Andrian and Shalek labs for comments and discussions of the project. We acknoweldge S. Knemeyer and V. Yeung (SciStories, LLC) for illustrations. S.H. was supported by the NIH (NIAMS 5R01AR068383-03 and 5T32HL066987-17) and a GSK postdoctoral fellowship. A.K.S. was supported by the Searle Scholars Program, the Beckman Young Investigator Program, the Pew-Stewart Scholars Program for Cancer Research, a Sloan Fellowship in Chemistry, the NIH (1DP2GM119419 and 2RM1HG006193), and the Ragon Institute of MGH, MIT and Harvard. J.O.M. was supported by HHMI Damon Runyon Cancer Research Foundation fellowship DRG-2274-16. C.G.K.Z. was supported by T32GM007753 from the NIH. U.H.v.A. was supported by the Ragon Institute of MGH, MIT and Harvard and NIH grant AR068383.

AUTHOR CONTRIBUTIONS

S.H., C.G.K.Z., A.K.S., and U.H.v.A. conceived the study. S.H. performed and analyzed *in vivo* experiments with help from J.A. and N.M. for image analysis. C.G.K.Z., with the help of J.O.-M. and M.V., generated scRNA-seq data. C.G.K.Z. analyzed scRNA-seq data. S.H., C.G.K.Z., A.K.S., and U.H.v.A. interpreted the results. S.H., C.G.K.Z., A.K.S., and U.H.v.A. wrote the manuscript with input from J.O.-M.

DECLARATION OF INTERESTS

A.K.S. has received compensation for consulting and SAB membership from Honeycomb Biotechnologies, Cellarity, Repertoire Immune Medicines, Ochre Bio, and Dahlia Biosciences. U.H.v.A. has received compensation for consulting and SAB membership from Beam, Cogen Therapeutics, Cygnal, Moderna, Monopteros, Morphic, Rubius, Selecta Biosciences, SQZ, and Synlogic. S.H., C.G.K.Z., A.K.S., and U.H.v.A. are co-inventors on a provisional patent application filed by the Broad Institute (U.S. patent no. 62/916,184) relating to the results described in this manuscript.

Received: November 11, 2019
Revised: September 23, 2020
Accepted: November 17, 2020
Published: December 16, 2020

REFERENCES

Abrahamsen, B., Zhao, J., Asante, C.O., Cendan, C.M., Marsh, S., Martinez-Barbera, J.P., Nassar, M.A., Dickenson, A.H., and Wood, J.N. (2008). The cell and molecular basis of mechanical, cold, and inflammatory pain. Science *321*, 702–705.

Adams, R.H., and Eichmann, A. (2010). Axon guidance molecules in vascular patterning. Cold Spring Harb. Perspect. Biol. *2*, a001875.

Aicher, T.P., Carroll, S., Raddi, G., Gierahn, T., Wadsworth, M.H., 2nd, Hughes, T.K., Love, C., and Shalek, A.K. (2019). Seq-Well: A Sample-Efficient, Portable Picowell Platform for Massively Parallel Single-Cell RNA Sequencing. Methods Mol. Biol. *1979*, 111–132.

Akira, S., Uematsu, S., and Takeuchi, O. (2006). Pathogen recognition and innate immunity. Cell *124*, 783–801.

Andoh, T., Nishikawa, Y., Yamaguchi-Miyamoto, T., Nojima, H., Narumiya, S., and Kuraishi, Y. (2007). Thromboxane A2 induces itch-associated responses through TP receptors in the skin in mice. J. Invest. Dermatol. *127*, 2042–2047.

Andrae, J., Gallini, R., and Betsholtz, C. (2008). Role of platelet-derived growth factors in physiology and medicine. Genes Dev. *22*, 1276–1312.

Assas, B.M., Pennock, J.I., and Miyan, J.A. (2014). Calcitonin gene-related peptide is a key neurotransmitter in the neuro-immune axis. Front. Neurosci. *8*, 23.

Baral, P., Umans, B.D., Li, L., Wallrapp, A., Bist, M., Kirschbaum, T., Wei, Y., Zhou, Y., Kuchroo, V.K., Burkett, P.R., et al. (2018). Nociceptor sensory neurons suppress neutrophil and γδ T cell responses in bacterial lung infections and lethal pneumonia. Nat. Med. *24*, 417–426.

Baral, P., Udit, S., and Chiu, I.M. (2019). Pain and immunity: implications for host defence. Nat. Rev. Immunol. *19*, 433–447.

Barkas, N., Petukhov, V., Nikolaeva, D., Lozinsky, Y., Demharter, S., Khodosevich, K., and Kharchenko, P.V. (2019). Joint analysis of heterogeneous single-cell RNA-seq dataset collections. Nat. Methods *16*, 695–698.

Bellinger, D.L., Lorton, D., Felten, S.Y., and Felten, D.L. (1992). Innervation of lymphoid organs and implications in development, aging, and autoimmunity. Int. J. Immunopharmacol. *14*, 329–344.

Belvisi, M.G. (2002). Overview of the innervation of the lung. Curr. Opin. Pharmacol. *2*, 211–215.

Blake, K.J., Baral, P., Voisin, T., Lubkin, A., Pinho-Ribeiro, F.A., Adams, K.L., Roberson, D.P., Ma, Y.C., Otto, M., Woolf, C.J., et al. (2018). Staphylococcus aureus produces pain through pore-forming toxins and neuronal TRPV1 that is silenced by QX-314. Nat. Commun. *9*, 37.

Bley, K.R., Hunter, J.C., Eglen, R.M., and Smith, J.A. (1998). The role of IP prostanoid receptors in inflammatory pain. Trends Pharmacol. Sci. *19*, 141–147.

Blondel, V.D., Guillaume, J., Lambiotte, R., and Lefebvre, E. (2008). Fast unfolding of communities in large networks. J. Stat. Mech. *2008*, P10008.

Brierley, S.M., Jones, R.C., 3rd, Gebhart, G.F., and Blackshaw, L.A. (2004). Splanchnic and pelvic mechanosensory afferents signal different qualities of colonic stimuli in mice. Gastroenterology *127*, 166–178.

Buettner, M., and Bode, U. (2012). Lymph node dissection–understanding the immunological function of lymph nodes. Clin. Exp. Immunol. *169*, 205–212.

Butler, A., Hoffman, P., Smibert, P., Papalexi, E., and Satija, R. (2018). Integrating single-cell transcriptomic data across different conditions, technologies, and species. Nat. Biotechnol. *36*, 411–420.

Chakrabarty, A., McCarson, K.E., and Smith, P.G. (2011). Hypersensitivity and hyperinnervation of the rat hind paw following carrageenan-induced inflammation. Neurosci. Lett. *495*, 67–71.

Chavan, S.S., Pavlov, V.A., and Tracey, K.J. (2017). Mechanisms and Therapeutic Relevance of Neuro-immune Communication. Immunity *46*, 927–942.

Chiu, I.M., von Hehn, C.A., and Woolf, C.J. (2012). Neurogenic inflammation and the peripheral nervous system in host defense and immunopathology. Nat. Neurosci. *15*, 1063–1067.

Chiu, I.M., Heesters, B.A., Ghasemlou, N., Von Hehn, C.A., Zhao, F., Tran, J., Wainger, B., Strominger, A., Muralidharan, S., Horswill, A.R., et al. (2013). Bacteria activate sensory neurons that modulate pain and inflammation. Nature *501*, 52–57.

Cho, C., Wang, Y., Smallwood, P.M., Williams, J., and Nathans, J. (2019). Dlg1 activates beta-catenin signaling to regulate retinal angiogenesis and the blood-retina and blood-brain barriers. eLife *8*, e45542.

Choi, I., Chung, H.K., Ramu, S., Lee, H.N., Kim, K.E., Lee, S., Yoo, J., Choi, D., Lee, Y.S., Aguilar, B., and Hong, Y.K. (2011). Visualization of lymphatic vessels by Prox1-promoter directed GFP reporter in a bacterial artificial chromosome-based transgenic mouse. Blood *117*, 362–365.

Chow, J.C., Young, D.W., Golenbock, D.T., Christ, W.J., and Gusovsky, F. (1999). Toll-like receptor-4 mediates lipopolysaccharide-induced signal transduction. J. Biol. Chem. *274*, 10689–10692.

Cohen, J.N., Tewalt, E.F., Rouhani, S.J., Buonomo, E.L., Bruce, A.N., Xu, X., Bekiranov, S., Fu, Y.X., and Engelhard, V.H. (2014). Tolerogenic properties of lymphatic endothelial cells are controlled by the lymph node microenvironment. PLoS ONE *9*, e87740.

Cohen, M., Giladi, A., Gorki, A.D., Solodkin, D.G., Zada, M., Hladik, A., Miklosi, A., Salame, T.M., Halpern, K.B., David, E., et al. (2018). Lung Single-Cell Signaling Interaction Map Reveals Basophil Role in Macrophage Imprinting. Cell *175*, 1031–1044.e18.

Cohen, J.A., Edwards, T.N., Liu, A.W., Hirai, T., Jones, M.R., Wu, J., Li, Y., Zhang, S., Ho, J., Davis, B.M., et al. (2019). Cutaneous TRPV1(+) Neurons Trigger Protective Innate Type 17 Anticipatory Immunity. Cell *178*, 919–932.e4.

Cordeiro, O.G., Chypre, M., Brouard, N., Rauber, S., Alloush, F., Romera-Hernandez, M., Bénézech, C., Li, Z., Eckly, A., Coles, M.C., et al. (2016). Integrin-Alpha IIb Identifies Murine Lymph Node Lymphatic Endothelial Cells Responsive to RANKL. PLoS ONE *11*, e0151848.

Deisseroth, K. (2011). Optogenetics. Nat. Methods *8*, 26–29.

Diogenes, A., Ferraz, C.C., Akopian, A.N., Henry, M.A., and Hargreaves, K.M. (2011). LPS sensitizes TRPV1 via activation of TLR4 in trigeminal sensory neurons. J. Dent. Res. *90*, 759–764.

Dobin, A., Davis, C.A., Schlesinger, F., Drenkow, J., Zaleski, C., Jha, S., Batut, P., Chaisson, M., and Gingeras, T.R. (2013). STAR: ultrafast universal RNA-seq aligner. Bioinformatics *29*, 15–21.

Drew, L.J., Wood, J.N., and Cesare, P. (2002). Distinct mechanosensitive properties of capsaicin-sensitive and -insensitive sensory neurons. J. Neurosci. *22*, RC228.

Drokhlyansky, E., Smillie, C.S., Wittenberghe, N.V., Ericsson, M., Griffin, G.K., Dionne, D., Cuoco, M.S., Goder-Reiser, M.N., Sharova, T., Aguirre, A.J., et al. (2019). The enteric nervous system of the human and mouse colon at single-cell resolution. Cell *182*, 1606–1622.e23.

Eelen, G., Dubois, C., Cantelmo, A.R., Goveia, J., Brüning, U., DeRan, M., Jarugumilli, G., van Rijssel, J., Saladino, G., Comitani, F., et al. (2018). Role of glutamine synthetase in angiogenesis beyond glutamine synthesis. Nature *561*, 63–69.

Ehling, M., Adams, S., Benedito, R., and Adams, R.H. (2013). Notch controls retinal blood vessel maturation and quiescence. Development *140*, 3051–3061.

Evrard, M., Kwok, I.W.H., Chong, S.Z., Teng, K.W.W., Becht, E., Chen, J., Sieow, J.L., Penny, H.L., Ching, G.C., Devi, S., et al. (2018). Developmental Analysis of Bone Marrow Neutrophils Reveals Populations Specialized in Expansion, Trafficking, and Effector Functions. Immunity *48*, 364–379.e8.

Fan, J., Salathia, N., Liu, R., Kaeser, G.E., Yung, Y.C., Herman, J.L., Kaper, F., Fan, J.B., Zhang, K., Chun, J., and Kharchenko, P.V. (2016). Characterizing transcriptional heterogeneity through pathway and gene set overdispersion analysis. Nat. Methods *13*, 241–244.

Felten, D.L., Felten, S.Y., Carlson, S.L., Olschowka, J.A., and Livnat, S. (1985). Noradrenergic and peptidergic innervation of lymphoid tissue. J. Immunol. *135* (2, Suppl), 755s–765s.

Felten, D.L., Felten, S.Y., Bellinger, D.L., and Lorton, D. (1992). Noradrenergic and peptidergic innervation of secondary lymphoid organs: role in experimental rheumatoid arthritis. Eur. J. Clin. Invest. *22* (*Suppl 1*), 37–41.

Fink, T., and Weihe, E. (1988). Multiple neuropeptides in nerves supplying mammalian lymph nodes: messenger candidates for sensory and autonomic neuroimmunomodulation? Neurosci. Lett. *90*, 39–44.

Fletcher, A.L., Malhotra, D., Acton, S.E., Lukacs-Kornek, V., Bellemare-Pelletier, A., Curry, M., Armant, M., and Turley, S.J. (2011). Reproducible isolation of lymph node stromal cells reveals site-dependent differences in fibroblastic reticular cells. Front. Immunol. *2*, 35.

Foster, S.L., Seehus, C.R., Woolf, C.J., and Talbot, S. (2017). Sense and Immunity: Context-Dependent Neuro-Immune Interplay. Front. Immunol. *8*, 1463.

Gautron, L., Sakata, I., Udit, S., Zigman, J.M., Wood, J.N., and Elmquist, J.K. (2011). Genetic tracing of Nav1.8-expressing vagal afferents in the mouse. J. Comp. Neurol. *519*, 3085–3101.

Gierahn, T.M., Wadsworth, M.H., 2nd, Hughes, T.K., Bryson, B.D., Butler, A., Satija, R., Fortune, S., Love, J.C., and Shalek, A.K. (2017). Seq-Well: portable, low-cost RNA sequencing of single cells at high throughput. Nat. Methods *14*, 395–398.

Godinho-Silva, C., Cardoso, F., and Veiga-Fernandes, H. (2019). Neuro-Immune Cell Units: A New Paradigm in Physiology. Annu. Rev. Immunol. *37*, 19–46.

González-Castillo, C., Ortuño-Sahagún, D., Guzmán-Brambila, C., Pallàs, M., and Rojas-Mayorquín, A.E. (2015). Pleiotrophin as a central nervous system

neuromodulator, evidences from the hippocampus. Front. Cell. Neurosci. *8*, 443.

Green, D.P., Limjunyawong, N., Gour, N., Pundir, P., and Dong, X. (2019). A Mast-Cell-Specific Receptor Mediates Neurogenic Inflammation and Pain. Neuron *101*, 412–420.e3.

Hanes, W.M., Olofsson, P.S., Talbot, S., Tsaava, T., Ochani, M., Imperato, G.H., Levine, Y.A., Roth, J., Pascal, M.A., Foster, S.L., et al. (2016). Neuronal circuits modulate antigen flow through lymph nodes. Bioelectron. Med. *3*, 18–28.

Hempel, C.M., Sugino, K., and Nelson, S.B. (2007). A manual method for the purification of fluorescently labeled neurons from the mammalian brain. Nat. Protoc. *2*, 2924–2929.

Heng, T.S., and Painter, M.W.; Immunological Genome Project Consortium (2008). The Immunological Genome Project: networks of gene expression in immune cells. Nat. Immunol. *9*, 1091–1094.

Homeister, J.W., Thall, A.D., Petryniak, B., Malý, P., Rogers, C.E., Smith, P.L., Kelly, R.J., Gersten, K.M., Askari, S.W., Cheng, G., et al. (2001). The alpha(1,3) fucosyltransferases FucT-IV and FucT-VII exert collaborative control over selectin-dependent leukocyte recruitment and lymphocyte homing. Immunity *15*, 115–126.

Hu, J., and Lewin, G.R. (2006). Mechanosensitive currents in the neurites of cultured mouse sensory neurones. J. Physiol. *577*, 815–828.

Huang, W., Sherman, B.T., and Lempicki, R.A. (2009a). Bioinformatics enrichment tools: paths toward the comprehensive functional analysis of large gene lists. Nucleic Acids Res. *37*, 1–13.

Huang, W., Sherman, B.T., and Lempicki, R.A. (2009b). Systematic and integrative analysis of large gene lists using DAVID bioinformatics resources. Nat. Protoc. *4*, 44–57.

Hughes, T.K., Wadsworth, M.H., Gierahn, T.M., Do, T., Weiss, D., Andrade, P.R., Ma, F., de Andrade Silva, B.J., Shao, S., Tsoi, L.C., et al. (2019). Highly Efficient, Massively-Parallel Single-Cell RNA-Seq Reveals Cellular States and Molecular Features of Human Skin Pathology. bioRxiv. https://doi.org/10.1101/689273.

Iannacone, M., Moseman, E.A., Tonti, E., Bosurgi, L., Junt, T., Henrickson, S.E., Whelan, S.P., Guidotti, L.G., and von Andrian, U.H. (2010). Subcapsular sinus macrophages prevent CNS invasion on peripheral infection with a neurotropic virus. Nature *465*, 1079–1083.

Iftakhar-E-Khuda, I., Fair-Mäkelä, R., Kukkonen-Macchi, A., Elima, K., Karikoski, M., Rantakari, P., Miyasaka, M., Salmi, M., and Jalkanen, S. (2016). Gene-expression profiling of different arms of lymphatic vasculature identifies candidates for manipulation of cell traffic. Proc. Natl. Acad. Sci. USA *113*, 10643–10648.

Inoshima, I., Inoshima, N., Wilke, G.A., Powers, M.E., Frank, K.M., Wang, Y., and Bubeck Wardenburg, J. (2011). A Staphylococcus aureus pore-forming toxin subverts the activity of ADAM10 to cause lethal infection in mice. Nat. Med. *17*, 1310–1314.

Janeway, C.A., Jr., and Medzhitov, R. (2002). Innate immune recognition. Annu. Rev. Immunol. *20*, 197–216.

Jin, M.S., Kim, S.E., Heo, J.Y., Lee, M.E., Kim, H.M., Paik, S.G., Lee, H., and Lee, J.O. (2007). Crystal structure of the TLR1-TLR2 heterodimer induced by binding of a tri-acylated lipopeptide. Cell *130*, 1071–1082.

Karrer, U., Althage, A., Odermatt, B., Roberts, C.W., Korsmeyer, S.J., Miyawaki, S., Hengartner, H., and Zinkernagel, R.M. (1997). On the key role of secondary lymphoid organs in antiviral immune responses studied in alymphoplastic (aly/aly) and spleenless (Hox11(-)/-) mutant mice. J. Exp. Med. *185*, 2157–2170.

Kashem, S.W., Riedl, M.S., Yao, C., Honda, C.N., Vulchanova, L., and Kaplan, D.H. (2015). Nociceptive Sensory Fibers Drive Interleukin-23 Production from CD301b+ Dermal Dendritic Cells and Drive Protective Cutaneous Immunity. Immunity *43*, 515–526.

Kawashima, H., Petryniak, B., Hiraoka, N., Mitoma, J., Huckaby, V., Nakayama, J., Uchimura, K., Kadomatsu, K., Muramatsu, T., Lowe, J.B., and Fukuda, M. (2005). N-acetylglucosamine-6-O-sulfotransferases 1 and 2 cooperatively control lymphocyte homing through L-selectin ligand biosynthesis in high endothelial venules. Nat. Immunol. *6*, 1096–1104.

Kharchenko, P.V., Silberstein, L., and Scadden, D.T. (2014). Bayesian approach to single-cell differential expression analysis. Nat. Methods *11*, 740–742.

Klein, R.S., Garber, C., and Howard, N. (2017). Infectious immunity in the central nervous system and brain function. Nat. Immunol. *18*, 132–141.

Kuehn, E.D., Meltzer, S., Abraira, V.E., Ho, C.Y., and Ginty, D.D. (2019). Tiling and somatotopic alignment of mammalian low-threshold mechanoreceptors. Proc. Natl. Acad. Sci. USA *116*, 9168–9177.

Kulkarni, R.M., Greenberg, J.M., and Akeson, A.L. (2009). NFATc1 regulates lymphatic endothelial development. Mech. Dev. *126*, 350–365.

Kupari, J., Haring, M., Agirre, E., Castelo-Branco, G., and Ernfors, P. (2019). An Atlas of Vagal Sensory Neurons and Their Molecular Specialization. Cell Rep. *27*, 2508–2523.e4.

Kurkowski, R., Kummer, W., and Heym, C. (1990). Substance P-immunoreactive nerve fibers in tracheobronchial lymph nodes of the guinea pig: origin, ultrastructure and coexistence with other peptides. Peptides *11*, 13–20.

Lakkis, F.G., Arakelov, A., Konieczny, B.T., and Inoue, Y. (2000). Immunologic 'ignorance' of vascularized organ transplants in the absence of secondary lymphoid tissue. Nat. Med. *6*, 686–688.

Larrivée, B., Freitas, C., Suchting, S., Brunet, I., and Eichmann, A. (2009). Guidance of vascular development: lessons from the nervous system. Circ. Res. *104*, 428–441.

Lawson, S.N., Crepps, B., and Perl, E.R. (2002). Calcitonin gene-related peptide immunoreactivity and afferent receptive properties of dorsal root ganglion neurones in guinea-pigs. J. Physiol. *540*, 989–1002.

Lewin, G.R., and Stucky, C.L. (2000). Sensory neuron mechanotransduction: regulation and underlying molecular mechanisms. Molecular basis of pain transduction (Wiley), pp. 129–148.

Li, L., Rutlin, M., Abraira, V.E., Cassidy, C., Kus, L., Gong, S., Jankowski, M.P., Luo, W., Heintz, N., Koerber, H.R., et al. (2011). The functional organization of cutaneous low-threshold mechanosensory neurons. Cell *147*, 1615–1627.

Lorton, D., Lubahn, C., Engan, C., Schaller, J., Felten, D.L., and Bellinger, D.L. (2000). Local application of capsaicin into the draining lymph nodes attenuates expression of adjuvant-induced arthritis. Neuroimmunomodulation *7*, 115–125.

Lutter, S., Xie, S., Tatin, F., and Makinen, T. (2012). Smooth muscle-endothelial cell communication activates Reelin signaling and regulates lymphatic vessel formation. J. Cell Biol. *197*, 837–849.

Mack, J.J., and Iruela-Arispe, M.L. (2018). NOTCH regulation of the endothelial cell phenotype. Curr. Opin. Hematol. *25*, 212–218.

Mackenzie, F., and Ruhrberg, C. (2012). Diverse roles for VEGF-A in the nervous system. Development *139*, 1371–1380.

Macosko, E.Z., Basu, A., Satija, R., Nemesh, J., Shekhar, K., Goldman, M., Tirosh, I., Bialas, A.R., Kamitaki, N., Martersteck, E.M., et al. (2015). Highly Parallel Genome-wide Expression Profiling of Individual Cells Using Nanoliter Droplets. Cell *161*, 1202–1214.

Mao, C., and Obeid, L.M. (2008). Ceramidases: regulators of cellular responses mediated by ceramide, sphingosine, and sphingosine-1-phosphate. Biochim. Biophys. Acta *1781*, 424–434.

Mason, M.R., Ehlert, E.M., Eggers, R., Pool, C.W., Hermening, S., Huseinovic, A., Timmermans, E., Blits, B., and Verhaagen, J. (2010). Comparison of AAV serotypes for gene delivery to dorsal root ganglion neurons. Mol. Ther. *18*, 715–724.

McCarter, G.C., Reichling, D.B., and Levine, J.D. (1999). Mechanical transduction by rat dorsal root ganglion neurons in vitro. Neurosci. Lett. *273*, 179–182.

McDavid, A., Finak, G., Chattopadyay, P.K., Dominguez, M., Lamoreaux, L., Ma, S.S., Roederer, M., and Gottardo, R. (2013). Data exploration, quality control and testing in single-cell qPCR-based gene expression experiments. Bioinformatics *29*, 461–467.

McLatchie, L.M., Fraser, N.J., Main, M.J., Wise, A., Brown, J., Thompson, N., Solari, R., Lee, M.G., and Foord, S.M. (1998). RAMPs regulate the transport and ligand specificity of the calcitonin-receptor-like receptor. Nature *393*, 333–339.

McMahon, S.B., La Russa, F., and Bennett, D.L. (2015). Crosstalk between the nociceptive and immune systems in host defence and disease. Nat. Rev. Neurosci. *16*, 389–402.

Mempel, T.R., Henrickson, S.E., and Von Andrian, U.H. (2004). T-cell priming by dendritic cells in lymph nodes occurs in three distinct phases. Nature *427*, 154–159.

Meseguer, V., Alpizar, Y.A., Luis, E., Tajada, S., Denlinger, B., Fajardo, O., Manenschijn, J.A., Fernández-Peña, C., Talavera, A., Kichko, T., et al. (2014). TRPA1 channels mediate acute neurogenic inflammation and pain produced by bacterial endotoxins. Nat. Commun. *5*, 3125.

Mithal, D.S., Banisadr, G., and Miller, R.J. (2012). CXCL12 signaling in the development of the nervous system. J. Neuroimmune Pharmacol. *7*, 820–834.

Moore, T.C., Lami, J.L., and Spruck, C.H. (1989). Substance P increases lymphocyte traffic and lymph flow through peripheral lymph nodes of sheep. Immunology *67*, 109–114.

Mooster, J.L., Le Bras, S., Massaad, M.J., Jabara, H., Yoon, J., Galand, C., Heesters, B.A., Burton, O.T., Mattoo, H., Manis, J., and Geha, R.S. (2015). Defective lymphoid organogenesis underlies the immune deficiency caused by a heterozygous S32I mutation in IκBα. J. Exp. Med. *212*, 185–202.

Nakai, A., Hayano, Y., Furuta, F., Noda, M., and Suzuki, K. (2014). Control of lymphocyte egress from lymph nodes through β2-adrenergic receptors. J. Exp. Med. *211*, 2583–2598.

Nassar, M.A., Stirling, L.C., Forlani, G., Baker, M.D., Matthews, E.A., Dickenson, A.H., and Wood, J.N. (2004). Nociceptor-specific gene deletion reveals a major role for Nav1.7 (PN1) in acute and inflammatory pain. Proc. Natl. Acad. Sci. USA *101*, 12706–12711.

Nonomura, K., Woo, S.H., Chang, R.B., Gillich, A., Qiu, Z., Francisco, A.G., Ranade, S.S., Liberles, S.D., and Patapoutian, A. (2017). Piezo2 senses airway stretch and mediates lung inflation-induced apnoea. Nature *541*, 176–181.

Norris, G.T., and Kipnis, J. (2019). Immune cells and CNS physiology: Microglia and beyond. J. Exp. Med. *216*, 60–70.

Oaklander, A.L., and Siegel, S.M. (2005). Cutaneous innervation: form and function. J. Am. Acad. Dermatol. *53*, 1027–1037.

Oh, S.W., Harris, J.A., Ng, L., Winslow, B., Cain, N., Mihalas, S., Wang, Q., Lau, C., Kuan, L., Henry, A.M., et al. (2014). A mesoscale connectome of the mouse brain. Nature *508*, 207–214.

Ordovas-Montanes, J., Rakoff-Nahoum, S., Huang, S., Riol-Blanco, L., Barreiro, O., and von Andrian, U.H. (2015). The Regulation of Immunological Processes by Peripheral Neurons in Homeostasis and Disease. Trends Immunol. *36*, 578–604.

Palazzo, E., Marconi, A., Truzzi, F., Dallaglio, K., Petrachi, T., Humbert, P., Schnebert, S., Perrier, E., Dumas, M., and Pincelli, C. (2012). Role of neurotrophins on dermal fibroblast survival and differentiation. J. Cell. Physiol. *227*, 1017–1025.

Pappu, R., Schwab, S.R., Cornelissen, I., Pereira, J.P., Regard, J.B., Xu, Y., Camerer, E., Zheng, Y.W., Huang, Y., Cyster, J.G., and Coughlin, S.R. (2007). Promotion of lymphocyte egress into blood and lymph by distinct sources of sphingosine-1-phosphate. Science *316*, 295–298.

Pham, T.H., Baluk, P., Xu, Y., Grigorova, I., Bankovich, A.J., Pappu, R., Coughlin, S.R., McDonald, D.M., Schwab, S.R., and Cyster, J.G. (2010). Lymphatic endothelial cell sphingosine kinase activity is required for lymphocyte egress and lymphatic patterning. J. Exp. Med. *207*, 17–27.

Picelli, S., Faridani, O.R., Björklund, A.K., Winberg, G., Sagasser, S., and Sandberg, R. (2014). Full-length RNA-seq from single cells using Smart-seq2. Nat. Protoc. *9*, 171–181.

Pinho-Ribeiro, F.A., Baddal, B., Haarsma, R., O'Seaghdha, M., Yang, N.J., Blake, K.J., Portley, M., Verri, W.A., Dale, J.B., Wessels, M.R., et al. (2018). Blocking Neuronal Signaling to Immune Cells Treats Streptococcal Invasive Infection. Cell *173*, 1083–1097.e22.

Pongratz, G., and Straub, R.H. (2013). Role of peripheral nerve fibres in acute and chronic inflammation in arthritis. Nat. Rev. Rheumatol. *9*, 117–126.

Popper, P., Mantyh, C.R., Vigna, S.R., Maggio, J.E., and Mantyh, P.W. (1988). The localization of sensory nerve fibers and receptor binding sites for sensory neuropeptides in canine mesenteric lymph nodes. Peptides *9*, 257–267.

Prinz, M., and Priller, J. (2017). The role of peripheral immune cells in the CNS in steady state and disease. Nat. Neurosci. *20*, 136–144.

Ramilowski, J.A., Goldberg, T., Harshbarger, J., Kloppmann, E., Lizio, M., Satagopam, V.P., Itoh, M., Kawaji, H., Carninci, P., Rost, B., and Forrest, A.R. (2015). A draft network of ligand-receptor-mediated multicellular signalling in human. Nat. Commun. *6*, 7866.

Ranade, S.S., Woo, S.H., Dubin, A.E., Moshourab, R.A., Wetzel, C., Petrus, M., Mathur, J., Bégay, V., Coste, B., Mainquist, J., et al. (2014). Piezo2 is the major transducer of mechanical forces for touch sensation in mice. Nature *516*, 121–125.

Reardon, C., Duncan, G.S., Brüstle, A., Brenner, D., Tusche, M.W., Olofsson, P.S., Rosas-Ballina, M., Tracey, K.J., and Mak, T.W. (2013). Lymphocyte-derived ACh regulates local innate but not adaptive immunity. Proc. Natl. Acad. Sci. USA *110*, 1410–1415.

Renier, N., Wu, Z., Simon, D.J., Yang, J., Ariel, P., and Tessier-Lavigne, M. (2014). iDISCO: a simple, rapid method to immunolabel large tissue samples for volume imaging. Cell *159*, 896–910.

Rice, F.L., and Albrecht, P.J. (2008). Cutaneous mechanisms of tactile perception: morphological and chemical organization of the innervation to the skin (Academic Press).

Riol-Blanco, L., Ordovas-Montanes, J., Perro, M., Naval, E., Thiriot, A., Alvarez, D., Paust, S., Wood, J.N., and von Andrian, U.H. (2014). Nociceptive sensory neurons drive interleukin-23-mediated psoriasiform skin inflammation. Nature *510*, 157–161.

Robertson, B. (1990). Wheat germ agglutinin binding in rat primary sensory neurons: a histochemical study. Histochemistry *94*, 81–85.

Rosas-Ballina, M., Olofsson, P.S., Ochani, M., Valdés-Ferrer, S.I., Levine, Y.A., Reardon, C., Tusche, M.W., Pavlov, V.A., Andersson, U., Chavan, S., et al. (2011). Acetylcholine-synthesizing T cells relay neural signals in a vagus nerve circuit. Science *334*, 98–101.

Sharma, N., Flaherty, K., Lezgiyeva, K., Wagner, D.E., Klein, A.M., and Ginty, D.D. (2020). The emergence of transcriptional identity in somatosensory neurons. Nature *577*, 392–398.

Shekhar, K., Lapan, S.W., Whitney, I.E., Tran, N.M., Macosko, E.Z., Kowalczyk, M., Adiconis, X., Levin, J.Z., Nemesh, J., Goldman, M., et al. (2016). Comprehensive Classification of Retinal Bipolar Neurons by Single-Cell Transcriptomics. Cell *166*, 1308–1323.e30.

Shepherd, A.J., Beresford, L.J., Bell, E.B., and Miyan, J.A. (2005a). Mobilisation of specific T cells from lymph nodes in contact sensitivity requires substance P. J. Neuroimmunol. *164*, 115–123.

Shibuya, M. (2011). Vascular Endothelial Growth Factor (VEGF) and Its Receptor (VEGFR) Signaling in Angiogenesis: A Crucial Target for Anti- and Pro-Angiogenic Therapies. Genes Cancer *2*, 1097–1105.

Smillie, C.S., Biton, M., Ordovas-Montanes, J., Sullivan, K.M., Burgin, G., Graham, D.B., Herbst, R.H., Rogel, N., Slyper, M., Waldman, J., et al. (2019). Intra- and Inter-cellular Rewiring of the Human Colon during Ulcerative Colitis. Cell *178*, 714–730.e22.

Stein, J.V., Rot, A., Luo, Y., Narasimhaswamy, M., Nakano, H., Gunn, M.D., Matsuzawa, A., Quackenbush, E.J., Dorf, M.E., and von Andrian, U.H. (2000). The CC chemokine thymus-derived chemotactic agent 4 (TCA-4, secondary lymphoid tissue chemokine, 6Ckine, exodus-2) triggers lymphocyte function-associated antigen 1-mediated arrest of rolling T lymphocytes in peripheral lymph node high endothelial venules. J. Exp. Med. *191*, 61–76.

Stuart, T., Butler, A., Hoffman, P., Hafemeister, C., Papalexi, E., Mauck, W.M., 3rd, Hao, Y., Stoeckius, M., Smibert, P., and Satija, R. (2019). Comprehensive Integration of Single-Cell Data. Cell *177*, 1888–1902.e21.

Südhof, T.C. (2018). Towards an Understanding of Synapse Formation. Neuron *100*, 276–293.

Suvas, S. (2017). Role of Substance P Neuropeptide in Inflammation, Wound Healing, and Tissue Homeostasis. J. Immunol. *199*, 1543–1552.

Takahashi, Y., and Nakajima, Y. (1996). Dermatomes in the rat limbs as determined by antidromic stimulation of sensory C-fibers in spinal nerves. Pain *67*, 197–202.

Takeda, A., Hollmen, M., Dermadi, D., Pan, J., Brulois, K.F., Kaukonen, R., Lonnberg, T., Bostrom, P., Koskivuo, I., Irjala, H., et al. (2019). Single-Cell Survey of Human Lymphatics Unveils Marked Endothelial Cell Heterogeneity and Mechanisms of Homing for Neutrophils. Immunity *51*, 561–572.e5.

Tallini, Y.N., Shui, B., Greene, K.S., Deng, K.Y., Doran, R., Fisher, P.J., Zipfel, W., and Kotlikoff, M.I. (2006). BAC transgenic mice express enhanced green fluorescent protein in central and peripheral cholinergic neurons. Physiol. Genomics *27*, 391–397.

Trombetta, J.J., Gennert, D., Lu, D., Satija, R., Shalek, A.K., and Regev, A. (2014). Preparation of Single-Cell RNA-Seq Libraries for Next Generation Sequencing. Curr. Protoc. Mol. Biol. *107*, 4.22.21-17.

Uchimura, K., Gauguet, J.M., Singer, M.S., Tsay, D., Kannagi, R., Muramatsu, T., von Andrian, U.H., and Rosen, S.D. (2005). A major class of L-selectin ligands is eliminated in mice deficient in two sulfotransferases expressed in high endothelial venules. Nat. Immunol. *6*, 1105–1113.

Ulvmar, M.H., Werth, K., Braun, A., Kelay, P., Hub, E., Eller, K., Chan, L., Lucas, B., Novitzky-Basso, I., Nakamura, K., et al. (2014). The atypical chemokine receptor CCRL1 shapes functional CCL21 gradients in lymph nodes. Nat. Immunol. *15*, 623–630.

Usoskin, D., Furlan, A., Islam, S., Abdo, H., Lönnerberg, P., Lou, D., Hjerling-Leffler, J., Haeggström, J., Kharchenko, O., Kharchenko, P.V., et al. (2015). Unbiased classification of sensory neuron types by large-scale single-cell RNA sequencing. Nat. Neurosci. *18*, 145–153.

Vaahtomeri, K., Karaman, S., Mäkinen, T., and Alitalo, K. (2017). Lymphangiogenesis guidance by paracrine and pericellular factors. Genes Dev. *31*, 1615–1634.

Vanlandewijck, M., He, L., Mäe, M.A., Andrae, J., Ando, K., Del Gaudio, F., Nahar, K., Lebouvier, T., Laviña, B., Gouveia, L., et al. (2018). A molecular atlas of cell types and zonation in the brain vasculature. Nature *554*, 475–480.

Veiga-Fernandes, H., and Mucida, D. (2016). Neuro-Immune Interactions at Barrier Surfaces. Cell *165*, 801–811.

Vento-Tormo, R., Efremova, M., Botting, R.A., Turco, M.Y., Vento-Tormo, M., Meyer, K.B., Park, J.E., Stephenson, E., Polański, K., Goncalves, A., et al. (2018). Single-cell reconstruction of the early maternal-fetal interface in humans. Nature *563*, 347–353.

von Andrian, U.H. (1996). Intravital microscopy of the peripheral lymph node microcirculation in mice. Microcirculation *3*, 287–300.

von Andrian, U.H., and Mempel, T.R. (2003). Homing and cellular traffic in lymph nodes. Nat. Rev. Immunol. *3*, 867–878.

Wacker, M.J., Tehrani, R.N., Smoot, R.L., and Orr, J.A. (2002). Thromboxane A(2) mimetic evokes a bradycardia mediated by stimulation of cardiac vagal afferent nerves. Am. J. Physiol. Heart Circ. Physiol. *282*, H482–H490.

Waltman, L., and Van Eck, N.J. (2013). A smart local moving algorithm for large-scale modularity-based community detection. Eur. Phys. J. B *86*, 471.

Wilke, G.A., and Bubeck Wardenburg, J. (2010). Role of a disintegrin and metalloprotease 10 in Staphylococcus aureus alpha-hemolysin-mediated cellular injury. Proc. Natl. Acad. Sci. USA *107*, 13473–13478.

Winkler, C., and Yao, S. (2014). The midkine family of growth factors: diverse roles in nervous system formation and maintenance. Br. J. Pharmacol. *171*, 905–912.

Woo, S.H., Lukacs, V., de Nooij, J.C., Zaytseva, D., Criddle, C.R., Francisco, A., Jessell, T.M., Wilkinson, K.A., and Patapoutian, A. (2015). Piezo2 is the principal mechanotransduction channel for proprioception. Nat. Neurosci. *18*, 1756–1762.

Wood, J.N., Emery, E.C., and Ernfors, P. (2018). Dorsal Root Ganglion Neuron Types and Their Functional Specialization (Oxford University Press).

Wu, H., Xiong, W.C., and Mei, L. (2010). To build a synapse: signaling pathways in neuromuscular junction assembly. Development *137*, 1017–1033.

Wu, M., Du, Y., Liu, Y., He, Y., Yang, C., Wang, W., and Gao, F. (2014). Low molecular weight hyaluronan induces lymphangiogenesis through LYVE-1-mediated signaling pathways. PLoS ONE *9*, e92857.

Yamano, T., Dobeš, J., Vobořil, M., Steinert, M., Brabec, T., Ziętara, N., Dobešová, M., Ohnmacht, C., Laan, M., Peterson, P., et al. (2019). Aire-expressing ILC3-like cells in the lymph node display potent APC features. J. Exp. Med. *216*, 1027–1037.

Yang, X.M., Han, H.X., Sui, F., Dai, Y.M., Chen, M., and Geng, J.G. (2010). Slit-Robo signaling mediates lymphangiogenesis and promotes tumor lymphatic metastasis. Biochem. Biophys. Res. Commun. *396*, 571–577.

Ye, X., Wang, Y., and Nathans, J. (2010). The Norrin/Frizzled4 signaling pathway in retinal vascular development and disease. Trends Mol. Med. *16*, 417–425.

Zeng, W.Z., Marshall, K.L., Min, S., Daou, I., Chapleau, M.W., Abboud, F.M., Liberles, S.D., and Patapoutian, A. (2018). PIEZOs mediate neuronal sensing of blood pressure and the baroreceptor reflex. Science *362*, 464–467.

Zhang, G., Brady, J., Liang, W.C., Wu, Y., Henkemeyer, M., and Yan, M. (2015). EphB4 forward signalling regulates lymphatic valve development. Nat. Commun. *6*, 6625.

Zhou, P., Hwang, K.W., Palucki, D., Kim, O., Newell, K.A., Fu, Y.X., and Alegre, M.L. (2003). Secondary lymphoid organs are important but not absolutely required for allograft responses. Am. J. Transplant. *3*, 259–266.

Please cite this article in press as: Huang et al., Lymph nodes are innervated by a unique population of sensory neurons with immunomodulatory potential, Cell (2021), https://doi.org/10.1016/j.cell.2020.11.028

STAR★METHODS

KEY RESOURCES TABLE

REAGENT or RESOURCE	SOURCE	IDENTIFIER
Antibodies		
Goat anti mCherry	ACRIS	Cat# AB0040-200; RRID:AB_2333092, 1:500
Rabbit anti-CGRP	Immunostar	Cat# 24112; RRID:AB_10000240, 1:500
Chicken anti-GFP	Aves Labs	Cat# GFP-1020; RRID:AB_10000240, 1:500
Chicken anti-NF200	Aves Labs	Cat# NFH; RRID:AB_2313552, 1:500
Rabbit anti-Tyrosine Hydroxylase	Millipore	Cat# AB152; RRID:AB_390204, 1:500
Rabbit anti-βIII-Tubulin	Biolegend	Cat# 802001; RRID:AB_2564645, 1:500
Alexa Fluor 647-conjugated rat anti-CD31	Biolegend	Cat# 102416; RRID:AB_493410, 1:50
FITC–conjugated mouse anti-smooth muscle actin (aSMA)	Sigma	Cat# F3777-.2ML; RRID:AB_476977, 1:500
eFluor 660-conjugated mouse anti-smooth muscle actin (aSMA)	Thermo Fisher	Cat# 50-9760-82; RRID:AB_2574362, 1:100
eFluor 660-conjugated rat anti-CD169	Thermo Fisher	Cat# 50-5755-80; RRID:AB_2574240, 1:100
Pacific Blue-conjugated rat anti-CD45	Biolegend	Cat# 103126; RRID:AB_493535, 1:50
Alexa Fluor 488-conjugated rat anti-PNAd	Thermo Fisher	Cat# 53-6036-82; RRID:AB_10804391, 1:50
FITC-conjugated rat anti-CD169	BioRad	Cat# MCA947F; RRID:AB_322323
Bacterial and virus strains		
AAV2/1.CMV.HI.eGFP-Cre.WPRE.SV40	Gift from Wilson J. M.	Addgene, Cat# 105545-AAV1, titer ≥ 8E+12 vg/ml
AAV2/1.CAG.Flex.tdTomato.WPRE.bGH	Oh et al. (2014)	Addgene, Cat# 51503-AAV1, titer ≥ 1E+13 vg/ml
Chemicals, peptides, and recombinant proteins		
2-Mercaptoethanol	Sigma	Cat# M3148-25ML
RLT Buffer	QIAGEN	Cat# 79216
dNTP	New England BioLabs	Cat# N0447L
RNase Inhibitor	Fisher Scientific	Cat# AM2696
Maxima RNaseH-minus RT Enzyme	Fisher Scientific	Cat# EP0753
$MgCl_2$	Sigma	Cat# 63069-100ML
Betaine	Sigma	Cat# B0300-5VL
AMPure RNAClean XP RNA-SPRI beads	Beckman Coulter	Cat# A63987
AMPure XP SPRI beads	Beckman Coulter	Cat# A63881
Guanidinium thiocyanate	Sigma	Cat# AM9422
Sarkosyl	Sigma	Cat# L7414
Exonuclease I	New England BioLabs	Cat# M0293S
(3-Aminopropyl)triethoxysilane (APTES)	Sigma	Cat# A3648-100ML
p-Phenylene diisothiocyanate (PDITC)	Sigma	Cat# 258555-5G
Pyridine	Sigma	Cat# 270970-1L
N,N-Dimethylformamide (DMF)	Sigma	Cat# 227056-2L
Chitosan	Sigma	Cat# C3646-100G
Poly(L-glutamic) acid sodium solution	Sigma	Cat# P4761-100MG
Klenow Fragment	New England BioLabs	Cat #M0212L
DNase I	Roche	Cat# 10104159001
Dispase	Thermo Fisher Scientific	Cat# 17105041
Collagenase P	Roche	Cat# 11213857001
WGA-AF488	Invitrogen	Cat# W11261, 2 mg/ml in PBS

(*Continued on next page*)

Continued

REAGENT or RESOURCE	SOURCE	IDENTIFIER
Papain	Worthington	Cat# LS003126
Collagenase type II	Worthington	Cat# LS004176
GenTeal Tears Lubricant Eye Gel	Alcon	Cat# NDC 0078-0429-47
Pam3CSK4	Invivogen	Cat# tlrl-pms
LPS	Sigma	Cat# L2654-1MG
Critical commercial assays		
Nextera XT DNA Library Preparation Kit	Illumina	Cat# FC-131-1096
CD3e MicroBead Kit	Miltenyi Biotec	Cat# 130-094-973
CD19 MicroBead Kit	Miltenyi Biotec	Cat# 130-121-301
LD columns	Miltenyi Biotec	Cat# 130-042-901
High Sensitivity D5000 ScreenTape	Agilent	Cat# 5067-5592
Qubit dsDNA High-Sensitivity kit	ThermoFisher	Cat# Q32854
NextSeq 500/550 High Output v2 (75 cycles)	Illumina	Cat# FC-404-2005
Kapa HiFi HotStart ReadyMix	Kapa Biosystems	Cat# KK2602
MACOSKO-2011-10 mRNA Capture Beads	ChemGenes	Cat# NC0927472
RNAscope® Multiplex Fluorescent Reagent Kit v2	ACD Biosystems	Cat# 323100
Deposited data		
Raw data, SMART-Seq2 of LN-innervating or skin-innervating neurons	Gene Expression Omnibus (https://www.ncbi.nlm.nih.gov/geo/)	GSE139600
Raw data, Seq-Well of LN-resident cells	Gene Expression Omnibus (https://www.ncbi.nlm.nih.gov/geo/)	GSE139658
Processed data, SMART-Seq2 of LN-innervating or skin-innervating neurons	Single Cell Portal	https://singlecell.broadinstitute.org/single_cell/study/SCP1187
Processed data, Seq-Well of LN-resident cells	Single Cell Portal	https://singlecell.broadinstitute.org/single_cell/study/SCP1186
Experimental models: organisms/strains		
Mouse: *Nav1.8^{Cre}*	Nassar et al., 2004	RRID:IMSR_EM:04582
Mouse: *Rosa26$^{LSL\text{-}tdTomato}$*: B6.Cg-*Gt(ROSA)26Sor$^{tm14(CAG\text{-}tdTomato)Hze}$*/J	The Jackson Laboratory	RRID:IMSR_JAX:007914
Mouse: *Bmx-CreER^{T2}*	Ehling et al., 2013	MGI:5513853
Mouse: *Rosa26$^{LSL\text{-}DTA}$*: B6.129P2-*Gt(ROSA)26Sor$^{tm1(DTA)Lky}$*/J	The Jackson Laboratory	RRID:IMSR_JAX:009669
Mouse: *Prox1-EGFP*	Choi et al., 2011	MGI:4847348
Mouse: *Rosa26$^{LSL\text{-}ChR2\text{-}eYFP}$*: B6.Cg-*Gt(ROSA)26Sor$^{tm32(CAG\text{-}COP4*H134R/EYFP)Hze}$*/J	The Jackson Laboratory	RRID:IMSR_JAX:024109
Mouse: *Rosa26$^{LSL\text{-}eYFP}$*: B6.Cg-Gt(ROSA)26Sortm3 (CAG-EYFP)Hze/J	The Jackson Laboratory	RRID:IMSR_JAX:007903
Mouse: *B6.Cg-Tg(RP23-268L19-EGFP)2Mik/J*	The Jackson Laboratory	RRID:IMSR_JAX:007902
Oligonucleotides		
SMART-seq2 2 3′ Oligo-dT Primer: /5Biosg/AAG CAG TGG TAT CAA CGC AGA GTA CTT TTT TTT TTT TTT TTT TTT TTT TTT TTT TVN	Integrated DNA Technologies	N/A
SMART-seq2 5′ TSO: AAG CAG TGG TAT CAA CGC AGA GTA CAT rGrGrG	Integrated DNA Technologies	N/A
SMART-seq2 and Seq-Well ISPCR: AAG CAG TGG TAT CAA CGC AGA GT	Integrated DNA Technologies	N/A
Custom Read 1 Primer: GCC TGT CCG CGG AAG CAG TGG TAT CAA CGC AGA GTA C	Integrated DNA Technologies	N/A

(*Continued on next page*)

Please cite this article in press as: Huang et al., Lymph nodes are innervated by a unique population of sensory neurons with immunomodulatory potential, Cell (2021), https://doi.org/10.1016/j.cell.2020.11.028

Continued

REAGENT or RESOURCE	SOURCE	IDENTIFIER
Seq-Well 5′ TSO: AAG CAG TGG TAT CAA CGC AGA GTG AAT rGrGrG	Integrated DNA Technologies	N/A
Seq-Well Custom P5-SMART PCR hybrid oligo: AAT GAT ACG GCG ACC ACC GAG ATC TAC ACG CCT GTC CGC GGA AGC AGT GGT ATC AAC GCA GAG TAC	Integrated DNA Technologies	N/A
Seq-Well dN-SMRT oligo: AAG CAG TGG TAT CAA CGC AGA GTG ANN NGG NNN B	Integrated DNA Technologies	N/A
RNAscope® Probe -tdTomato-C2	ACD Biosystems	Cat# 317041-C2
RNAscope® Probe -Mm-Ptgir	ACD Biosystems	Cat# 487851
RNAscope® Probe -Mm-Prokr2-C3	ACD Biosystems	Cat# 98431-C3
Software and algorithms		
R version 3.4.4	R Core Team	https://www.r-project.org
R package – Seurat v2.3.4	Github	https://github.com/satijalab/seurat
R package – SCDE	Bioconductor	http://bioconductor.org/packages/release/bioc/html/scde.html
R package – mixOmics	Bioconductor	http://bioconductor.org/packages/release/bioc/html/mixOmics.html
Prism 6	GraphPad Software	https://www.graphpad.com/scientific-software/prism/
STAR	Github	https://github.com/alexdobin/STAR
Imaris 9.2.1 and 7.4.2	Imaris	9.2.1 and 7.4.2
Other		
Capillary Tubing for Microinjection	FHC	Cat# 27-30-0
Aspirator Tube Assemblies for Calibrated Microcapillary Pipettes	Sigma	Cat# A5177-5EA
Capillary Tubing for Single Cell Picking	World Precision Instruments	Cat# TW100F-4
Optical Fiber	Thorlabs	Cat# CFMLC12U-20

RESOURCE AVAILABILITY

Lead contact

Further information and requests for resources and reagents should be directed to and will be fulfilled by the Lead Contact, Ulrich H. von Andrian (uva@hms.harvard.edu).

Materials availability

No new or unique reagents were generated in this study.

Data and code availability

The raw data and gene expression matrices for all scRNA-seq data have been deposited in the Gene Expression Omnibus (https://www.ncbi.nlm.nih.gov/geo/) under the accession number GSE139600 for SMART-seq2 of LN-innervating or skin-innervating neurons, and accession number GSE139658 for Seq-Well of LN-resident cells. Raw data and metadata can also be downloaded and visualized on the Single Cell Portal: LN-resident cells, https://singlecell.broadinstitute.org/single_cell/study/SCP1186. LN-innervating and skin-innervating neurons, https://singlecell.broadinstitute.org/single_cell/study/SCP1187. Gene lists corresponding to differential expression tests in Figures 4E, 5A, 5B, and S4F–S4H can be found in Table S1. Cell type-identifying gene lists corresponding to Figures 6B, 6C, and S5A–S5P can be found in Table S2. All differentially expressed genes from optogenetic stimulation experiments presented in Figures 7C–7H can be found in Table S3. All R code for analysis available upon request.

EXPERIMENTAL MODEL AND SUBJECT DETAILS

Mouse lines used in this study were all previously described and include *Nav1.8*^{Cre} (RRID:IMSR_EM:04582) (Nassar et al., 2004), *Rosa26*$^{LSL\text{-}tdTomato}$ (RRID:IMSR_JAX:007914), *Bmx-CreER*^{T2} (MGI:5513853) (Ehling et al., 2013), *Rosa26*$^{LSL\text{-}DTA}$ (RRID:IMSR_JAX:009669), *Prox1-EGFP* (MGI:4847348) (Choi et al., 2011), *Rosa26*$^{LSL\text{-}ChR2\text{-}eYFP}$ (RRID:IMSR_JAX:024109), *Rosa26*$^{LSL\text{-}eYFP}$

(RRID:IMSR_JAX:007903) and *ChAT*^{BAC}*-eGFP* (RRID:IMSR_JAX: 007902). All of the animals were handled according to approved institutional animal care and use committee (IACUC) protocols of Harvard Medical School. Unless indicated otherwise, adult mice of both sexes between 6-12 weeks of age were used for various experiments.

METHOD DETAILS

Whole mount immunohistochemistry

Whole mount immunohistochemistry of LNs was performed using an iDISCO protocol with methanol pretreatment optimized for LNs (Renier et al., 2014). Briefly, adult animals (6-12 weeks) were perfused with 25 mL of PBS (Hyclone) and 25 mL of 4% paraformaldehyde (PFA, Sigma) sequentially at room temperature (RT). Peripheral lymph nodes (PLNs), including popliteal and inguinal lymph nodes (popLNs and iLNs), were postfixed with 4% PFA for 1 hr at 4°C. For methanol pretreatment, fixed LNs were washed sequentially in 50% methanol (Fisher Scientific) (in PBS) for 1 hr, 100% methanol for 1 hr, 50% methanol for 1 hr, PBS for 1 hr twice, and PBS/0.2% Triton X-100 (VWR) for 1 hr twice at RT. LNs were then left in PBS/0.2% Triton X-100/20% DMSO (Sigma)/0.3 M glycine (BioRad) overnight at RT and blocked in PBS/0.2% Triton X-100/10% DMSO/6% donkey serum (Jackson Immunoresearch) or goat serum (GIBCO)/anti-CD16/CD32 (Fc block) (Bio X cell) overnight at RT. LNs were subsequently washed in PBS/0.2% Tween-20 (Fisher Scientific)/10 μg/mL heparin (Sigma) (PTwH), for 1 hr twice at RT, before incubation with antibody mix in PTwH/5% DMSO/3% donkey or goat serum/Fc block 1:100 for 3 days at RT. LNs were extensively washed in PTwH for at least 6 times over the course of a day at RT. For unconjugated antibodies, LNs were further incubated with a secondary antibody mix including a panel of species-specific anti-IgG (H+L) Alexa Fluro 488, 546, 647 and 594-conjugated antibodies (Invitrogen or Jackson Immunoresearch) in PTwH/5% DMSO/3% donkey or goat serum/Fc block 1:100 for 3 more days at RT. LNs were washed in the same way as after primary antibody incubation for 1 day. Immunolabeled LNs following one round of antibody incubation for conjugated antibodies (or two for unconjugated antibodies) were then processed for clearing, which includes sequential incubation with 50% methanol for 1 hr, 100% methanol for 1 hr for three times and a mixture of 1-part benzyl alcohol (Sigma): 2-parts benzyl benzoate (Sigma) (BABB) overnight at RT. For tdTomato immunolabeling, goat anti-mCherry antibody (ACRIS) was preabsorbed against PLNs from *tdTomato*$^{-}$ animals overnight at RT prior to use.

Whole mount immunohistochemistry of DRGs and the skin was performed as described previously (Li et al., 2011). Briefly, DRGs inside vertebral column and the depilated hairy skin from PFA-perfused animals (6-12 weeks) were postfixed with 4% PFA for 1 hr or Zamboni fixative (Fisher Scientific) overnight, respectively at 4°C. Samples were washed every 30 min with PBS/0.3% Triton-100 (0.3% PBST) for 4-6 hr, then incubated with primary antibodies in antibody diluent (0.3% PBST/20% DMSO/5% donkey or goat serum) for 2-3 days at RT. Samples were then washed with 0.3% PBST every 30 min for 5–8 hr before incubation with secondary antibodies in antibody diluent for 2-3 days at RT. After extensive washes as described above, samples were dehydrated and cleared in 50% methanol for 1 hr, 100% methanol for 1 hr for three times and BABB overnight at RT.

Cleared whole-mount tissues were imaged in BABB between two coverglasses using Olympus FV3000 confocal imaging system, except for those shown in Figures 7K and 7L, which were acquired on BioRad 2100MP system and those shown in Figures 3B, S3B, and S3E, which were acquired on Zeiss Stereo Discovery V16. The antibodies used were: rabbit anti-CGRP (Immunostar, 24112, 1:500), chicken anti-GFP (Aves Labs, GFP-1020, 1:500), chicken anti-NF200 (Aves Labs, NFH, 1:500), rabbit anti-Tyrosine Hydroxylase (Millipore, AB152, 1:500), goat anti mCherry antibody (1:500, ACRIS AB0040-200), rabbit anti-βIII-Tubulin (Biolegend, 802001, 1:500), Alexa Fluor 647-conjugated rat anti-CD31 (Biolegend, 102416, 1:50), FITC–conjugated mouse anti-smooth muscle actin (aSMA) (Sigma, F3777-.2ML, 1:500), eFluor 660-conjugated mouse anti-smooth muscle actin (aSMA) (Thermo Fisher, 50-9760-82, 1:100), eFluor 660-conjugated rat anti-CD169 (Thermo Fisher, 50-5755-80, 1:50), Pacific Blue-conjugated rat anti-CD45 (Biolegend, 103126, 1:50), Alexa Fluor 488-conjugated rat anti-PNAd (Thermo Fisher, 53-6036-82, 1:50)

Retrograde labeling of LN- and skin-innervating neurons

To retrogradely label LN-innervating neurons, adult animals (6-12 weeks) were anesthetized by intraperitoneal injection of ketamine (Patterson Vet) (50 mg kg^{-1}) and xylazine (Patterson Vet) (10 mg kg^{-1}). The skin overlying the targeted iLN was shaved and depilated so that the LN underneath was visible percutaneously. A 5 mm incision was made directly on top of the iLN. The iLN was microdissected without perturbing afferent lymphatic vessels and surrounding blood vessels. 1 μL of Adeno-Associated Virus (AAV) (AAV2/1.CMV.HI.eGFP-Cre.WPRE.SV40, titer > = 8E+12 vg/mL, Addgene) mixed with 0.5 μL of fast green (Sigma) was injected into the iLN of *Rosa26*$^{LSL\text{-}tdTomato/LSL\text{-}tdTomato}$ animals using a pulled and trimmed glass pipette (FHC) which was connected to a 5 mL syringe through the aspiration assembly system (Sigma). The injection site was immediately rinsed with 2 mL of saline (Patterson Vet) to wash away any off-target virus before the incision was closed with sutures. Animals were sacrificed between 1 month and 6 months after injection for histology or scRNA-seq. To directly visualize the axonal projections of sensory neurons retrogradely labeled from the iLN, AAV carrying Cre-dependent tdTomato cassette (AAV2/1.CAG.Flex.tdTomato.WPRE.bGH, titer $\geq 10^{13}$ vg/mL, Addgene) was injected into the iLN *Nav1.8*$^{Cre/+}$ animals as described above. For WGA-based retrograde labeling, 1 μL of WGA-AF488 (2 mg/mL in PBS, Invitrogen) was injected into the iLN of *Nav1.8*$^{Cre/+}$; *Rosa26*$^{LSL\text{-}tdTomato/+}$ animals as described before and the animals were processed for histology 4 days post injection. Retrograde labeling of skin-innervating neurons was described previously (Kuehn et al., 2019). Briefly, following ketamine-xylazine mediated anesthesia, a single injection of 0.2 μL of various AAV2/1 viruses as described above and 0.1 μL of fast green was delivered using the injection device described above intradermally into the patch of depilated skin

overlying the iLN of adult mice (6-12 weeks). Animals were sacrificed between 1 month and 6 months after injection for immunohistochemistry, RNAscope, or scRNA-seq.

Immunohistochemistry of tissue sections

Adult animals (6-12 weeks) were perfused with 25 mL of PBS and 25 mL of 4% PFA sequentially at RT. The intact vertebral column was postfixed overnight with 4% PFA at 4°C. DRGs were subsequently dissected and processed for cryosectioning. 14 μm serial cryosections were collected and processed for immunohistochemistry as described previously (Li et al., 2011). In brief, sections were postfixed with 4% PFA for 10 min at RT. Following three washes with PBS, they were incubated with blocking buffer (PBS with 5% normal goat serum and 0.3% Triton-100) for 1 hr at RT. The sections were then incubated with Rabbit anti-TH (Millipore) in the same blocking buffer overnight at 4°C. The following day, sections were washed three times with wash buffer (PBS with 0.3% Triton-100) before incubation with goat Alexa Fluor 647-conjugated anti-rabbit (Invitrogen) for 1 hr at RT. Sections were then washed for three times with wash buffer before mounting in Fluoromount Aqueous Mounting Medium (Sigma). WGA-488 and tdTomato were visualized directly based on endogenous fluorescence. All the sections with tdTomato$^+$ cells were imaged at 20x using Olympus FV3000 confocal imaging system.

Intravital two-photon microscopy

Adult *Nav1.8*$^{Cre/+}$; *Rosa26*$^{LSL\text{-}tdTomato/+}$ animals (6-12 weeks) were given 1 μg of FITC-conjugated rat anti-CD169 antibody (BioRad) diluted in a total volume of 20 μL of PBS into the right footpad to label CD169$^+$ subscapular macrophages inside the draining LN. Immediately after, the animals were prepared microsurgically for intravital two-photon microscopy as described before (Mempel et al., 2004). Briefly, anesthesia during surgical preparation and imaging was achieved through the ketamine-xylazine method as described above. The right popLN was exposed and positioned with the cortex facing outward with minimal perturbation to afferent lymphatic vessels and surrounding blood vessels, while the animal was immobilized onto a custom-built stage by its hip bone and the vertebral column. The imaging chamber was created around the exposed LN with high vacuum grease (VWR) on the side and a coverslip on top. A thermocouple (Omega) was placed next to the LN to monitor the local temperature, which was maintained between 36.5 and 37°C by a custom-built water bath heating system. Two-photon imaging was performed on a Bio-Rad Radiance 2100MP Confocal/Multiphoton microscopy system with two MaiTai Ti:sapphire lasers (Spectra-Physics) tuned to 800 nm and 900 nm for two photon excitation and second harmonic generation. Z stacks of sensory innervation of the capsular/subcapsular space on the cortical side were acquired in 1 μm steps with a 20 × , 0.95 numerical aperture objective (Olympus).

Subcutaneous challenge by footpad injection of LPS or Pam3CSK4

LPS (Sigma) and Pam3CSK4 (Invivogen) were dissolved in water to a stock concentration of 5mg/ml and 2mg/ml respectively. 50 μg of LPS or 40 μg of Pam3CSK4 were injected into one footpad of adult *Nav1.8*$^{Cre/+}$ *x Rosa26*$^{LSL\text{-}tdTomato/LSL\text{-}tdTomato}$ mice in a total volume of 20 μl, while the contralateral footpad received equal volume of PBS. 3 days later, popLNs were harvested and processed for whole mount immunohistochemistry as described above.

Manual cell sorting for scRNA-seq

Adult mice with retrogradely-labeled LN- or skin-innervating neurons were sacrificed by CO_2 asphyxiation. T13 and L1 DRGs ipsilateral to the side of injection were quickly removed without nerves attached and checked for tdTomato labeling in cold HBSS (1X, no Ca^{2+} or Mg^{2+}) (VWR) under Leica MZ10 F stereomicroscope with fluorescence. DRGs were immediately digested with 1 mL of papain solution (HBSS/10 mM HEPES (VWR)/500 μM EDTA (Westnet)/0.4 mg/mL L-Cysteine (Sigma)/1.5 mM $CaCl_2$ (Sigma)/20 unit/mL Papain (Worthington)) in a 37°C water bath for 10 min, with agitation every 2 min. DRGs were further digested with 1 mL of collagenase type II/dispase solution (HBSS/10 mM HEPES/4 mg/mL collagenase type II (Worthington)/5 mg/mL dispase (Thermo Fisher)) in a 37°C water bath for 30 min, with agitation every 10 min. Following centrifugation at 400 g for 4 min, digested DRGs were mechanically disrupted in 0.2 mL of complete L15 medium (L15 (Invitrogen)/10 mM HEPES/10% FBS (Germini)) by passing them first through a 1000 μL pipette tip up to 10 times, and then through a 200 μL pipette tip up to 5 times until the tissues were fully dissociated. To remove myelin/axonal debris, the cell suspension diluted in 1 mL of complete L15 medium was carefully layered on top of 5 mL of Percoll gradient (L15/10 mM HEPES/20% Percoll (GE Healthcare) and centrifuged at 400 g for 9 min. After removing the supernatant, cells were washed in 2 mL of L15/10 mM HEPES and centrifuged at 750 g for 3 min. Finally, cells were resuspended in 1 mL of cold sorting buffer (L15/10 mM HEPES/1 mg/mL BSA (VWR)/25 μg/mL DNase I (Roche)), and subjected to fluorescence-assisted single-cell picking as described previously (Hempel et al., 2007). Briefly, the cell suspension diluted in 3 mL of sorting buffer was immediately transferred to a 35 mm Petri dish (Scanning dish) with lane markings 6 mm apart and let sit on ice until most cells had settled to the bottom which normally takes 15-20 min. Rare fluorescent cells were readily identified under Leica MZ10 F stereomicroscope with fluorescence (transillumination off) by scanning the bottom of the dish lane by lane to maximize recovery and avoid rescanning. Zoom was set such that the field of view corresponded to the width of a single lane. To pick out fluorescent cells with minimal contamination from nonfluorescent cells, a pulled and trimmed micropipette (World Precision Instruments) was carefully lowered under transillumination into the sorting buffer until it was in the vicinity of the target cell. Simultaneous positive pressure was applied by mouth through the aspiration assembly system, as described above for retrograde labeling. Once the micropipette was in position, the target cell was gently aspirated into the micropipette through capillary action by transient release of positive

pressure. The micropipette was quickly removed to prevent aspiration of unwanted cells or debris. The content of the micropipette, including the target cell, was expelled gently into a droplet of cold fresh sorting buffer on a different 35 mm Petri dish (wash dish 1) under transillumination. Wash dish 1 was kept on ice while subsequent scans for fluorescent cells occurred. Once 16 or all the fluorescent cells, whichever comes first, were collected in wash dish 1, cells were washed two additional times by moving them one by one into a new droplet of sorting buffer on clean 35 mm Petri dishes. Micropipettes were not reused for different cells to avoid cross contamination. After the final wash, each fluorescent cell was pipetted up and down the micropipette three times to remove unwanted contamination before being ejected into 10 μL of cold RLT (QIAGEN) supplemented with 1% β-mercaptoethanol (Sigma) in a 96-well plate, and snap-frozen on dry ice and stored at −80°C. The entire manual sorting procedure was routinely completed in 1.5 hr.

scRNA-seq of neurons using Smart-Seq2

Single-cell libraries were generated according to the SMART-seq2 protocol (Picelli et al., 2014; Trombetta et al., 2014). Briefly, RNA from single-cell lysates was purified using AMPure RNA Clean Spri beads (Beckman Coulter) at a 2.2x volume ratio, and mixed with oligo-dT primer (SMART-seq2 3′ Oligo-dT Primer), dNTPs (NEB), and RNase inhibitor (Fisher Scientific) at 72°C for 3 minutes on a thermal cycler to anneal the 3′ primer to polyadenylated mRNA. Reverse transcription was carried out in a master mix of Maxima RNaseH-minus RT enzyme and buffer (Fisher Scientific), $MgCl_2$ (Sigma), Betaine (Sigma), RNase inhibitor, and a 5′ template switch oligonucleotide (SMART-seq2 5′ TSO) using the following protocol: 42°C for 90 minutes, followed by 10 cycles of 50°C for 2 minutes, 42°C for 2 minutes, and followed by inactivation at 70°C for 15 minutes. Whole transcriptome amplification was achieved by addition of KAPA HiFi HotStart ReadyMix (Kapa Biosystems) and IS PCR primer (ISPCR) to the reverse transcription product and amplification on a thermal cycler using the following protocol: 98°C for 3 minutes, followed by 21 cycles of 98°C for 15 s, 67°C for 20 s, 72°C for 6 minutes, followed by a final 5-minute extension at 72°C. Libraries were purified using AMPure XP SPRI beads at a volume ratio of 0.8x followed by 0.9x. Library size was assessed using a High-Sensitivity DNA chip (Agilent Bioanalyzer), confirming the expected size distribution of ~1000-2000 bp. Tagmentation reactions were carried out with the Nextera XT DNA Sample Preparation Kit (Illumina) using 250 pg of cDNA per single cell as input, with modified manufacturer's instructions as described. Libraries were purified twice with AMPure XP SPRI beads at a volume ratio of 0.9x, size distribution assessed using a High Sensitivity DNA chip (Agilent Bioanalyzer) and Qubit High-Sensitivity DNA kit (Invitrogen). Libraries were pooled and sequenced using NextSeq500/550 High Output v2 kits (75 cycles, Illumina) using 30-30 paired end sequencing with 8-mer dual indexing.

RNAscope

The RNAscope Fluorescent Multiplex Assay (ACD Biosystems) was performed according to RNAscope Multiplex Fluorescent Reagent Kit v2 user manual for fresh-frozen tissue samples. Briefly, 14 μm fresh frozen sections from T13 and L1 DRGs with each side containing retrogradely-labeled tdTomato$^+$ LN- or skin- innervating neurons from the same animal were hybridized with RNAscope probes for *Ptgir* (487851), *tdTomato* (317041-C2), and *Prokr2* (498431-C3) simultaneously. The probes were amplified and detected with TSA plus fluorescein, cyanine 3 and cyanine 5 (Perkin Elmer). The ACD 3-plex negative control probe was run in parallel on separate sections in each experiment to assess the background level and set the acquisition parameter. All sections with *tdTomato*$^+$ cells were imaged at 20x using an Olympus FV3000 confocal imaging system. The frequency of *Ptgir*$^+$ or *Prokr2*$^+$ DRG neurons among the *tdTomato*$^+$ LN- or skin-innervating population was determined by considering all the *tdTomato*$^+$ cells that were recovered and uniquely-defined from a single animal.

Tamoxifen treatment

Tamoxifen (Sigma) was dissolved in corn oil (Sigma) at a concentration of 20 mg/mL by shaking overnight at 37°C, and stored at 4°C for the duration of the injections. For labeling arterial vessels with *Bmx-CreER*^{T2}, 0.5 mg of tamoxifen was delivered intraperitoneally to label arterial ECs into *Bmx-CreER*^{T2}; *Rosa26*$^{eYFP/+}$ animals between 4-6 weeks of age daily for three consecutive days. Animals were analyzed between 1-3 weeks later.

6-OHDA treatment

For sympathetic denervation, the stock solution of 6-hydroxydopamine (6-OHDA) (Sigma) was prepared in water at 42 mg/mL and stored at −20°C. *Nav1.8*$^{Cre/+}$; *Rosa26*$^{LSL\text{-}tdTomato/+}$ animals from the same litter between the ages of 6-12 weeks were injected intraperitoneally with 6-OHDA (100 mg kg^{-1}) or an equal volume of saline daily for 5 consecutive days. Animals were analyzed the following day.

Optogenetic stimulation of iLN-innervating sensory neurons

Age-matched adult *Nav1.8*$^{Cre/+}$; *Rosa26*$^{LSL\text{-}ChR2\text{-}eYFP/+}$ (ChR2+) or *Nav1.8*$^{Cre/+}$; *Rosa26*$^{LSL\text{-}eYFP/+}$ (ChR2-) animals (6-12 weeks) were deeply anesthetized (isoflurane, 1.5%–2%, Patterson Vet) maintained at normal body temperature with a water bath heating system (Baxter) during surgical preparation and photostimulation. The animals were surgically prepared for intravital optogenetic stimulation using a method that was adapted from a previously-described protocol for intravital microcopy of iLNs (von Andrian, 1996). Briefly, the skin with the left iLN was flipped inside out following a small incision immediately left to the midline and glued onto a metal block to keep the medulla side of LN exposed. Care was taken not to overstretch the skin flap and damage lymphatic and blood vessels. The

Please cite this article in press as: Huang et al., Lymph nodes are innervated by a unique population of sensory neurons with immunomodulatory potential, Cell (2021), https://doi.org/10.1016/j.cell.2020.11.028

site of illumination, the branch point of the antero-posterior-running segment of the y-shaped superficial epigastric artery from where LN feeding arterioles emerged was located and exposed with microdissection without compromising the blood vessel integrity while the tissue was kept moist with normal saline. The stimulation chamber was then built around the iLN with vacuum grease on the side to keep solution from leaking, as well as a metal hairpin shaped tubing with hot water flowing inside on top of vacuum grease to maintain the tissue between 36.5 and 37°C. A thermocouple was placed next to the branch point to monitor the temperature at the tissue. An optic fiber (200 μm core, Thorlabs) coupled to a DPSS laser light source (473 nm, Shanghai Laser & Optics Century) was positioned for focal illumination directly on top of the branch point. The stimulation chamber was subsequently filled to the metal tubing with GenTeal Tears Lubricant Eye Gel (Alcon) to keep the tissue from drying out during stimulation. Pulsed light stimulation (5 ms pulses, 125 mW/mm^2 intensity, 20 Hz) was delivered to the targeted region for 3 hr under the control of a shutter system (Uniblitz). iLNs from both sides were immediately removed after light stimulation and kept in ice cold LN media (HBSS (Corning)/2% FBS/10 mM HEPES/2 mM $CaCl_2$) until subsequent processing.

LN Dissociation and Single Cell Isolation

LNs were kept on ice until processing, < 60 minutes between animal sacrifice and tissue digestion. To minimize biases introduced during tissue dissociation, a gentle dissociation protocol optimized for reliable isolation of both stromal and hemopoietic LN cells was used to generate a suspension of single cells from both the non-immune and the immune compartments (Fletcher et al., 2011). LN media was aspirated, and each LN was placed in 1 mL of pre-warmed digestion media (0.8 mg/mL dispase, 0.2 mg/mL collagenase P (Roche), 50 μg/mL of DNase I in LN media). Using a pair of needle-nose forceps, the capsule of each LN was gently pierced, and the LN in digestion media were placed in a 37°C water bath for 20 minutes with no agitation. Next, LNs were gently agitated without touching the tissue, pelleted by gravity, and the 1 mL of digestion media supernatant was removed and placed in a collection tube on ice containing 10 mL of quenching buffer (PBS/5 mM EDTA/5% FBS). A fresh 1 mL of digestion buffer was added to each LN, and the LNs were placed back in the 37°C water bath for an additional 5 minutes. The LN was gently agitated and triturated using a 1000 μL pipette tip, solid capsular and stromal matter was allowed to settle to the bottom of the tube without centrifuging, and the supernatant digestion media was added to the same collection tube containing quenching buffer. 5-minute incubation periods in fresh digestion buffer and trituration with a 1000 μL pipette tip continued until LNs were completely digested, typically requiring 3-4 additional digestion steps. The cellular suspension in quenching buffer was filtered through a 100 μm filter, and washed with an additional 15 mL of quenching buffer. Single-cell suspensions were centrifuged at 300 g for 3 minutes at 4°C, and counted using a hemocytometer and light microscope. We recovered an average of 4.00 ± 0.53 million cells per LN, and observed no differences in cellularity by treatment group or animal genotype. We saved an aliquot of 60,000 cells from each sample in quenching media on ice as the unenriched sample, and centrifuged the remaining cells at 300 g for 3 minutes at 4°C. Next, using the Miltenyi CD3ε microbead kit and CD19 mouse microbead kit, all remaining LN cells were stained according to manufacturer instructions with the following modifications. First, single cells were stained with CD3ε biotin for 10 minutes on ice, washed once with MACS buffer (PBS/0.5% BSA (Sigma)/2 mM EDTA) and stained simultaneously with CD19 microbeads and biotin microbeads. Cells were isolated using LD columns (Miltenyi) according to manufacturer specifications and the flow-through was collected as the non-T and non-B enriched sample. Single cells from both enriched and unenriched samples were pelleted by centrifugation at 300 g for 3 minutes at 4°C, and counted using a hemocytometer with trypan blue staining to estimate cell viability. Across 14 LNs, we recovered an average of 270,000 ± 31,000 (mean ± SEM) cells per lymph node following CD3ε and CD19 depletion with > 90% viability.

For LN cellularity analysis, single-cell suspensions of the two iLNs from the same ChR2+ or ChR2- mouse (6-12 weeks) were prepared as above. The cells were then filtered through steel mesh and resuspended at the appropriate cell density in FACS buffer before being acquired on a BD Accuri C6 Plus flow cytometer (BD Biosciences).

LN scRNA-seq using Seq-Well

Single cells from each lymph node prior to and post CD3ε and CD19 depletion were kept separate and diluted to 15,000 cells in 200 μL complete media (RPMI 1640/10% FBS). Seq-Well was performed as described with changes noted below (Aicher et al., 2019; Gierahn et al., 2017). Briefly, a pre-functionalized PDMS array containing ~86,000 nanowells was loaded with uniquely-barcoded mRNA capture beads (ChemGenes) (Macosko et al., 2015) and suspended in complete media for at least 20 minutes. 15,000 cells were deposited onto the top of each PDMS array and let settle by gravity into distinct wells. The array was gently washed with PBS, and sealed using a functionalized polycarbonate membrane with a pore size of 0.01 μm, which allows exchange of buffers without permitting mixing of cell materials between different wells. Seq-Well arrays were sealed in a dry 37°C oven for 40 minutes, and submerged in a lysis buffer containing 5 M guanidium thiocyanate (Sigma), 1 mM EDTA, 1% beta-mercaptoethanol and 0.05% sarkosyl (Sigma) for 20 minutes at room temperature. Arrays were transferred to hybridization buffer containing 2 M NaCl (Fisher Scientific) with 8% (v/v) polyethylene glycol (PEG, Sigma) and agitated for 40 minutes at room temperature, mRNA capture beads with mRNA hybridized were collected from each Seq-Well array, and beads were resuspended in a master mix for reverse transcription containing Maxima H Minus Reverse Transcriptase and buffer, dNTPs, RNase inhibitor, a 5′ template switch oligonucleotide (Seq-Well 5′ TSO), and PEG for 30 minutes at room temperature, and overnight at 52°C with end-over-end rotation. Exonuclease digestion was carried out as described previously: beads were washed with TE with 0.01% tween-20 (Fisher Scientific) and TE with 0.5% SDS (Sigma), denatured while rotating for 5 minutes in 0.2 mM NaOH, and resuspended in ExoI (NEB) for 1 hour at 37°C with end-over-end rotation (Hughes et al., 2019). Next, beads were washed with TE + 0.01% tween-20, and second strand synthesis was carried out by

resuspending beads in a master mix containing Klenow Fragment (NEB), dNTPs, PEG, and the dN-SMRT oligonucleotide (Seq-Well Second Strand Primer) to enable random priming off of the beads. PCR was carried out as described using 2X KAPA HiFi Hotstart Readymix and ISPCR primer (Seq-Well ISPCR), and placed on a thermal cycler using the following protocol: 95°C for 3 minutes, followed by 4 cycles of 98°C for 20 s, 65°C for 45 s, 72°C for 3 minutes, followed by 12 cycles of 98°C for 20 s, 67°C for 20 s, 72°C for 3 minutes, followed by a final 5-minute extension at 72°C. Post-whole transcriptome amplification proceeded as described above for SMART-seq2 libraries, with the following exceptions: AMPure XP SPRI bead cleanup occurred first at a 0.6 x volume ratio, followed by 0.8x. Library size was analyzed using an Agilent Tapestation hsD5000 kit, confirming the expected peak at ~1000 bp, and absence of smaller peaks corresponding to primer. Libraries were quantified using Qubit High-Sensitivity DNA kit and prepared for Illumina sequencing using Nextera XT DNA Sample Preparation kit using 900 pg of cDNA library as input to tagmentation reactions. Amplified final libraries were purified twice with AMPure XP SPRI beads as before, with a volume ratio of 0.6x followed by 0.8x. Libraries from 3 Seq-Well arrays were pooled and sequenced together using a NextSeq 500/550 High Output v2 kit (75 cycles) using a paired end read structure with custom read 1 primer (Seq-Well CR1P): read 1: 20 bases, read 2: 50 bases, read 1 index: 8 bases.

QUANTIFICATION AND STATISTICAL ANALYSIS

Image analysis

All image analyses were performed in Imaris 9.2.1 or 7.4.2 as detailed below. To better visualize neuronal architecture in or/and around LNs, for all LN images except for Figures 7K, 7L, S1B, S2D, S2E, S3A, S3D, and S7A, an isosurface for the LN was generated by manually drawing LN contours on 2D slices every fifth slice and was used to mask the original images so that only what was inside the LN mask was shown. Depending on the purpose of the experiment, LN isosurfaces were defined with varying degrees of stringency: based on the outermost layer of LECs in Figures 2A and 2C and S2A, on collagen type I staining in Figure 2F, on SMA staining in Figures 2D, 2E and S2B, or on GFP background staining in Figure S1A or on tdTomato background staining everywhere else. In Figures 2A, 2C–2F, S2A, S2B, and S3H, additional masking of the channel(s) where nerves were stained was performed with isosurfaces generated for neuronal signal within LNs based on morphology, i.e., fiber-like structures that can be traced through multiple slices, to highlight neuronal structures. To better visualize fibers in the capsular/subcapsular space of LNs as shown in Figure 2F, intranodal sensory fibers and total sensory fibers within and below the capsule were isolated by masking the original channel with LN isosurfaces defined based on GFP (LECs) and collagen type I staining, respectively. The resulting channel after subtracting the former channel from the latter one corresponds to the capsular/subcapsular plexus. Original, processed images and rendered isosurfaces were viewed as 3D reconstructions in surpass view with orthogonal camera setting unless indicated otherwise.

For quantification of innervation density of LNs as in Figures 1C–1F, relevant channels were first masked with the LN isosurface as described above. Isosurfaces for sensory and sympathetic fibers within the masked channels, i.e., inside the LN, were then generated by automatic creation based on features that distinguish neuronal signal from everything else, e.g., intensity, sphericity, followed by manual editing. Sensory or sympathetic fiber density for a given LN was defined as the ratio of the volume of isosurfaces for sensory or sympathetic fibers within the LN to that for the LN. Similar steps were taken to generate isosurfaces for sensory fibers inside the LNs for 3D rendering and quantification in Figures 5G–5N.

For quantification of penetration depth of intranodal sensory fibers, the outermost layer of LECs, which demarcates the LN boundary, was used to precisely segment LNs into isosurfaces. Isosurfaces for intranodal sensory fibers, sensory fibers within the relevant channel after applying the LN isosurface as a mask, were generated as described above. Using the distance transformation function, the closest distance from any given voxel within the LN isosurface to the surface of the LN in μm was computed and converted into an intensity value for that given voxel in a separate channel. To determine penetration depth of intranodal sensory fibers, the distance transformation channel was masked against isosurfaces for intranodal sensory fibers to generate a new channel where the penetration depth at any given voxel within the intranodal sensory fibers was encoded as the intensity value for that specific voxel with the maximum intensity value representing the maximum penetration depth for a given LN. Such a channel, when displayed in surpass view as in Figure 2A, allowed direct visualization of the spatial relationship between intranodal sensory fibers and the nearest LN surface. Additionally, the penetration depth of intranodal sensory fibers was described in Figure 2B in the form of the percentage of total intranodal fibers found within LN spaces with increasing distance away from the LN surface. For that analysis, the original distance transformation channel, as described above, was used to create a series of isosurfaces of decreasing sizes which represent increasingly-deep LN spaces with its closest distance to the LN surface increasing from 0 to 100 μm with 10 μm intervals. For example, 10 was set as the intensity threshold cutoff during automatic creation so that all voxels with intensity value larger than and equal to 10 were selected in one single surface which corresponds to the LN space 10 μm and more below the LN surface. To calculate the percentage of total intranodal sensory fibers in any of those LN spaces, the isosurface for total sensory fibers and that for a said LN space, e.g., 10 μm and more below the surface, as described above, were each used to generate their corresponding binary channels, where all voxels outside of a surface were set as 0, while those inside were set at 100. Colocalization analysis was then performed on those two binary channels, and the percentage of non 0 voxels in the binary nerve channel that were colocalized corresponded to the percentage of total intranodal sensory fibers found 10 μm and more below the LN surface. This process was repeated for increasingly smaller LN spaces with 10 μm interval. The percentage of total intranodal fibers in LN spaces in the form of 10um bins from 0 to 100 μm, e.g., 10-20 μm, was further derived from serial subtraction of the percentage in the LN space

that is 10um deeper, e.g., (20 μm and more below the surface), from that in the current LN space, e.g., (10 μm and more below the surface), as shown in Figure 2B.

Neuron scRNA-seq data preprocessing

Single cells were sequenced to a depth of 1.6 ± 0.1 million (mean ± SEM) reads per cell. Pooled libraries were demultiplexed using bcl2fastq (v2.17.1.14) with default settings, and aligned using STAR (Dobin et al., 2013) to the mouse UCSC genome reference (version mm10), and a gene expression matrix was generated using RSEM (v1.2.3) in paired-end mode. Single-cell libraries with fewer than 3,000 unique genes and fewer than 17% of reads mapping to transcriptomic regions were excluded from subsequent analysis, resulting in a final dataset of 52 LN-innervating neurons collected from 8 mice, and 31 skin-innervating neurons collected from 4 mice. Among cells retained for analysis, the number of unique genes captured was 9,843 ± 229 (mean ± SEM) among LN-innervating neurons and 9,653 ± 302 among skin-innervating neurons. Libraries from LN-innervating neurons contained 50.45 ± 2.3% transcriptome-aligning fragments, libraries from skin-innervating neurons contained 58.33 ± 2.9%. Among all alignment and library quality metrics assessed, we found no significant differences between LN-innervating and skin-innervating neurons. All analysis of gene expression was completed using the normalized RSEM output as transcripts per million (TPM).

Neuron scRNA-seq differential gene expression

All analyses of scRNA-seq data was carried out using the R language for Statistical Computing. Single-cell libraries were first assessed for expression of canonical neuronal markers and known lineage-defining genes from accompanying imaging data, such as Nav1.8 (*Scn10a*) and tyrosine hydroxylase (*Th*). The full list of markers is supplied in Table S1. To directly assess differences in gene expression between LN-innervating and skin-innervating neurons, we used the R package Single Cell Differential Expression (SCDE, version 1.99.1) with default input parameters (Fan et al., 2016; Kharchenko et al., 2014). A cutoff of Holm-corrected Z score > 1.96 or < −1.96 (corresponding to a corrected p value < 0.05) was used to identify significantly DE genes for subsequent analysis. Heatmaps were created using the R package gplots (version 3.0.1). DAVID was used for analysis of over-represented gene ontologies over significantly DE genes (Huang et al., 2009a, 2009b).

Analysis of neuron scRNA-seq in the context of previously published datasets

As our target-specific single cells do not represent the full diversity of neurons contained in the DRG, we utilized the scRNA-seq atlas published by Usoskin et al. (2015) (subsequently referred to as the "Usoskin, Furlan Atlas" to classify our cells. Using the raw data and accompanying metadata hosted at http://linnarssonlab.org/drg/, we first identified the intersection of expressed genes from the Usoskin, Furlan Atlas and LN-innervating and skin-innervating single cells, and eliminated cells identified as non-neuronal ("NoN" and "NoN outlier") from the Usoskin, Furlan Atlas, resulting in a dataset of 148 neurofilamentous (NF), 81 peptidergic (PEP), 251 tyrosine hydroxylase (TH), 169 non-peptidergic (NP), and 39 "Central, unsolved" cells. To mimic the dimensionality reduction methods the previous authors used to identify major neuronal cell types, we transformed the data as $\log_2$(1+TPM), and calculated the gene variance across all cells. We cut to genes with a variance $\log_2$(1+TPM) > 0.5, resulting in 11,778 genes. Next, we performed principal component analysis over the $\log_2$-transformed, mean-centered data, and found that PC_2 and PC_4 reflected major axes of variability between TH, PEP, NF, and NP cell types – identified by the authors of the previous study as "Level.1" cell type subsets (Figure S4A). To identify how LN-innervating and skin-innervating cells related to major DRG cell types in a reduced dimensional space, we projected our target-specific data into PC_2 and PC_4 of the Usoskin, Furlan Atlas. This was completed by first calculating the principal components:

$$\mathbf{X} - \boldsymbol{c}_m = \mathbf{USV}^{\mathrm{T}} \quad \text{(Equation 1)}$$

where X is the $\log_2$(1+TPM) data matrix of M genes by N cells from the Usoskin, Furlan Atlas. Equation 1 calculates the singular value decomposition of this matrix after subtracting the average of each row (gene) of X, denoted c_m, from X. U represents a matrix of M orthonormal vectors corresponding to M genes and V represents a matrix of N orthonormal vectors corresponding to N cells. To apply this same dimensionality reduction transformation to our new dataset of LN-innervating and skin-innervating single cells, Y, we use Equation 2:

$$\mathbf{PC}_{\mathrm{i}} = \sum_{\mathrm{m}=1}^{\mathrm{M}} (\mathbf{Y} - \boldsymbol{c}_m)\mathbf{u}_{\mathrm{i}} \quad \text{(Equation 2)}$$

Y represents the $\log_2$(1+TPM) transformed matrix of our innervation-target-specific data, c_m refers to the same vector of row (gene) averages calculated from X. The centered Y matrix is multiplied as a dot product with the i^{th} principal component gene eigenvector, or the i^{th} column vector of U, denoted u_i. By taking the sum over all transformed rows for each column (cell), we project the LN-innervating and skin-innervating data (Y) into the principal component space calculated for the Usoskin, Furlan Atlas (X), denoted PC_i. This data is visualized by plotting the PC_2 and PC_4 vectors from the Usoskin, Furlan Atlas (transparent circles, Figure S4A), with the PC_2 and PC_4 vectors from the transformed LN-innervating and skin-innervating cells (filled squares). The Euclidean distance between each innervation-target-specific single cell and all cells within the Usoskin, Furlan Atlas was calculated over PC2 and PC4

(Figure S4B). The range of cell-to-cell Euclidean distances between like-cells (e.g., PEP-to-PEP) within the Usoskin, Furlan Atlas is represented by a dashed line corresponding to the 99%ile.

We similarly analyzed our LN-innervating and skin-innervating single cell transcriptomes in the context of an expanded dataset of somatosensory neurons published by Sharma et al. (2020) (subsequently referred to as the "Sharma Atlas"). Here, authors generated data from 10,922 cells from cervical, thoracic, and lumbar dorsal root ganglia, uncovering at least 15 transcriptionally distinct cell types/states. Unlike the Usoskin, Furlan Atlas, the cell types in the Sharma Atlas could not be sufficiently represented in two-dimensional principal components space. Using the JackStraw method from the Seurat package to identify significant principal components, we recovered 32 significant principal components. As with the Usoskin, Furlan Atlas, we next projected the LN-innervating and skin-innervating single cell transcriptomes into the 32-dimensional principal components space defined by the Sharma Atlas according to Equation 2, and created a joint principal component matrix of cells x $PC_{1\text{-}32}$ including cells from the Sharma Atlas, LN-innervating neurons, and skin-innervating neurons. Finally, we constructed a shared nearest-neighbor graph over this joint matrix and visualized single cells in a two-dimensional uniform manifold approximation and projection (UMAP) plot (Figures 4A and 4B). To establish cell similarity, we used label propagation methods over a shared nearest-neighbor graph built from the 32-dimensional projected space, similar to other published methods for single-cell transcriptomic integration (Barkas et al., 2019; Stuart et al., 2019). Here, "unknown" cells (from the LN-innervating or skin-innervating datasets) were each queried for their top 100 nearest neighbors, and cellular identity was predicted based on a consensus identity of the cell's neighbors. Results from label propagation are presented in Figure 4C.

To analyze the expression similarity between each single cell from our target-specific dataset and the data in the Usoskin, Furlan Atlas and Sharma Atlas in a more directed, supervised manner, we assessed how each single cell correlated with each neuron subtype defined by each Atlas. For the Usoskin, Furlan Atlas, we elected to use the more detailed neuronal subtypes, termed "Level.3," which breaks some of the major neuron subtypes, NP, PEP, and NF, into subtypes based on intra-population diversity. For both Atlases, we calculated the average gene expression for each neuron subtype (e.g., NP1) over the $\log_2$(1+TPM) transformed single-cell data, generating pseudo-population averages for each neuron subtype. Next, we only considered genes in our pseudo-population averages that were designated as "subtype-defining" by the Usoskin et al. (2015) analysis, corresponding to the top 50 genes upregulated within each cell type when compared to all other cell types in their dataset, yielding 379 unique genes. For the Sharma Atlas, we restricted genes to the 700 genes defined by the authors as "subtype specific" and provided as supplemental data 1 in their manuscript. We similarly restricted our LN-innervating and skin-innervating single-cell libraries to only these 379 unique genes (for comparison to the Usoskin, Furlan Atlas) or 700 unique genes (for comparison to the Sharma Atlas), and calculated the Spearman correlation between each target-specific single cell (following $\log_2$(1+TPM) transformation) and the pseudo-population averages. The results from this analysis are presented in Figure 4D for comparison to the Sharma Atlas, and Figure S4C for comparison to the Usoskin, Furlan Atlas. We clustered LN-innervating and skin-innervating single cells by their correlation with the Usoskin, Furlan Atlas pseudo-population using complete linkage clustering, and using a cut height of 0.8 retained 4 distinct Neuron Types: Neuron type 1 (LN-innervating cells: 25, skin-innervating cells: 9), Neuron type 2 (LN-innervating cells: 1, skin-innervating cells: 14), Neuron type 3 (LN-innervating cells: 23, skin-innervating cells: 5), and Neuron type 4 (LN-innervating cells: 3, skin-innervating cells: 3) (Figure S4C). We confirmed these clusters were largely stable and in agreement with the partitions created in comparison with the Sharma Atlas (Figure 4D). Neuron Types 1 and 3, which share the strongest similarity with CGRP-η, -ξ, -α, -β -γ, and -ε subtypes defined by Sharma et al. (2020) (and highest similarity with PEP1 and PEP2 subtypes defined by Usoskin et al. (2015), were enriched in the LN-innervating population relative to the skin-innervating population (LN-innervating: 48% Neuron Type 1, 44% Neuron Type 3; skin-innervating: 29% Neuron Type 1, 16% Neuron Type 3). Conversely, Neuron Types 2 and 4 were underrepresented in the LN-innervating population compared to the skin-innervating population (LN-innervating: 2% Neuron Type 2, 6% Neuron Type 4; skin-innervating: 45% Neuron Type 2, 10% Neuron Type 4).

To assess the gene expression phenotype of each Neuron Type, we used SCDE to identify DE genes between cells of each Neuron Type compared to all cells of the 3 remaining Neuron Types. SCDE was run as described above with default input parameters, genes with a Holm-corrected p value < 0.01 were considered significant and presented in Figure 4F and Table S1.

LN Seq-Well data preprocessing

Reads were aligned and processed according to the Drop-Seq Computational Protocol v2.0 (https://github.com/broadinstitute/Drop-seq). Briefly, reads were first demultiplexed according to index read 1 using bcl2fastq (v2.17.1.14) with default settings. Read 1 was split into the first 12 base pairs corresponding to the cell barcode (CB), and the 13-20^{th} base pairs, which encode the unique molecular identifier (UMI). CBs, UMIs, and read 2 sequences with low base quality were discarded, as were any that contained non-random sequences (e.g., primer sequences, poly-A tails). Following CB and UMI tagging, read 2 was aligned to the mouse genome (version mm10) using STAR v2.5.2b with default parameters including "–limitOutSJcollapsed 1000000–twopassMode Basic." STAR alignments were merged to recover cell and molecular barcodes, and any sequences within hamming edit distance 1 were merged, as these likely originated from the same original sequence. Additional methods to correct for bead synthesis errors in the CB or UMI are detailed in the Drop-Seq Computational Protocol v2.0 ("DetectBeadSynthesisErrors" function). Digital gene expression matrices for each array were retained following quality filtering and UMI-correction, and further processed using the R language for Statistical Computing. Cells with fewer than 300 unique genes were removed from analysis.

Please cite this article in press as: Huang et al., Lymph nodes are innervated by a unique population of sensory neurons with immunomodulatory potential, Cell (2021), https://doi.org/10.1016/j.cell.2020.11.028

Dimensionality reduction, clustering, visualization, and cell type identification of LN Seq-Well data

We restricted our primary analysis of LN-resident cell types to only arrays corresponding to steady state iLN without surgical manipulation or optogenetic stimulation. A total of 9,662 cells were retained with 25,929 unique genes expressed across 7 mice with 1 LN per mouse. For 2 mice, we sequenced arrays corresponding to all LN cells prior to CD3ε/CD19 depletion as well as CD3ε/CD19 depleted cells on a separate array. The average cell recovery per array was 1,074 ± 141 (mean ± SEM) cells, with an average gene count of 1,581 ± 11 genes and average UMI per cell of 4,251 ± 48 UMI (mean ± SEM). Data was normalized and scaled using the Seurat R package (https://github.com/satija.lab/seurat; Butler et al., 2018): transforming the data to $\log_e$(UMI+1) and applying a scale factor of 10,000. We confirmed equivalent depth and cell quality across each of our arrays and the absence of major batch effects introduced by sequencing work-up day or other technical factors, and thus did not regress any batch-related covariates out of our data, including individual cell quality or mitochondrial percent. To identify major axes of variation within our data, we first subsetted our data to only highly-variable genes across all cells – all genes with dispersion (calculated as the variance to mean ratio) > 1.1 were kept, resulting in 2,348 variable genes. Principal component analysis was applied to the cells cut to variable genes for the top 100 principal components. Using the JackStraw function within Seurat, we identified the top significant PCs, and compared these significant PCs to the variance explained by each dimension, ultimately choosing 41 PCs for subsequent clustering and further dimensionality reduction (Shekhar et al., 2016). Critically, we completed all of the following analysis over a range of variable gene cutoffs and principal components to ensure that our cell identification results were robust to parameter choice.

For 2D visualization, we used the Barnes-Hut implementation of t-distributed stochastic neighbor embedding (t-SNE) with "perplexity" set to 40. This tSNE projection of the steady state LN atlas is represented in Figures 6B and S5A. To identify clusters of transcriptionally-similar cells, we employed unsupervised clustering with the Louvain algorithm with the Jaccard correction (Blondel et al., 2008). Briefly, this method involves constructing a k-nearest neighbor graph over the Euclidean distance between cells in the 41-PC reduced space, followed by a shared nearest neighbor (SNN)-based clustering and modularity optimization (Waltman and Van Eck, 2013). We implemented this using the FindClusters tool within the Seurat R package with default parameters and k.param set to 20 and resolution set to 0.4. Here, we intentionally underclustered our data to avoid erroneously splitting cells with shared cell type functions, as the variable genes calculated for this dimensionally-reduced space likely did not fully reflect more nuanced cell type differences (e.g., variable behavior between Neutrophil subtypes). The "Parent Cluster" results from first-pass cell type clustering are represented in the tSNE plot and clusters identified in Figure S5A. We used the Seurat function FindAllMarkers to identify differentially-expressed genes upregulated within each cluster compared to all other cells in the dataset, and tested differential expression using the likelihood-ratio test for single-cell gene expression (by setting test.use to "bimod") (McDavid et al., 2013). The top 100 differentially-expressed genes for each cluster were analyzed, as ranked by the average fold change and restricted to only those with FDR-corrected p values < 0.05. Next, to assess if any cell subtypes existed within each cluster, we restricted our data to only cells within a single "Parent Cluster," and recalculated the variable genes over these cells. The above analysis, from calculation of variable genes to tSNE visualization and cluster identification, was repeated for each cluster listed in Figure S5A. Cell types for which we could identify sub-clusters with significant differentially-expressed genes are marked with asterisks next to their names in Figure S5A, and the sub-cluster tSNE projections and top differentially expressed genes are represented in Figures S5B–S5O. For the T cell parent cluster, we required two iterative sub-clustering steps to fully enumerate all constituent cell types: the first clustering step differentiated regulatory T cells (Tregs) from the remaining T cells (Figures S5B and S5C), and subsequent clustering on the non-Treg T cells uncovered CD4 T cells versus CD8 T cells. All differentially-expressed genes within each subcluster can be found in Table S2.

After exhaustive assessment for cell subclusters within each cell type, we identified 24 unique cell types within our steady state dataset (Figure 6B). We calculated the differentially expressed genes between each cell type and all other cells using a likelihood ratio test (using the FindAllMarkers function with test.use set to "bimod"), the results of this analysis are presented in Figures 6C and S5P and Table S2. By identifying canonical marker genes within these DE gene lists from the literature and using resources such as ImmGen (Heng et al., 2008), we attributed cell identities to each cell type within our dataset, as named in Figures 6B, 6C, and S5P. We recovered two populations of blood endothelial cells, one of which likely corresponds to HEV endothelial cells (HEC), based on uniform and high expression of well-established HEC markers, e.g., *Ccl21a*, *Fut7*, *Chst4* (Figures S5H and S5I; Homeister et al., 2001; Kawashima et al., 2005; Stein et al., 2000; Uchimura et al., 2005). The second blood endothelial cell cluster, termed BEC, includes a heterogeneous set of non-HEV endothelial cells, including arterial, capillary, and non-HEV venular cells (Figures S5H and S5I; Vanlandewijck et al., 2018). Additionally, we identified two distinct populations of *Prox1*$^+$ lymphatic endothelial cells (LECs), with LEC 1 likely representing a mixture of LECs lining the floor of SCS and medullary sinuses based on *Madcam1, Msr1, Bmp2, Vcam1,* and *CD274* (PD-L1) expression profiles (Cohen et al., 2014; Cordeiro et al., 2016; Takeda et al., 2019), and LEC 2 defined by unique expression of multiple extracellular matrix or structural proteins, including *Fbln2, Aqp1, Fbln5, Tnc and Reln* (Figures S5N and S5O). Interestingly, cells within the LEC 2 cluster shared molecular signatures with LECs positioned at the ceiling of SCS, within the cortical sinuses, and lining lymphatic vessels, including selective expression of *Emcn*, *Ackr4*, *Ackr2*, *Klf2*, *Fabp4* and *Cav1* (Iftakhar-E-Khuda et al., 2016; Takeda et al., 2019; Ulvmar et al., 2014). We also identified a subtype of dendritic-cell-like cells (Aire$^+$ APC), which likely represent the Aire-expressing ILC3-like cells that were described recently (Yamano et al., 2019). Similarly, we detected two subtypes of neutrophils, Neutrophils 1 and 2, which potentially reflect distinct maturation states similar to what was recently described for bone marrow neutrophils (Evrard et al., 2018; Figures S5L and S5M): Neutrophils 1 expressed components of neutrophil granules and effector molecules at high levels, including *Elane, Prtn3, Ctsg, Ngp, Ltf, Camp,* and *Mpo*, whereas

Neutrophils 2 expressed little or no effector molecules, but elevated levels of pro-inflammatory genes, including leukocyte traffic molecules, chemokines, cytokines, and cytokine receptors such as *Sell, Ccl4, Cxcr2, Cxcl2, Ccl6, Il1b,* and *Csf3r*.

Analysis of cellular receptor-ligand pairs

We reasoned that cells or cell types within the LN that interact with innervating neurons would likely express proteins that enable such contact or communication. As we generated unbiased single-cell transcriptomic data from LN-innervating neurons and the potential targeted cell types, we incorporated databases of ligand and receptor pairs to understand if any of the LN-resident cell types expressed a high abundance of cognate molecules, and would thus be poised to interact with innervating neurons. A general schematic of this method is provided in Figure S6A. We used the database of receptor-ligand interactions curated by Ramilowski et al. (Ramilowski et al., 2015), which consists of 2,422 total interactions over 708 unique genes (originally provided as human genes, and converted to mouse orthologs using the HUGO database). First, data from LN-innervating neurons was limited to only genes with non-negligible expression, using a cutoff of average $\log_2(1+TPM) > 3$, yielding 6,666 total genes for subsequent analysis. The intersection of genes within the Ramilowski interaction database and those expressed at non-negligible levels among LN-innervating neurons yielded 184 total genes. After limiting to only interactions with at least one participating gene expressed in the LN-innervating neurons, the interaction database was restricted to 750 total receptor-ligand pairs, and 471 unique potential cognates. We next assessed the expression of these 471 cognate genes within the LN-resident cell atlas. First, we summarized the expression of individual cells within the LN-resident atlas by taking the pseudo-population average of each cell type (over non-log single-cell data). We limited the LN-resident atlas data to only genes with non-negligible expression across all cell type pseudo-populations, cutting to genes with an average UMI expression > 1, yielding 256 total potential cognates (from the previous 471). Next, we developed a summary statistic to reflect the abundance of neuron cognates expressed within LN-resident cell types. First, we scaled our data by subtracting the mean and dividing by the standard deviation for each individual gene – this enabled us to assess the contribution of all genes equally such that signal was not dominated by genes with high total expression (Figure 6E). Finally, we calculated the "Interaction Potential" (IP) as the mean of these scaled values for each cell type: cell types that expressed relatively higher abundances of all candidate neuron-cognates received a higher IP score. Our null model states that the interaction potentials we calculated are no more extreme than the IP we would have recovered by chance. To test our experimentally-derived IP, we generated a null distribution by shuffling the cell type labels over all single cells within the LN-resident cell atlas, and repeated the "cell type" averaging, scaling, and IP calculation for 1,000 permutations. By comparing our true IP scores to the null distribution, we were able to identify certain cell types with significantly higher IP than observed by chance, and could attribute a P value to each cell type (Figure 6F, 99% confidence interval denoted by dashed line). IP scores were re-scaled such that the lower bound of the 99% confidence interval was equal to 0 for clarity. The results of this approach are presented in Figures 6D–6F, S6A, and S6B.

Crucially, we were concerned that the method of calculation of the IP, the summary statistics applied, the choice of raw versus scaled data, or confounding factors that differentiate cell types, including average genes/cell and number of cells per cell type, would influence our ranked list of top interacting cell types and bias our results. For example, we wondered whether differences in quality metrics or other technical factors between cell types might result in higher or lower IP rankings – for instance, a cell type with significantly higher RNA recovery per cell than another cell type would appear to have a higher interaction potential. We found no correlation between the IP (as reported in Figure 6F) and the median UMI per cell for each cell type (Figure S6B, $p = 0.32$). To address bias introduced by our choice in summary statistic or data normalization, we repeated the above pipeline without gene-wise scaling across cell types (Figure S6C), or by calculating the percent of cells with non-zero expression of a given gene, in the place of calculating of average expression per cell type (Figure S6D). In both of these cases, we observed that non-endothelial stroma, LEC 1, LEC 2, BEC, and HEC remained the top-scoring cell types for Interaction Potential (significance calculated by permutation test as described above). Finally, we reasoned that variations in the number of cells per cell type might limit our ability to compare between different cell types. We iteratively down-sampled our single-cell data to analyze interaction potentials (using the method in Figures 6D–6F) for only 25 total cells per cell type – the histograms of these calculations after 1,000 iterations are plotted in Figure S6E. Critically, non-endothelial stroma, LEC 1, LEC 2, BEC, and HEC cell types remained top-ranking in Interaction Potential after controlling for cell abundance per cell type.

Finally, we derived an alternative statistical testing strategy to assess the overrepresentation of neuron-interaction cognates among expressed genes between different cell types. Here, we binarized our data to classify genes as "expressed" or "not expressed" within a cell type, using an average gene expression cutoff of 1. We considered the list of 256 potential neuronal cognate genes, and used a Fisher's Exact Test to assess whether the cognate gene list was overrepresented among expressed genes for a given cell type (mimicking the field-standard for gene ontology enrichment analysis) (Huang et al., 2009a, 2009b), and a Holm correction to adjust for multiple tests. In close agreement with the results from our interaction potential statistic above, we found significant overrepresentation of potential neuronal cognate genes in the following cell types (listed in decreasing statistical significance): non-endothelial stroma ($p = 1.6 \times 10^{-28}$), BEC ($p = 2.5 \times 10^{-22}$), LEC 1 ($p = 4.5 \times 10^{-22}$), HEC ($p = 8.3 \times 10^{-21}$), LEC 2 ($p = 9.6 \times 10^{-20}$), Macrophages ($p = 8.7 \times 10^{-9}$), Mast Cells ($p = 6.5 \times 10^{-8}$), Neutrophils 2 ($p = 5.2 \times 10^{-6}$), Neutrophils 1 ($p = 1.8 \times 10^{-4}$), pDC ($p = 1.7 \times 10^{-3}$), *Aire*$^+$ APCs ($p = 3.4 \times 10^{-3}$), and cDC2 (8.9×10^{-3}). All other cell types were non-significant by a Holm-adjusted p value cutoff of 0.01. Critically, this ranking was not sensitive to the choice of binarization cutoff, tested over a range of 0.5 – 10 UMI, data not shown).

Please cite this article in press as: Huang et al., Lymph nodes are innervated by a unique population of sensory neurons with immunomodulatory potential, Cell (2021), https://doi.org/10.1016/j.cell.2020.11.028

Differential gene expression following optogenetic stimulation

Cells were partitioned into the cell types annotated in Figure 7B. Using the Seurat function DiffExpTest, which employs a likelihood ratio test to identify differentially expressed genes, we analyzed cells for each cell type from ChR2+Light+ LN versus ChR2+Light- LN. Similarly, we identified differentially expressed genes by cell type between ChR2-Light+ LN versus Chr2-Light- LN. We reasoned that the DE genes in ChR2+ mice represented both the effects of neuronal stimulation, as well as changes induced by surgery and/or phototoxicity, while the DE genes in the ChR2- mice only correspond to changes due to surgery and/or phototoxicity. For each cell type, we identified genes DE in ChR2+ animals by a Holm-adjusted p value cutoff of 0.05, and eliminated genes from these lists that were also DE (using the same cutoff) in ChR2- LN. We calculated the effect size using Cohen's d, and restricted our gene lists to only those genes with a non-negligible effect size, using a cutoff of 0.2 (analysis of the effect of various effect-size cutoffs in Figure S7F). The results of these analyses for each cell type can be found in Table S3. In Figure 7H, we further restricted our DE gene lists for heatmap visualization, and in Figure 7J for gene ontology analysis (using DAVID, as described above) by only including genes that were also DE between LNs harvested from the same mouse in at least 2 of 4 ChR2+ mice.

Statistical testing

Using prism software, we performed unpaired two-tailed Student's t tests for Figures 1E, 1H, and 5F, Welch's t tests for Figures 5G, 5H, 5K, 5L, S1G, S3C, S4N, and S4O, 2-way ANOVA with Sidak's multiple comparisons test with for Figure S7E. All other statistical tests corresponding to differential gene expression or assessment of interaction potential are described above and completed using R language for Statistical Computing. Tests of correlation and correlation significance are annotated by the correlation model used (Pearson versus Spearman) were completed using R language for Statistical Computing. Parameters such as sample size, number of replicates, number of independent experiments, measures of center, dispersion, and precision (mean ± SEM) and statistical significances are reported in Figures and Figure Legends. A p value less than 0.05 was considered significant unless otherwise reported; a more stringent cutoff of 0.01 was used in some instances, and annotated as such. Where appropriate, a Holm correction was used to account for multiple tests, as noted in the figure legends or STAR Methods.

Supplemental Figures

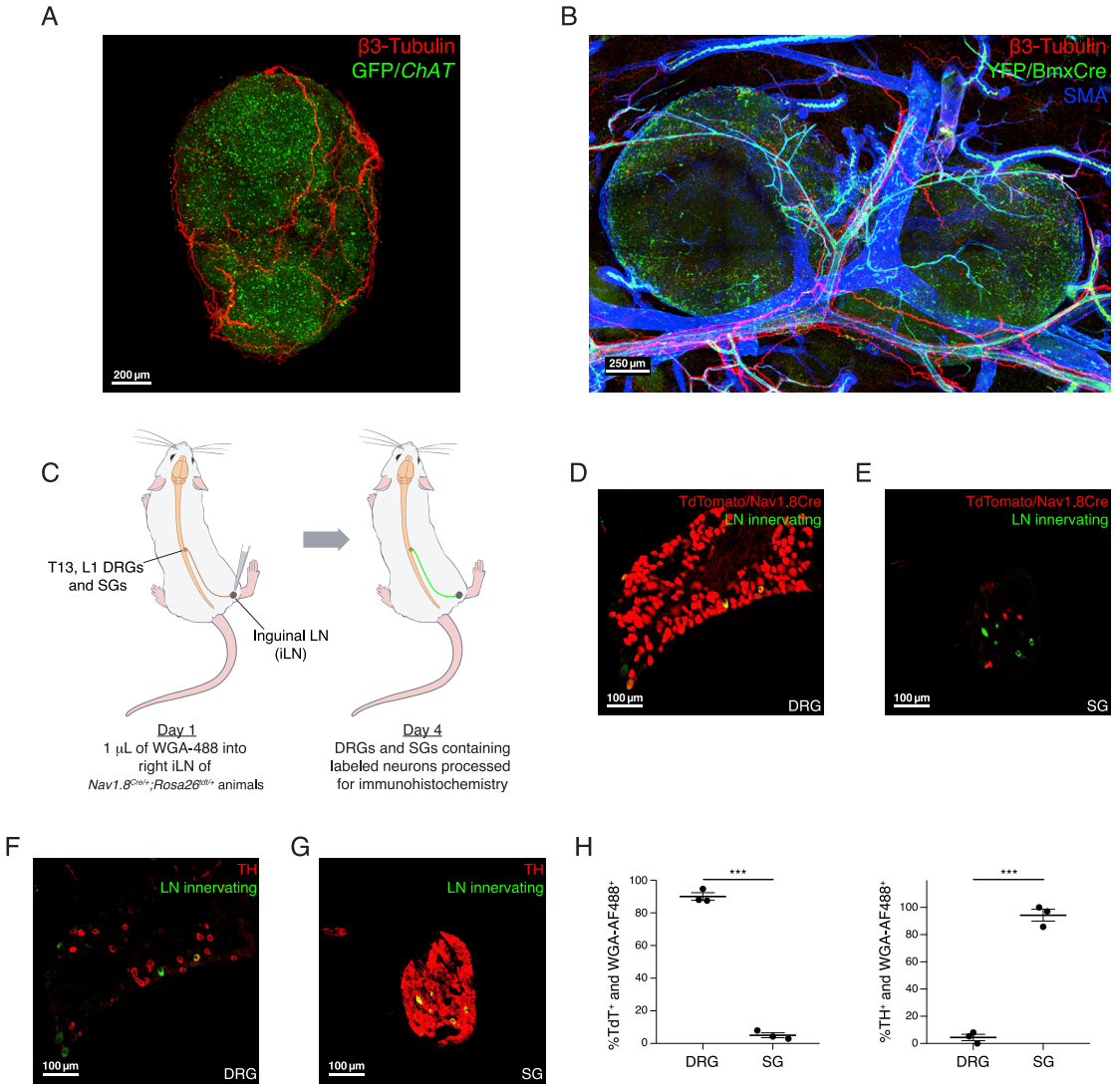

Figure S1. Confirmation of specific labeling of sensory and sympathetic innervation of LN with Nav1.8^{Cre} and TH, related to Figure 1

(A) 3D reconstruction of a representative confocal image of whole-mount popLNs from *ChAT^{BAC}-eGFP* animals, where cholinergic cells are genetically labeled with GFP, stained for β3-Tubulin (red), GFP (green). Scale bar, 200μm. (B) 3D reconstruction of a representative confocal image of whole-mount iLNs from tamoxifen-treated *Bmx-CreER^{T2} Rosa26$^{LSL\text{-}eYFP/+}$* animals, where arterial endothelial cells are genetically labeled with YFP, stained for β3-Tubulin (red), YFP (green), and smooth muscle actin (SMA, blue), demonstrating preferential association between nerves and arterial vessels supplying LNs. Scale bar, 250 μm. (C) The schematic for fluorescent wheat-germ agglutinin (WGA) -based retrograde tracing of iLN-innervating sensory neurons. (D and E) Representative confocal images of sections from DRGs and SGs containing WGA-AF488^{+} retrogradely-labeled iLN-innervating neurons of *Nav1.8$^{Cre/+}$; Rosa26$^{LSL\text{-}tdTomato/+}$* animals with endogenous fluorescence from tdTomato and WGA-AF488 shown in red and green, respectively. Scale bars, 100 μm. (F and G) Representative confocal images of sections from DRGs and SGs containing WGA-AF488^{+} retrogradely-labeled iLN-innervating neurons of *Nav1.8$^{Cre/+}$; Rosa26$^{LSL\text{-}tdTomato/+}$* animals, with TH stained in red and endogenous fluorescence from WGA-AF488 shown in green. Scale bars, 100 μm. (H) Quantification of the percentage of WGA-AF488^{+} retrogradely-labeled LN-innervating DRG or SG neurons that are genetically labeled with Nav1.8^{Cre} or are TH^{+}. Significance assessed by Welch's t test, p = 0.0003 (***), p < 0.001 (***), based on a total of 60 WGA-AF88^{+} DRG neurons and 167 WGA-AF88^{+} SG neurons from 3 mice. Error bars, SEM.

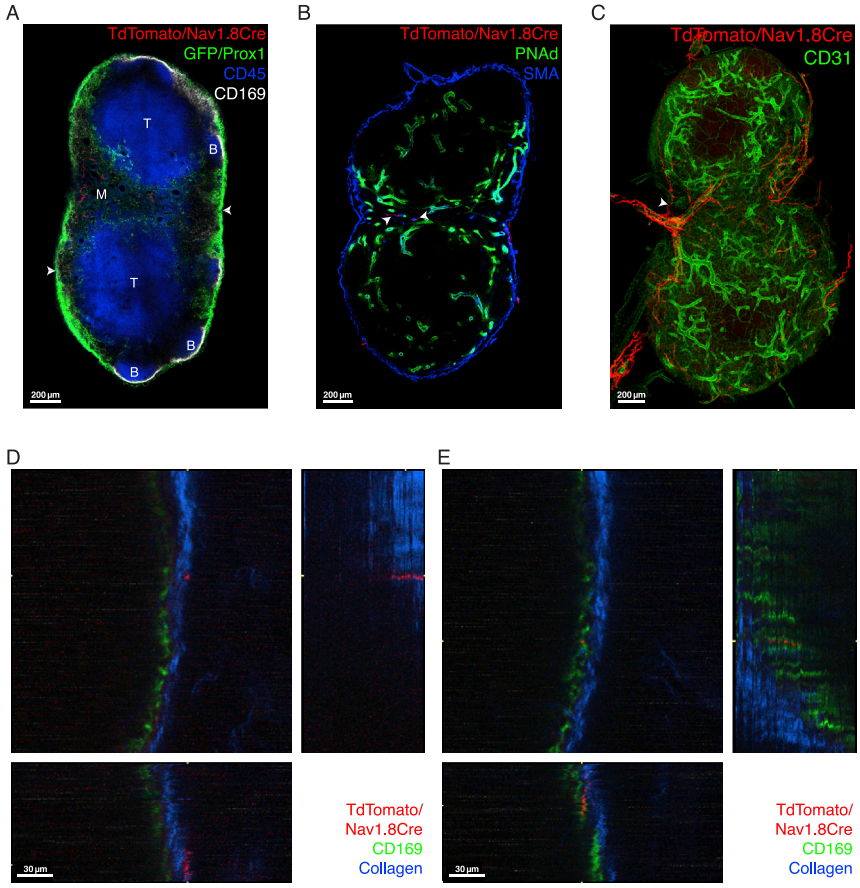

Figure S2. Anatomical characterization of sensory innervation of different LN subdomains, related to Figure 2

(A) A representative confocal section of whole-mount iLNs from *Nav1.8*$^{Cre/+}$; *Rosa26*$^{tdTomato/+}$; *Prox1-EGFP* animals, stained for tdTomato (red), GFP (green), CD45 (blue) and CD169 (white), allowing identification of LN subdomains, including T cell zone labeled as (T), B follicles labeled as (B) and the medulla labeled as (M). Note that the outermost layer of GFP$^+$ LECs (green) marked by arrowheads delineates LN boundary. Scale bar, 200 μm. (B) A representative confocal section of whole-mount iLNs from *Nav1.8*$^{Cre/+}$; *Rosa26*$^{LSL\text{-}tdTomato/LSL\text{-}tdTomato}$ animals, stained for tdTomato (red), PNAd (green) and SMA (blue), demonstrating a general lack of contact between tdTomato$^+$ sensory fibers (arrowhead) and PNAd$^+$ high endothelial venules (HEVs). Scale bar, 200 μm. (C) 3D view of a representative confocal substack of whole-mount iLNs from *Nav1.8*$^{Cre/+}$; *Rosa26*$^{LSL\text{-}tdTomato/LSL\text{-}tdTomato}$ animals, stained for tdTomato (red) and CD31 (green), illustrating the perivascular origin of capsular/subcapsular fibers (arrowhead). Scale bar, 200 μm. (D and E). Section view of an *intravital* two-photon micrograph of representative capsular/subcapsular tdTomato$^+$ sensory fibers (red) in relation to *in vivo* antibody labeled CD169$^+$ SCS macrophages (green) and collagen fibers (blue) detected by second-harmonic generation microscopy in popLNs from *Nav1.8*$^{Cre/+}$; *Rosa26*$^{LSL\text{-}tdTomato/+}$ animals, demonstrating the presence of capsular (D) and subcapsular (E) fibers. Scale bars, 30 μm.

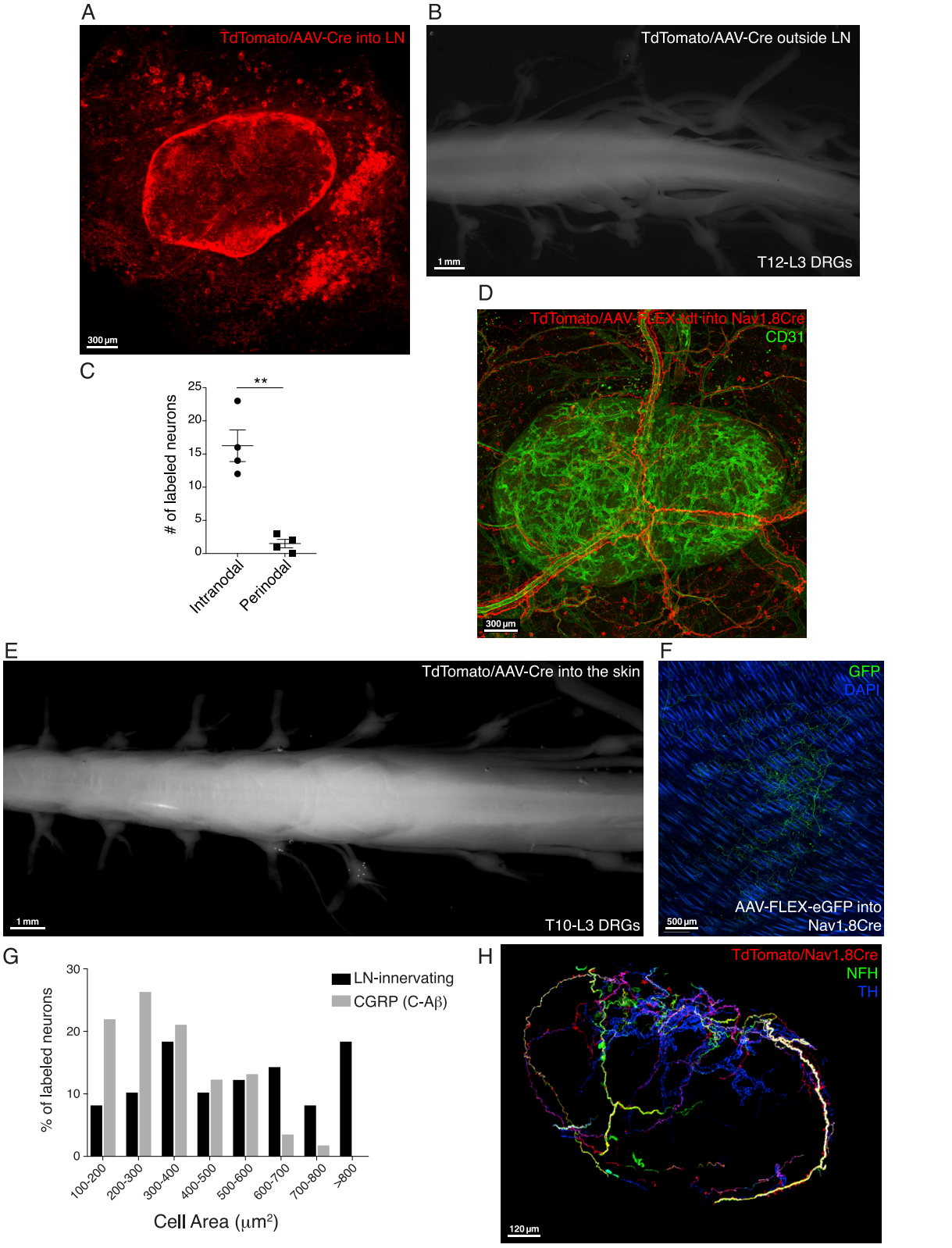

(legend on next page)

Figure S3. Evaluation of the specificity and efficiency of virus-based retrograde labeling, related to Figure 3

(A) 3D reconstruction of a representative confocal image of whole-mount iLNs targeted for intranodal injection with AAV-Cre from *Rosa26*$^{LSL\text{-}tdTomato/LSL\text{-}tdTomato}$ animals, stained for tdTomato (red) to show the extent of labeling at the site of injection. Scale bar, 300 μm. (B) Representative epifluorescence image of tdTomato^{+} DRG neurons retrogradely labeled from perinodal injection in a whole-mount spinal cord-DRG preparation without antibody amplification. Scale bar, 1 mm. (C) Quantification of the number of retrograde-labeled neurons from intranodal and perinodal injection. Intranodal: 16.25 (mean) ± 2.394 (SEM); perinodal: 1.500 (mean) ± 0.6455 (SEM), p = 0.0064 (**) by Welch's t test, n = 4 per group. (D) 3D reconstruction of a representative confocal image of whole-mount iLNs targeted for intranodal injection with AAV-Flex-tdTomato from *Nav1.8*$^{Cre/+}$; *Rosa26*$^{LSL\text{-}eYFP/+}$ animals, stained for tdTomato (red) and CD31 (green) to visualize the axonal projections of retrogradely-labeled neurons. Scale bar, 300 μm. (E) Representative epifluorescence image of tdTomato^{+} DRG neurons retrogradely labeled from the skin overlying the iLN in a whole-mount spinal cord-DRG preparation without antibody amplification. Scale bar, 1 mm. (F) 3D reconstruction of a representative confocal image of whole-mount skin targeted for intradermal injection with AAV-Flex-eGFP from *Nav1.8*$^{Cre/+}$ animals, stained for GFP (green) and DAPI (blue) to demonstrate the specificity of labeling from the skin. Scale bar, 500 μm. (G) Soma size distribution of retrogradely-labeled iLN-innervating and randomly sampled CGRP^{+} neurons from the same DRGs following intranodal injection of AAV-Cre into *Rosa26*$^{LSL\text{-}tdTomato/LSL\text{-}tdTomato}$ animals based on 49 tdTomato^{+} iLN-innervating and 114 CGRP^{+} DRG neurons from 3 and 2 mice, respectively. (H) 3D reconstruction of a representative confocal image of whole-mount iLNs from *Nav1.8*$^{Cre/+}$; *Rosa26*$^{LSL\text{-}tdTomato/LSL\text{-}tdTomato}$ animals, stained for tdTomato (red), neurofilament heavy chain (NFH, green) and TH (blue) to visualize co-innervation of LNs by myelinated and unmyelinated sensory fibers. Scale bar, 120 μm.

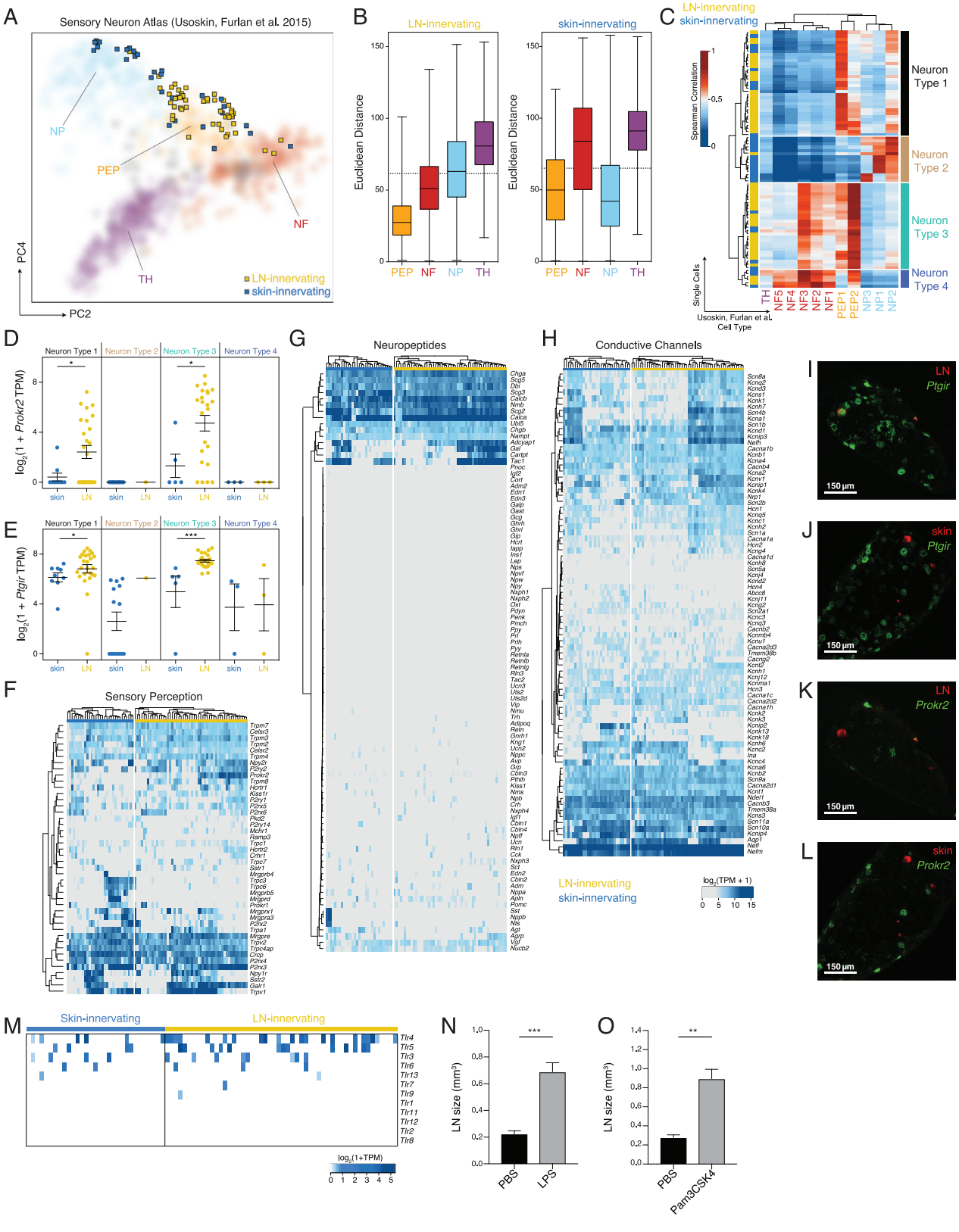

(legend on next page)

Figure S4. Contextualizing LN- and skin-innervating sensory neurons and evaluation of individual gene and gene pathway expression, related to Figures 4 and 5

(A) Principal Components (PCs) 2 versus 4 of Usoskin, Furlan Atlas (Usoskin et al., 2015), represented by transparent circles, colored by previously-defined cell types: non-peptidergic nociceptors (NP, light blue); peptidergic nociceptors (PEP, orange); neurofilament containing (NF, red); and tyrosine hydroxylase containing (TH, purple). LN-innervating (yellow squares) and skin-innervating (blue squares) neurons are projected onto the PC space (see STAR Methods). (B) Euclidean distance between each LN-innervating neuron (left) or skin-innervating neuron (right) and neurons in the Usoskin, Furlan Atlas, separated by cell type. Dashed lines represent the 99% confidence interval for distance between single cells categorized as the same cell type within the Atlas. Box represents 25-75 quantiles, error bars span min-max range. (C) Spearman correlation between the scRNA-seq profiles of LN- or skin-innervating neurons and neuronal subsets from the Usoskin, Furlan Atlas. Hierarchical clustering divides LN- and skin-innervating neurons into 4 major subtypes: Neuron Type 1 (PEP1-like, black); Neuron Type 2 (NP-like, tan); Neuron Type 3 (mixed PEP2/NF123, turquoise); and Neuron Type 4 (mixed PEP2/NF12345, dark blue). (D and E) Expression of *Prokr2* (D) and *Ptgir* (E) by innervation target and Neuron Type. Significance assessed by Mann-Whitney-Wilcoxon test *$p < 0.05$, ***$p < 0.001$. (F-H) Heatmaps of gene lists curated in the Usoskin, Furlan Atlas. Blue bar represents skin-innervating neurons, yellow bar represents LN-innervating neurons. (I-L) Representative confocal images of RNAscope analysis for indicated target (green) on DRG sections containing tdTomato$^+$ retrogradely-labeled neurons (red) ((I), (K): LN-innervating, (J), (L): skin-innervating). (M) Heatmap of toll-like-receptor (TLR) gene expression in LN-innervating (yellow bar) and skin-innervating (blue bar) neurons. Scale bars, 150 μm. (N) and (O) Volume of LNs following PBS versus LPS (N) or PBS versus Pam3CSK4 footpad injection (O) based on whole-mount LN immunohistochemistry. For (N), $p = 0.0005$ (***) based on 6 LNs per group from a total of 6 animals from different litters by Welch's t test; For (O), $p = 0.0055$ (**) based on 4 LNs per groups from a total of 4 animals from different litters by Welch's t test. Error bars, SEM.

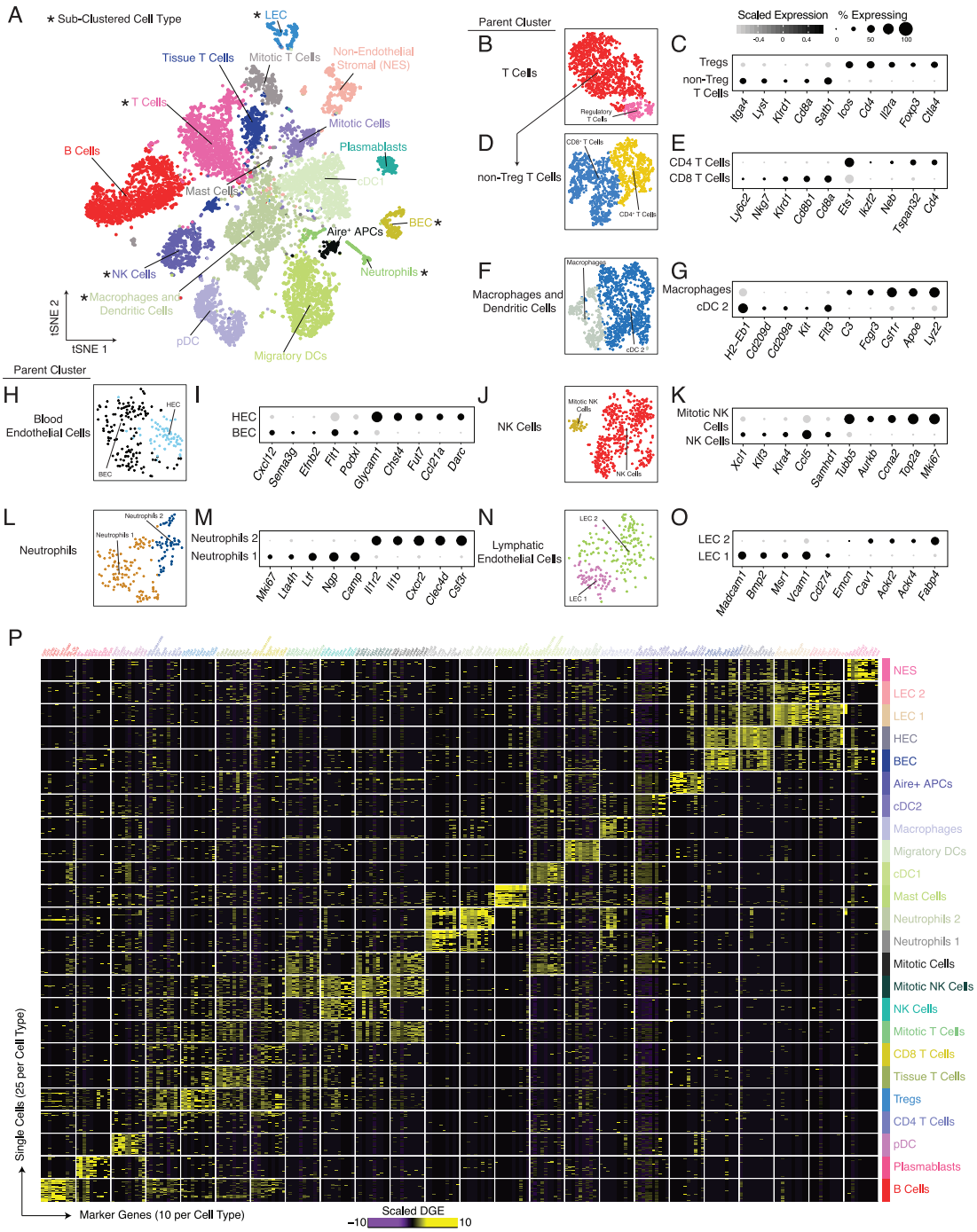

Figure S5. A single-cell RNA-seq atlas of iLNs at steady state, related to Figure 6

(A) tSNE of 9,662 single cells from an initial clustering analysis. * indicates clusters that required additional subclustering to resolve all constituent cell types. (B) tSNE of T cell parent cluster. (C) Dot plot of the top DE genes between Tregs and remaining non-Treg T cells. (D) tSNE of additional subclustering of non-Treg T cells from B. (E) Dot plot of the top DE genes between CD4 T cells and CD8 T cells. (F) tSNE of parent macrophage and dendritic cell cluster. (G) Dot plot of the top DE genes between Macrophages and cDC 2 cells. (H) tSNE of parent blood endothelial cell cluster. (I) Dot plot of the top DE genes between BEC and HEC. (J) tSNE of parent NK cells. (K) Dot plot of the top DE genes between mitotic NK cells and non-mitotic NK cells ("NK cells"). (L) tSNE of parent Neutrophil cluster. (M) Dot plot of the top DE genes between Neutrophils 1 and Neutrophils 2. (N) tSNE of parent Lymphatic Endothelial Cell (LEC) cluster. (O) Dot plot of the top DE genes

(legend continued on next page)

between LEC 1 and LEC 2. For all dot plots, circle diameters reflect the percent of cells expressing a given marker within that cell type, circle colors reflect relative expression abundance within that cell type; light gray: low, black: high. (P) Heatmap of gene-normalized, scaled DGE of the top 10 cell type-specific genes for each identified cell type (yellow: high relative expression; purple: low relative expression). Cell types reflect final clustering after subclustering, cell type-specific genes identified by comparing one cell type to all other cells in the dataset. Cell types are subsampled to 25 cells per cell type for heatmap.

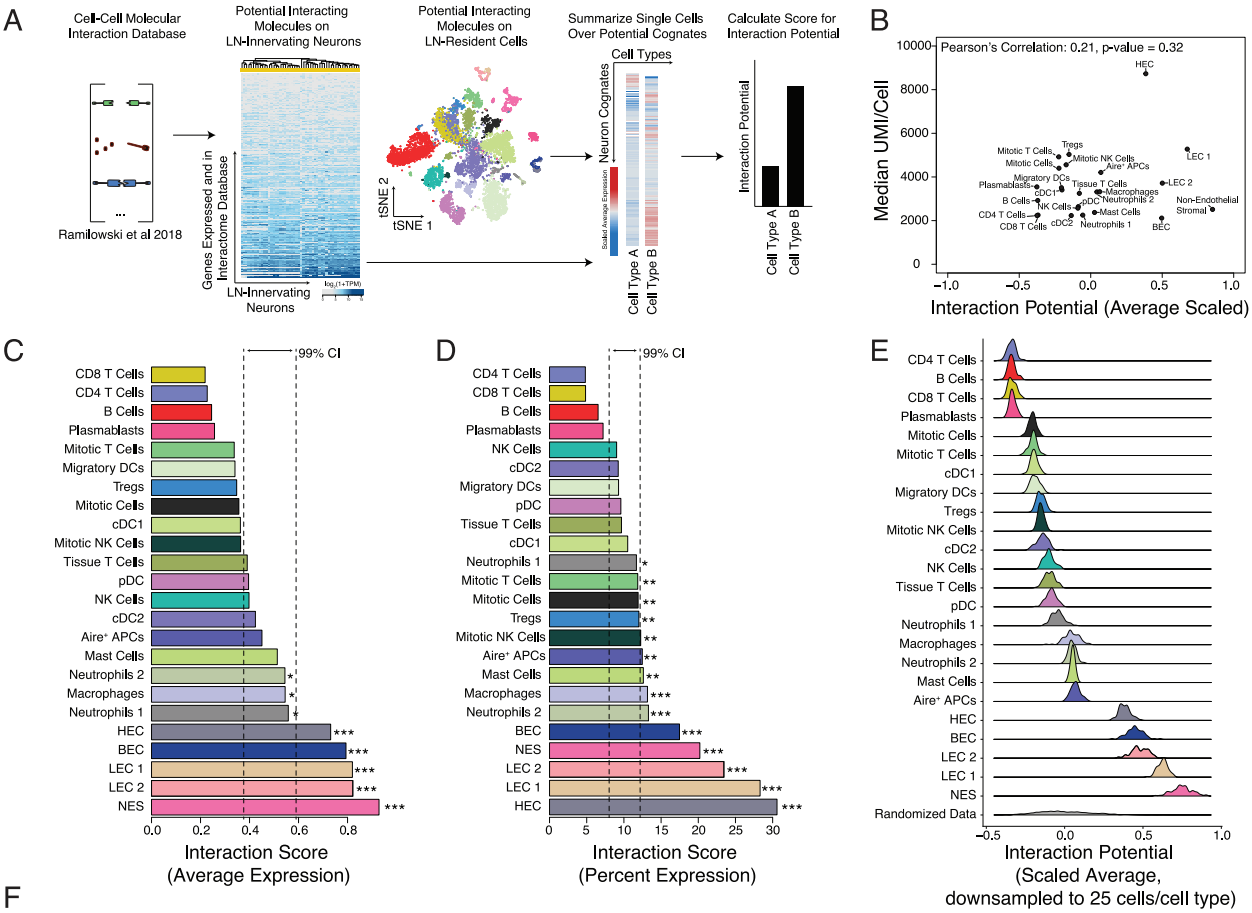

(legend on next page)

Figure S6. Evaluation of methods to determine neuron-LN cell interaction potentials, related to Figure 6

(A) Schematic of method for identifying cognate neuron-LN-cell pairs. (B) Pearson correlation of Interaction Potential (calculated as in Figure 6G) with cell quality (measured as median UMI/cell for each cell type). (C and D) Comparison of cell type summary statistics to calculate Interaction Potential ((C) average expression, (D) percent expression) *$p < 0.05$, **$p < 0.01$, ***$p < 0.001$, dashed lines represent 99% confidence interval from permutation test (see STAR Methods). (E) Comparison of Interaction Potential after downsampling to equivalent cell numbers (using the scaled average Interaction Potential, as in Figure 6G). (F) Left: Heatmap of top expressed neuropeptides in LN-innervating sensory neurons; Right: Dotplot of respective cognate receptor expression (denoted by arrows) in LN cells at steady state (circle diameter reflects the percent of cells expressing a given marker within that cell type, circle color reflects relative expression abundance within that cell type; light gray: low, black: high). (G and H) Top candidate interaction molecules driving high Interaction Potential in Figure 6E. (G) Non-Endothelial Stromal, (H) BEC.

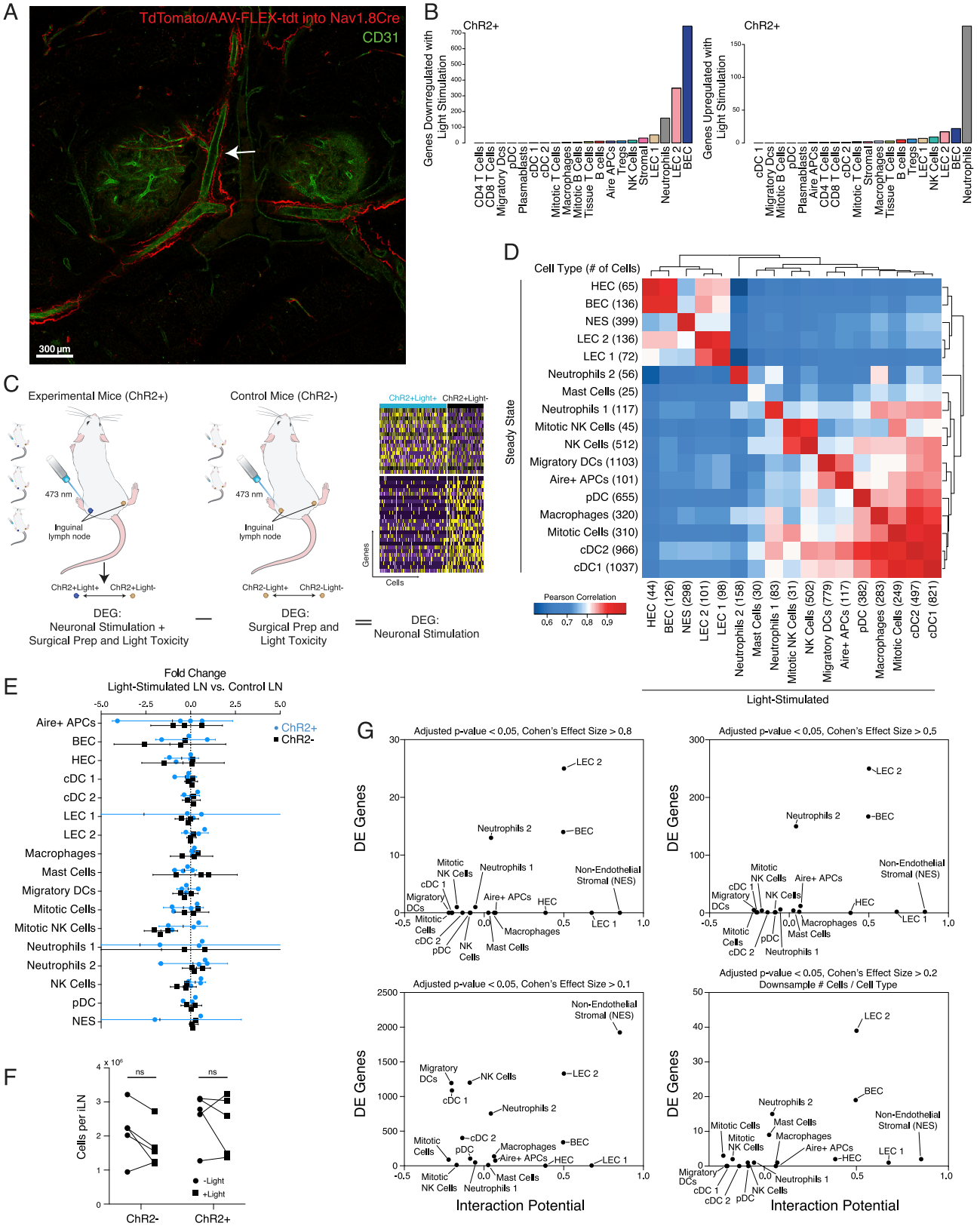

(legend on next page)

Figure S7. scRNA-seq of iLNs following optogenetic neuronal stimulation, related to Figure 7

(A) 3D reconstruction of representative confocal sections of whole-mount iLNs following intranodal injection of AAV-Flex-tdTomato into *Nav1.8*$^{Cre/+}$; *Rosa26*$^{LSL\text{-}eYFP/+}$ animals, stained for tdTomato (red) and CD31 (green) to reveal the axonal trajectory of iLN-innervating neurons in relation to the site of illumination (arrow). Scale bar, 300 μm. (B). Abundance of light-induced differentially expressed genes (left: downregulated with light stimulation; right: upregulated with light stimulation) among 2 ChR2+ animals, representing preliminary analysis of optogenetic-based neuronal triggering. (C) Schematic of mouse cohort and study design (differentially expressed genes, DEG). (D) Correlation between the pseudopopulation average gene expression profile of each cell type from the steady state iLN atlas (Figure 6, rows) and the light-stimulated iLN atlas (Figure 7, columns). (E) Quantification of alterations in cell composition by photostimulation, represented as fold change in fractional abundance of each cell type between matched light-exposed and light-unexposed sides within each mouse. Blue circles: ChR2+ mice, n = 4; black squares: ChR2- mice, n = 3. (F) Cellularity of light-exposed and light-unexposed iLNs from ChR2- and ChR2+ animals at the end of photostimulation. ChR2-: p = 0.2470 (not significant, ns); ChR2: p = 0.6755 (ns) by 2-way ANOVA with Sidak's multiple comparisons test; 5 mice per genotype. (G) Correlation between abundance of DE genes and interaction potential over multiple of DE gene cutoff parameters.